Design and engineering of structured light tailored for materials science applications

Dimitris Mansour

Department of Materials Science and technology

University of Crete

This thesis is submitted for the degree of
Doctor of Philosophy

Supervisor: Prof. Dimitris G. Papazoglou

Heraklion, 2021

Design and engineering of structured light tailored for materials science applications

University of Crete

Department of Materials Science and technology

PhD Thesis

Dimitris Mansour

Supervisor:	Prof. Dimitris G. Papazoglou
Comittee members:	Prof. Stelios Tzortzakis
	Prof. Maria Kafesaki

Heraklion, 2021

Table of Contents

Acknowledgements

First and foremost, I would like to express my deepest appreciation and sincere gratitude to my supervisor Prof. Dimitrios G. Papazoglou for his continuous support and guidance during all these years of my PhD thesis, and most importantly for his belief in me. He was always present, and willing to help and give me advice, in our fruitful meetings, as well as to encourage and inspire me. I could not have imagined having a better supervisor and mentor for my PhD study.

Besides my supervisor, I would like to thank Prof. Stelios Tzortzakis, head of UNIS group, and Prof. Maria Kafesaki for being members of the advisory committee of this PhD and evaluating this work. Moreover, it is also important to thank Prof. Konstantinos Makris, Dr. Emmanuel Stratakis, Prof. George Kopidakis and Prof. George Kioseoglou for agreeing to evaluate this work without a second thought and being members of the 7-member committee of this PhD thesis. As well as Dr. Giannis Zacharakis for providing access to technical equipment necessary for my work.

Furthermore, I also wish to thank all the members of the UNIS group, Dr. Anastasios Koulouklidis, Dr. Mary Manousidaki, Dr. Vladimir Fedorov, Michalis Loulakis, Christina Lanara, and Christina Daskalaki, for being great colleagues.

I sincerely wish to thank my collaborators and friends Dr. Evangelos Skoulas, Matina Vlachou, Dr. Ioannis Makos, Apostolis Brimis, Mikis Mylonakis, Dionysis Xydias, Giorgos Maragkakis.

I wish to acknowledge financial support from the Heracles project, and to thank Prof. Dimitrios Anglos and Dr. Paraskevi Pouli. The research work was supported by the Hellenic Foundation for Research and Innovation (HFRI) and the General Secretariat for Research and Technology (GSRT), under the HFRI PhD Fellowship grant (GA. no. 844).

Last but not least, I would like to thank my family and all the people who supported me through this journey.

Abstract

The generation of custom light fields, often described as structured light, is a topic of wide interest in optics. Structured light provides a significant advantage compared to non-structured light, by enabling us to control the intensity distribution and the focus position in both linear and non-linear propagation regimes. Such a control is challenging for high-power beams, since as one increases the beam's optical power, nonlinear effects inevitably take place and as a result the beam's spatial structure is dynamically altered. Although a plethora of structured optical beams have been introduced to address this problem, their generation is not trivial. Their complexity challenges our current state of the art techniques for light structuring and has urged us to exploit, among others, unconventional approaches like the use of optical aberrations or spatial multiplexing.

This thesis is focused on theoretical and experimental design techniques for materializing structured optical wave packets, with higher efficiency and power and at broad spectral range, tailored for materials science applications. These novel techniques include among others the use of reflecting optics as broadband continuous phase masks, which allowed us to experimentally study the effect of spatiotemporal coherence on the propagation of accelerating wave packets and to generate curved plasma channels for THz generation in air. Likewise, using rotationally symmetric accelerating beams as a template, we introduce a toolbox of versatile light scalpels, and demonstrate the generation of Tornado waves, an exciting new type of spiralling light that combines radial and angular acceleration with a precisely tuned focal distribution.

Περίληψη

Η δημιουργία ειδικά σχεδιασμένου φωτός, ή όπως συχνά αναφέρεται διαμορφωμένο φως, είναι ένα πεδίο ευρέως ενδιαφέροντος στην οπτική. Διαμορφωμένο φως προσδίδει ένα σημαντικό πλεονέκτημα σε σύγκριση με μη διαμορφωμένο φως, επιτρέποντας τον έλεγχο της κατανομής της έντασης και την θέση της εστίας στη γραμμική και μη-γραμμική περιοχή. Ένας τέτοιος έλεγχος είναι αρκετά απαιτητικός για δέσμες με μεγάλη ισχύ, εφόσον όσο η ισχύς της δέσμης αυξάνεται τόσο τέτοια μη γραμμικά φαινόμενα εμφανίζονται με αποτέλεσμα να αλλάζουν δυναμικά την χωρική κατατομή της δέσμης. Αν και πρόσφατα υπάρχει μια πληθώρα από διαμορφωμένες δέσμες φωτός για λύση αυτού του προβλήματος, ωστόσο η δημιουργία τους δεν είναι απλή. Η πολυπλοκότητά τους είναι πρόκληση για τις υπάρχουσες τεχνικές διαμόρφωσης φωτός και μας ωθεί σε μη συνήθεις προσεγγίσεις όπως την χρήση οπτικών σφαλμάτων ή της χωρικής πολυπλεξίας. Αυτή η διατριβή επικεντρώνεται σε θεωρητικές και πειραματικές τεχνικές σχεδιασμού για την δημιουργία διαμορφωμένων οπτικών κυματοπακέτων, με μεγαλύτερη απόδοση και ισχύ καθώς και σε ευρύ φάσμα, ειδικά σχεδιασμένων για την εφαρμογές στην επιστήμη των υλικών. Σε αυτές τις καινοτόμες τεχνικές, συγκαταλέγονται, μεταξύ άλλων, η χρήση ανακλαστικών οπτικών ως συνεχείς φασικές μάσκες που λειτουργούν σε ευρύ φάσμα, επιτρέποντάς μας την πειραματική μελέτη της επίδρασης της χωρικής και χρονικής συμφωνίας κατά την διάδοση επιταχυνόμενων κυματοπακέτων καθώς και την δημιουργία καμπυλωμένου πλάσματος για την δημιουργία THz στον αέρα. Επίσης, χρησιμοποιώντας περιστροφικά συμμετρικές επιταχυνόμενες δέσμες ως μια παλέτα, εισάγουμε μία νέα εργαλειοθήκη οπτικών δεσμών και επιτυγχάνουμε την δημιουργία των Tornado waves, μια καινούργια κατηγορία δεσμών με σπειροειδή τροχιά που συνδυάζει ακτινική και γωνιακή επιτάχυνση, διαμορφώνοντας με ακρίβεια την κατανομή στην εστία.

Thesis Summary

A plethora of optical beams with non-trivial amplitude and phase distributions have been recently introduced. In a collection containing only the, classical now, Bessel beams an increasing number of new members like the Airy and the radially symmetric Airy, Mathieu and Pearcey beams have been added, along with beams carrying orbital angular momentum (OAM). These structured optical wave packets propagate in curved trajectories and resist to diffraction or dispersion. Therefore, they are able to self-heal, bypass obstacles, and create abrupt foci. Such advantages make them ideal candidates to form a new set of tools applied in various applications ranging from materials processing and characterization to telecommunications. On the other hand, the generation of these wave packets is not trivial. Their complexity challenges our current state of the art techniques for wavefront shaping, and has urged us to exploit, among others, unconventional approaches like the use of optical aberrations, and spatial multiplexing. This thesis is focused on design techniques for materializing structured optical wave packets, with higher efficiency and power and at broad spectral range, tailored for materials science applications.

In the first Chapter we make an introduction of wave propagation and paraxial wave propagation as most of the waves that we deal with in this thesis are in the paraxial regime. We introduce structure light by presenting usually used in applications Gaussian and Bessel beams, and we make and introduction to accelerating Airy beams and other types of structure light beams. Following we show a few applications of structure light. We close this chapter by presenting basic principles of spatial and temporal coherence of light.

In the next Chapter we explore our approach for the design and engineering of structured light. We present our pallet of accelerating beams, namely the 1D Airy and 2D airy beams as well as the cylindrically symmetric Airy beams and study their behavior along propagation. Moreover, we introduce a unified description of the two variants of cylindrically symmetric Airy beams, called ring-Airy and inverse ring-Airy respectively, in which we have added a conical phase gradient to have more control over their focal characteristics. Furthermore, we derive semi-empirical analytical relations

for their focal characteristics. In addition, we show that by superimposing two cylindrically symmetric Airy beams with conical phase, we can create two foci feature that can be fully controlled, using our analytical predictions.

In the third chapter we present our generation techniques for the generation of structured light. We divide them in two main categories, in continuous and discrete methods. First we show that using aberration of simple reflective optics we can create a broadband continuous phase modulation device, and study its capabilities and operational regime. Then we present that it is possible to structure light using a phase-only imprinted in a spatial light modulation device. In addition we introduce, for the first time to our knowledge, a spatial multiplexing technique for the generation of multiple superimposed ring-Airy beams carrying orbital angular momentum, using a single phase mask.

In the final chapter we show our experimental results. To demonstrate the ability of our reflective phase modulation device to act as such we generated white light Airy beams and studied their properties. In addition, using this device we can create accelerating beams with variable partial spatial coherence and study their propagation dynamics in free space as well as their self healing properties when we block a part of the beam. Furthermore, we also demonstrate the capability of our device to withstand high powers by creating curved plasma channels and use them to generate THz waves. Finally, using the spatial multiplexing technique we presented in the previous chapter, we can generate spiraling and we show the first experimental observation of tornado waves.

1 Introduction

1.1 Wave propagation

The definition of a wave, although central to many physical phenomena that we observe, is not trivial. Beside cyclic definitions like: *"a wave is a solution of the wave equation"* or *"a wave is an oscillation of something"* a robust and generic definition [1] is that *"a wave is a propagating imbalance"*.

In this thesis we focus our attention on electromagnetic waves, and more specifically to light waves and ways to structure them. An electromagnetic wave refers to the simultaneous oscillation of the electric and magnetic fields, and for an isotropic medium is described by Maxwell's equations [2, 3].

$$\begin{aligned} \nabla \cdot \mathbf{D} &= \rho_f \\ \nabla \cdot \mathbf{B} &= 0 \\ \nabla \times \mathbf{E} &= -\frac{\partial \mathbf{B}}{\partial t} \\ \nabla \times \mathbf{H} &= \mathbf{J}_f + \frac{\partial \mathbf{D}}{\partial t} \end{aligned} \tag{1.1}$$

where $\mathbf{E}$ is the electric field, $\mathbf{B}$ is the magnetic field, while $\mathbf{D}$ is the electric displacement and $\mathbf{H}$ is an auxiliary vector field called H-field [1], and ρ_f and $\mathbf{J}_f$ are the external electric charge density and the corresponding electric current density respectively. The properties of a medium are usually described by two parameters: ϵ and μ, which are respectively the electric permittivity and magnetic permeability of that medium. From Eq. (1.1) we can derive wave equations for the electric and magnetic fields, in a medium free of charges and currents, ($\rho = 0$ and $\mathbf{J} = 0$):

$$\begin{aligned} \nabla^2 \mathbf{E} - \frac{1}{v^2}\frac{\partial^2 \mathbf{E}}{\partial t^2} &= 0 \\ \nabla^2 \mathbf{B} - \frac{1}{v^2}\frac{\partial^2 \mathbf{B}}{\partial t^2} &= 0 \end{aligned} \tag{1.2}$$

where $v = \frac{1}{\sqrt{\epsilon\mu}}$ is the speed of light in the medium. Assuming that we have a linearly polarized plane wave that is harmonic in space and time, propagating

[1] For further clarification about dispute for the name of $\mathbf{H}$ see [3] p. 271.

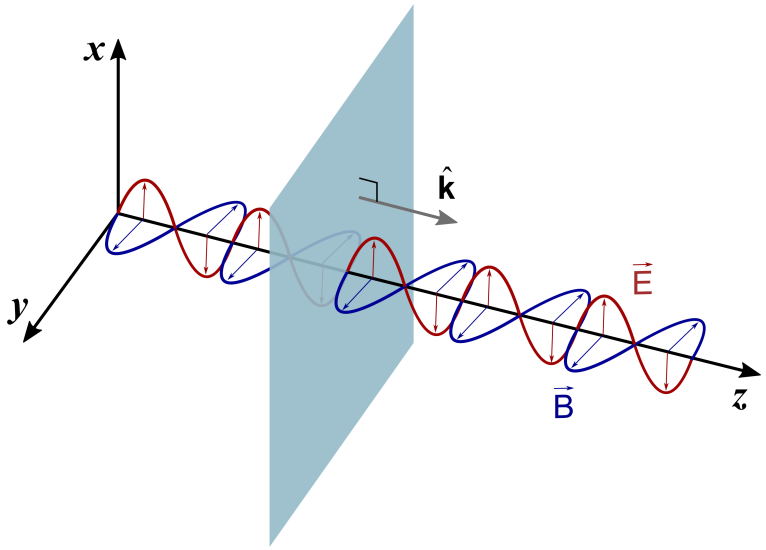

Figure 1.1: Illustration of a plane wave propagating along the z direction. The sinusoidal curves depict the oscillating electric $\mathbf{E}$ and magnetic $\mathbf{B}$ fields.

in an arbitrary direction, then its electric field can be described by:

$$\mathbf{E}(\mathbf{r}, t) = E_0 \exp[i(\mathbf{k} \cdot \mathbf{r} - \omega t)]\hat{\mathbf{n}}$$

where $\hat{\mathbf{n}}$ is the polarization direction, which refers to the oscillation direction of the electric field, i is the imaginary unit, $\mathbf{r}$ is the position vector, $\mathbf{k} = \frac{2\pi}{\lambda}\hat{\mathbf{k}}$ is the wave-vector, while the unitary vector $\hat{\mathbf{k}}$ is parallel to the propagation direction, λ is the wavelength, and ω is the angular frequency. An example of a plane wave propagating in z direction is illustrated in Fig. 1.1. The wave is linearly polarized parallel to the x axis, while the magnetic field is parallel to the y axis. Note that the electric and magnetic field vectors oscillate in phase, normal to each other as well as to the propagation direction.

1.1.1 Paraxial approximation

Solving the wave equations (1.2) to study E/M wave propagation is not trivial since the field vectors variate both in space and time. On the other hand, under some common and simple constrains, the equations can be simplified while still describing a plethora of optical phenomena. To begin with, assuming that the waves are harmonic the electric field can be described as:

$$\mathbf{E}(\mathbf{r}, t) = \tilde{\mathbf{E}}(\mathbf{r}) \exp(-i\omega t) \tag{1.3}$$

where $\tilde{\mathbf{E}}(\mathbf{r})$ describes the spatial distribution of the field and ω is the angular frequency. Substituting this into the wave equation Eq. (1.2) leads to the

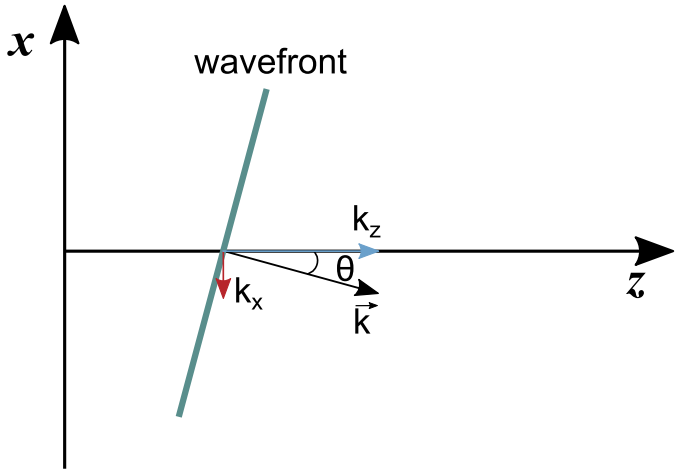

Figure 1.2: Illustration of a paraxial wavefront and its wavenumber projection on transverse and longitudinal axes, where the optical axis is the z direction.

Helmholtz equation:

$$\nabla^2\tilde{\mathbf{E}}(\mathbf{r},t) + k^2\tilde{\mathbf{E}}(\mathbf{r},t) = 0 \tag{1.4}$$

where $k = \omega/v$ is the wavenumber, and v the velocity of the light wave in the medium. Let us now focus on the study of the propagation of such harmonic waves, which propagate along an axis, referred to as propagation axis. These waves are often described as paraxial because, as they propagate, they weakly spread in a direction transverse to the propagation axis. From a geometrical point of view paraxial propagation refers to rays that make a small angle (typically $\theta \leq 20^o$) to the propagation axis. This is depicted in Fig. 1.2 where it shows a paraxial wavefront with its corresponding wave-vector and its projection on transverse and longitudinal axes, in this case the angle between wave-vector $\mathbf{k}$ and the propagation is sufficiently small ($\theta \leq 20^o$), thus the projection of $\mathbf{k}$ on z axis is much larger than that on x axis $k_z \gg k_x$.

The propagation of such a field includes a dense oscillation, with a period λ, and a slower evolution of the field amplitude. Assuming that the wave propagates along z axis, we can decouple these two by using a carrier wave with a slow changing amplitude $\mathbf{u}(\mathbf{r})$ to describe the field distribution:

$$\tilde{\mathbf{E}}(\mathbf{r}) = \mathbf{u}(\mathbf{r})\exp(ikz) \tag{1.5}$$

Using the carrier wave/envelope description of Eq. 1.5 Helmholtz equation (Eq. 1.4) can now be further simplified:

$$(\nabla_\perp^2 + \frac{\partial^2}{\partial z^2} + 2ik\frac{\partial}{\partial z})\mathbf{u}(\mathbf{r}) = 0 \tag{1.6}$$

where the symbol $\nabla_\perp^2$ denotes the transverse part of the Laplacian operator, which in Cartesian coordinates is $\nabla_\perp^2 = \frac{\partial^2}{\partial x^2} + \frac{\partial^2}{\partial y^2}$. Since we are focused on the study of paraxial waves, the field amplitude $\mathbf{u}(\mathbf{r})$ evolves much slower in the longitudinal direction compared to the transverse direction so we can apply the so called *slowly varying envelope approximation* [2]:

$$\frac{\partial^2 \mathbf{u}(\mathbf{r})}{\partial z^2} \ll k\frac{\partial \mathbf{u}(\mathbf{r})}{\partial z}, \ \frac{\partial^2 \mathbf{u}(\mathbf{r})}{\partial z^2} \ll k\nabla_\perp^2 \mathbf{u}(\mathbf{r}) \tag{1.7}$$

Taking all of the above into account, the Helmholtz equation Eq. (1.4) reduces to the paraxial wave equation:

$$i\frac{\partial \mathbf{u}(\mathbf{r})}{\partial z} = -\frac{1}{2k}\nabla_\perp^2 \mathbf{u}(\mathbf{r}) \tag{1.8}$$

Furthermore, in the case of a paraxial wave the field projection along the propagation axis is infinitesimal ($\mathbf{k} \simeq k_z\hat{\mathbf{k}} \Rightarrow \mathbf{u}\cdot\hat{\mathbf{z}} \simeq 0$). Thus the propagation of such waves can be decoupled from their polarization $\mathbf{u}(\mathbf{r}) = u(\mathbf{r})\hat{\mathbf{p}}$, where u is the wave amplitude and $\hat{\mathbf{p}}$ is the polarization state. In this case, Eq. 1.8 can be written [4] in a scalar form as:

$$i\frac{\partial u(\mathbf{r})}{\partial z} = -\frac{1}{2k}\nabla_\perp^2 u(\mathbf{r}) \tag{1.9}$$

In the following we will mainly use of this equation since we are focused in problems related to the paraxial propagation regime. In addition, quite often we will study cylindrical symmetric beam distributions. The scalar paraxial wave equation in cylindrical coordinates (r, ϕ, z) for a light beam with cylindrical symmetry where its field distribution $u(r, z)$ is independent of the azimuthal angle ϕ is:

$$\frac{\partial^2 u(r,z)}{\partial r^2} + \frac{1}{r}\frac{\partial u(r,z)}{\partial r} + 2ik\frac{\partial u(r,z)}{\partial z} = 0 \tag{1.10}$$

Furthermore, it is not hard to recognize that the Eq. (1.8) is mathematically identical to Schrödinger's equation of free particles [5] in quantum mechanics.

$$i\hbar\frac{\partial \psi(\mathbf{r},t)}{\partial t} = -\frac{\hbar^2}{2m}\frac{\partial^2 \psi(\mathbf{r},t)}{\partial \mathbf{r}^2} \tag{1.11}$$

where $\hbar$ is the reduced plank's constant, $\psi(\mathbf{r}, t)$ is the spatiotemporal probability wave-function of the free particle, of mass m. The mathematical equivalence $z \leftrightarrow t$ dictates that a propagation along z of an optical wave is equivalent to the evolution along time t of a wave-function. This allows us to study the evolution of a quantum mechanical wave-packet, through the propagation of an optical wave, using an equivalent optical scheme and vice versa. As we will further discuss in the following sections this mathematical equivalence bridges the fields of Optics and Quantum Mechanics allowing for a fruitful interchange of ideas and applications.

1.2 Structured light

By structured light we describe the generation of optical fields that are customized. Structuring can involve, independently or in combination [6], the spatial modulation of amplitude, phase, and polarization of a light wave. In most of the cases, the goal is to achieve a tailored propagation or a focal intensity distribution. In the following we will review some of the light distributions that are available, and compare them with respect to their propagation properties.

1.2.1 Gaussian beams

The most commonly used intensity profile of a light wave is the Gaussian distribution [7, 8]. Gaussian beams, are easy to handle, require no special equipment to generate them, and their propagation can be analytically described through optical systems [2, 9]. Likewise, they are easily focused to localized and intense foci, using a simple converging lens. On the other hand, their focal aspect ratio (ratio of focal width to focal length) depends on the focus position with respect to the initial plane (z=0). The amplitude distribution of this beam, at some plane (z) along its propagation, is mathematically described by:

$$\mathbf{E}(r,z) = E_0 \frac{w_0}{w(z)} \exp(-\frac{r^2}{w(z)^2}) \exp\{-i[kz + k\frac{r^2}{2R(z)} - \psi(z)]\}\ \hat{\mathbf{n}} \quad (1.12)$$

where r is the radial distance, z is the propagation distance, E_0 is the peak electric field amplitude at $z = 0$, $\hat{\mathbf{n}}$ is a vector describing the polarization state, $w(z)$ is the beam semi-diameter defined by the radius at which the field amplitude falls to $1/e$ of its peak value, $w_0 = w(0)$ is the beam waist, $R(z)$ is the beam's wavefront radius of curvature, and $\psi(z)$ is the Gouy phase, representing the phase difference of Gaussian beam compared to a plane wave [7]. Using the normalization of the paraxial wave equation we can see that a Gaussian beam of waist w_0 will spread as it propagates at a distance comparable to $z_R = \pi w_0^2/\lambda$, which we refer to as Rayleigh length [7]. Another, commonly used, metric for the description of the transverse size of a beam is the full width at half maximum (FWHM). For Gaussian beams this is related to the beam semi-diameter FWHM $= 2\sqrt{\ln 2}$ w(z). Fig. 1.3(a) shows the propagation [2] of a Gaussian beam with $FWHM =$ 500 μm, and a wavelength of $\lambda =$ 800 μm with a Rayleigh length of $z_R \cong$ 510mm. As we can observe, the intensity decreases and the beam becomes wider as it propagates at a distance comparable to z_R. Typically, the intensity of a Gaussian beam is highest at the beam's waist. On the other hand, such a beam can be focused using a lens, achieving a high intensity at the focus,

[2] The numerical simulations in this thesis were preformed using *PyWp*, an angular spectrum propagation algorithm [10] developed in Python^{TM}.

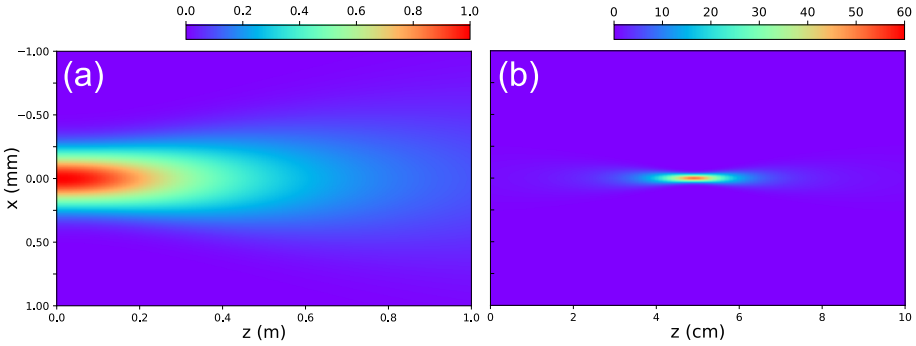

Figure 1.3: Intensity distribution $I(x, z)$ of (a) a Gaussian beam with FWHM = 500 μm and (b) the same Gaussian beam focused by a lens of a focal distance $f = 50$ mm.

which comprises the new waist, in a remote distance. In Fig. 1.3(b) we show numerical simulation results of the propagation of a Gaussian beam after being focused by a thin lens of focal distance $f = 50$ mm, placed at $z = 0$. Clearly the maximum intensity at the focus is multiple times that of the initial $I_{max} \sim 60\ I_0$.

1.2.2 Non-diffracting waves

Diffraction is a fundamental physical property of travelling light [2], and it is manifested by the spreading of a wave as it propagates in free space, or when it encounters an obstacle. According to the Fresnel-Huygens principle [2], diffraction results from the distributed interference of secondary waves emitted from various points on the original wavefront. On the other hand, diffraction can also be explained by means of the uncertainty principle [5], originating from the transverse spatial confinement of the beam, that results either from it's finite size or by the presence of an obstacle.

Interestingly, there exists a special type of waves that overcome diffraction. These waves, referred to as *non-diffracting* waves [11], are solutions of the paraxial wave equation (Eq. 1.8) with their intensity distribution remaining invariant along the propagation. A trivial non-diffracting wave is the plane wave. It is easy to understand, using Babinet's principle [2], that when a non-diffracting wave is blocked by an obstacle, the diffracted wave will decay after some propagation distance allowing for the non-diffracting wave to self-heal. The realization of such waves is practically impossible, since they are infinite in size and carry infinite energy. Nevertheless, variants of them with finite size and energy can be realized by proper apodization. These waves are quasi-non-diffracting since they impart many of the properties of their ideal counterparts. Their transverse distribution remains unchanged over a finite propagation distance and they exhibit self healing when ob-

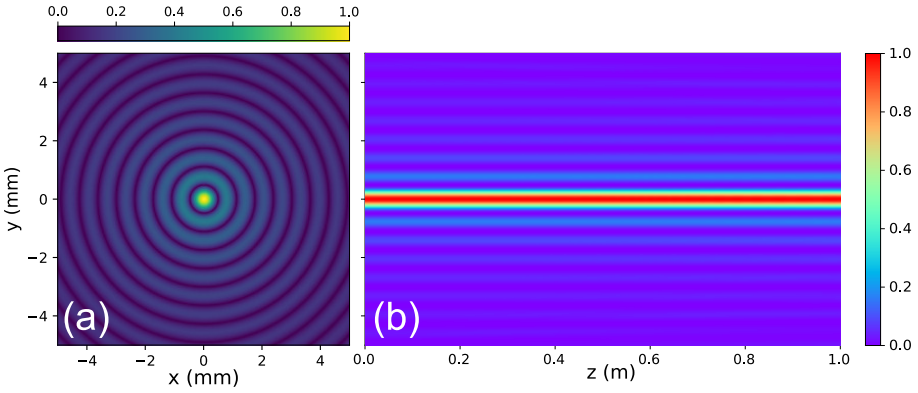

Figure 1.4: Distribution of an ideal, non-diffracting Bessel beam $J_0(cr)$ with $c = 0.2 \cdot 10^{-3} m^{-1}$ (a) Amplitude distribution at the transverse $x-y$ initial plane ($|A(x, y, z = 0)|$) and (b) Intensity distribution $I(y, z)$ at a $y-z$ plane along propagation. Numerical simulation results [10]

scured by an obstacle. In the following, we will examine in more detail two, commonly used, types of non-diffracting beams namely the Bessel and the Airy beam.

Bessel beams

Bessel beams were the first non-trivial non-diffracting waves that were proposed [12, 13]. In these first publications, a non-diffracting solution to the wave equation was presented, in the form of a zero-order Bessel function of the first kind [14], J_0[‡]. Bessel beams are actually comprised by a conical wavefront. Their angular spectrum is a ring of radius $k \sin\theta$, where k is the wavenumber and θ is the conical angle.

Fig. 1.4(a) shows the amplitude distribution at the transverse initial $x-y$ plane of a pure Bessel beam $J_0(cr)$ where c is a constant, and r is the radius. Note the characteristic high intensity hot-spot in the center that is surrounded by rings of decaying amplitude. Fig. 1.4(b) depicts numerical simulation results of the intensity $I(y, z)$ distribution at the $y-z$ plane. The non-diffracting property of the ideal Bessel beam that remains invariant along z is clearly visible. Bessel beams of finite energy, referred to as Bessel-Gauss, can be generated by transforming a collimated Gaussian beam using a circular slit in combination with a is focusing lens [13], or by using a conical lens or axicon [15, 9, 16], or by directly imprinting a conical phase using a spatial light modulator (SLM) [17, 18]. The field distribution of Bessel-Gauss

[‡]Bessel function of the first kind and n^{th} order: $J_n(x) = \frac{1}{\pi}\int_0^{\pi} \cos(n\theta - x\sin\theta)d\theta$

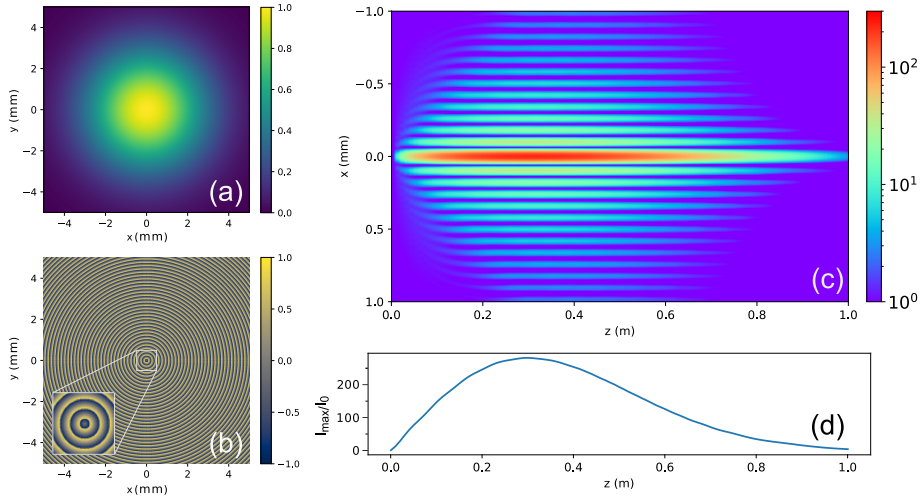

Figure 1.5: (a) Transverse amplitude profile of the Gaussian beam with $FWHM = 5$ mm (b) Conical phase gradient with angle $\theta = 5$ mrad (wrapped phase, in π units), (c) (x-z) intensity cross-section, and (d) Maximum peak intensity, normalized with initial intensity. Numerical simulation results I_{max}/I_0 along propagation. [10]

beams at the initial plane is described by:

$$u(r,0) = \exp(-\frac{r^2}{w_0^2}) \exp(ikr \sin\theta) \tag{1.13}$$

where r is the radius in cylindrical coordinates, w_0 is the waist of the initial Gaussian beam, and k is the wave number. Typical transverse amplitude and phase profiles of a Gauss-Bessel beam at the initial plane ($z = 0$) are shown in Figs. 1.5(a),(b). We clearly observe the characteristic Gaussian amplitude profile (FWHM = 5 mm) in Fig. 1.5(a), and the conical phase distribution (conical angle angle $\theta = 5$ mrad) in Fig. 1.5(b). Although Bessel-Gauss beams are not ideal, they impart some non-diffracting properties from their ideal Bessel counterparts. For example, they propagate for a considerable distance keeping an invariant intensity distribution compared to a similarly sized Gaussian beam, before they eventually spread out due to diffraction [12]. Numerical propagation results of the Gauss-Bessel beam depicted in Fig. 1.5(a),(b) are shown in Figs. 1.5(c),(d). It is clear that, at least partially, the non-diffracting properties of the pure Bessel beam are also present in the propagation of the Gauss-Bessel beam.

Airy beams

In 1979 Berry and Balazs in their well-known article [19] entitled *"Non-spreading wave packets"* showed that *"...for a wave ψ in the form of an*

Airy function the probability density $|\psi|^2$ *propagates in free space without distortion and constant acceleration.*". In this work they proved that the Airy function [§] [20], is the only, apart form the trivial plane wave, non-dispersing solution of the one dimensional Schröndiger's equation of a free particle. Moreover, notably this wave-packet, described by Airy function, not only does not spread with time but it also accelerates, to the positive x values, without an external force. The Airy function can be mathematically described using an integral:

$$Ai(x) = \frac{1}{\pi}\int_0^\infty \cos(xt + t^3/3)dt \tag{1.14}$$

As shown in Fig. 1.6 the Airy function is not symmetrical, being practically zero for $x > 0$ while oscillating with a decaying amplitude for $x < 0$. An approximation of the Airy function[22], describes well this behaviour:

$$Ai(x) \cong \mathrm{Re}\{\frac{\sin[\frac{2}{3}(-x)^{3/2}+\frac{\pi}{4}]}{\sqrt{\pi}\,(-x)^{1/4}}\} = \begin{cases} \frac{\sin[\frac{2}{3}(-x)^{3/2}+\frac{\pi}{4}]}{\sqrt{\pi}\,(-x)^{1/4}} & x \leq 0 \\ \\ \frac{e^{-\frac{2}{3}x^{3/2}}}{2\sqrt{\pi}\,x^{1/4}} & x > 0 \end{cases} \tag{1.15}$$

[§]The Airy function Ai(x) is a solution of the differential equation $y'' - xy = 0$ introduced by George B. Airy to describe the shape of a supernumerary rainbow [20, 21].

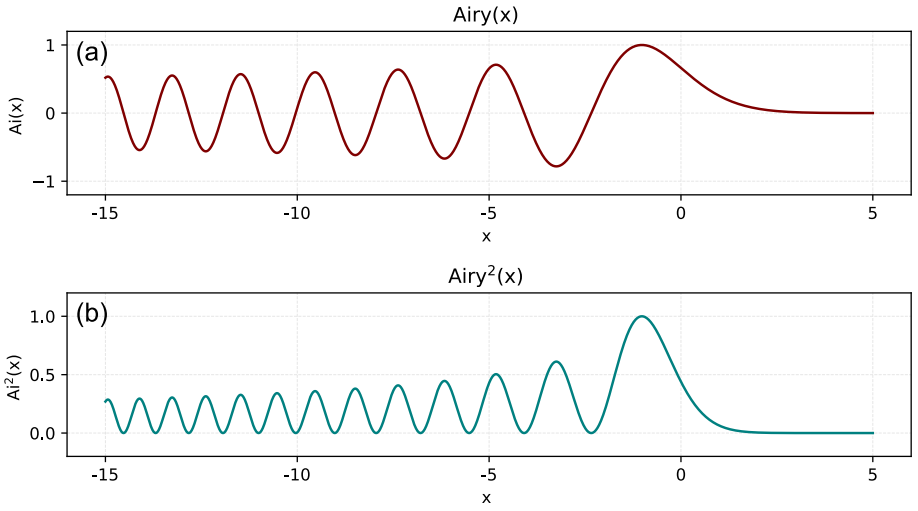

Figure 1.6: Plot of (a) an Airy function $Ai(x)$ and its square $Ai^2(x)$.

Using this approximation, it was recently demonstrated [23] that all powers of the Airy function can be described in an elegant way:

$$Ai(x)^{2m} \cong \sum_{n=0}^{m} \frac{2^{m-n} \cdot m!}{n!(m-n)!} E(x)^{2m-n} Ai(\hat{S} \cdot x)^n \tag{1.16}$$

$$Ai(x)^{2m+1} \cong \sum_{n=0}^{m} \frac{2^{m-n} \cdot m!}{n!(m-n)!} E(x)^{2m-n} Ai(\hat{S} \cdot x)^n \cdot Ai(x)$$

where $E(\rho) \equiv 1/[2\sqrt{\pi} f(\rho)^{1/4}]$, $\hat{S}$ is a linear scaling operator $\hat{S} \cdot \rho \equiv 2^{2/3}\rho + \pi/(8 \times 2^{1/3})$ and f is an apodization function described by:

$$f(x) \equiv \begin{cases} -x & x \leq -\frac{6}{5} \\ \frac{6}{5} - e^{-\frac{24}{5}} + e^{4x} & x > -\frac{6}{5} \end{cases}$$

Although the concept of a non-spreading wavefunction was demonstrated in the field of Quantum Mechanics, the mathematical equivalence of Schröndiger's equation and paraxial wave equation made these findings directly applicable to the field of Optics where non-diffracting Airy beams were introduced by Siviloglou et. al [24]. Besides the ideal Airy distribution, an exponential truncation was used in order to realize finite energy Airy beams:

$$u(x) = Ai(x)\exp(ax) \tag{1.17}$$

where $a > 0$ is an apodization factor. A typical truncated Airy function distribution is shown in Fig. 1.7. Although there are many other ways to

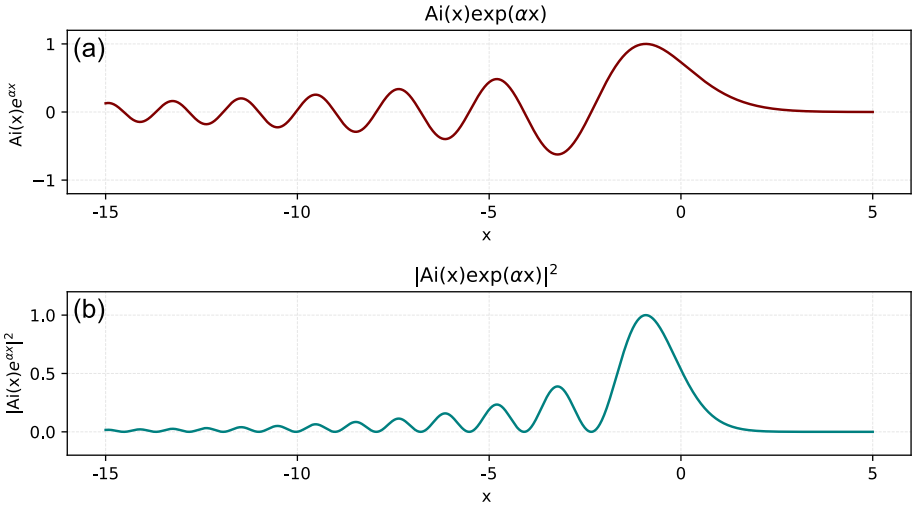

Figure 1.7: Plot of (a) truncated Airy function $\mathrm{Ai}(x)\exp(ax)$ and its square $|\mathrm{Ai}(x)\exp(ax)|^2$ with decay factor $a = 0.1$.

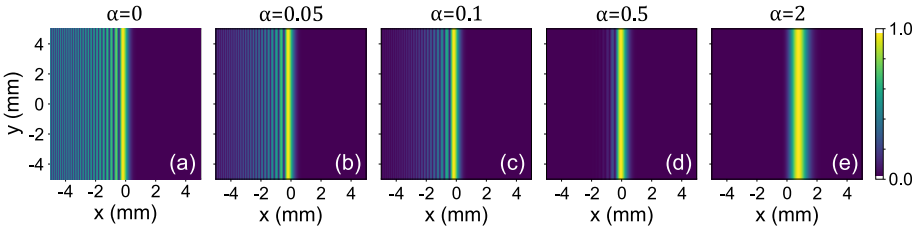

Figure 1.8: Transverse amplitude profiles at the initial plane ($|A(x, y, z = 0)|$) of 1D Airy beams with different apodization factors a. (a) $a = 0$, (b) $a = 0.05$, (c) $a = 0.1$, (d) $a = 0.5$, and (e) $a = 2$.

truncate the Airy distribution, this approach is quite beneficial for the realization of Airy beams since it's Fourier transform is a Gaussian distribution with an imprinted cubic phase [24, 25]. We will discuss in more detail about the generation techniques in the next chapters. Moreover, Figs. 1.8(a)-(e) depict the effect of the truncation factor a to the transverse amplitude profiles of the Airy beam. As the value of a increases the characteristic oscillatory distribution of the Airy beam disappears, while for values of $a > 1$ the Airy beam is practically transformed to a Gaussian-like beam.

The study of the propagation of the truncated version of the Airy beam or simply Airy beam is usually described in normalized coordinates. The paraxial wave equation in such coordinates is:

$$i\frac{\partial u(s,\xi)}{\partial \xi} + \frac{1}{2}\frac{\partial^2 u(s,\xi)}{\partial s^2} = 0 \tag{1.18}$$

where u is the electric field envelope, $s = x/w$ is a transverse dimensionless coordinate, with w being an arbitrary transverse scale parameter, $\xi = z/kx_0^2$ is a longitudinal dimensionless coordinate, and $k = 2\pi n/\lambda$ is the wavenumber and n the refractive index of the medium.

The analytic solution for the propagation of the Airy beam $u(s, 0) = Ai(s)\exp(as)$, is derived [24] by directly integrating Eq. (1.18) and is given by:

$$\begin{aligned} u(s,\xi) = Ai[s - (\frac{\xi}{2})^2 + i\alpha\xi] \\ \cdot \exp[\alpha s - \frac{\alpha\xi^2}{2} + i(-\frac{\xi^3}{12} + \frac{\alpha^2\xi}{2} + \frac{s\xi}{2})] \end{aligned} \tag{1.19}$$

Alternatively, in physical coordinates, in a medium with $n = 1$, the propagation of the Airy beam is described by:

$$\begin{aligned} u(x,z) = Ai[\frac{x}{w_x} - (\frac{z}{2kw_x^2})^2 + \frac{i\alpha z}{kw_x^2}] \\ \cdot \exp[\frac{\alpha x}{w_x} - \frac{\alpha z^2}{2k^2 w_x^4} + i(-\frac{z^3}{12k^3 w_x^6} + \frac{\alpha^2 z}{2kw_x^2} + \frac{xz}{2kw_x^3})] \end{aligned} \tag{1.20}$$

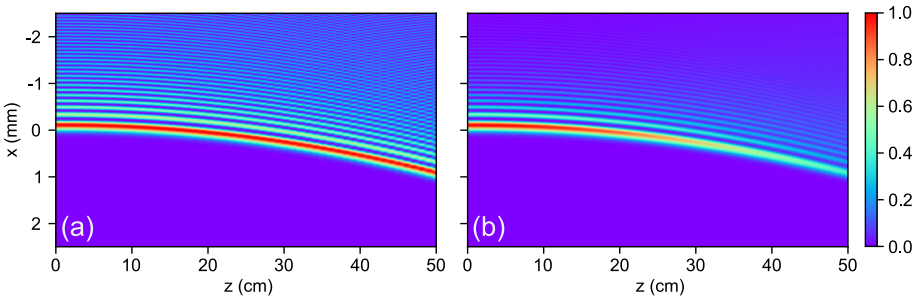

Figure 1.9: Intensity distribution along propagation of (a) an ideal Airy beam ($\alpha = 0$) with transverse scale parameter $w_x = 100$ μm, and (b) and Airy beam with $w_x = 100$ μm, and apodization factor $\alpha = 0.05$.

In the case of an ideal Airy $a = 0$ so as it can be easily seen from the Airy function arguments [¶] in Eqs. (1.19), (1.20) the distribution is invariant along a parabolic trajectory. On the other hand, when $a > 0$ the amplitude of the distribution decays as the beam propagates mainly due to the factor $\exp(-\frac{\alpha z^2}{2k^2 w_x^4})$. For sufficiently small values of the truncation parameter $0 < a \leq 0.5$ this decay is very slow so the beam preserves it's non-diffracting properties for a considerable propagation distance. From Eq. (1.20) we can estimate that the peak intensity will drop to half of it's original value at a distance $z_{max} = \frac{kw_x^2}{\sqrt{a}}\sqrt{2\ln 2}$. Compared to the Rayleigh range of a Gaussian beam with a beam waist $w_0 = w_x$ this distance is larger by a factor $\sqrt{2\ln 2}/\sqrt{a} \sim 1.18/\sqrt{a}$. If the Gaussian beam has the same (FWHM) with the primary Airy lobe then this ratio is slightly different $\sim 1.26/\sqrt{a}$.

Fig. 1.9 depicts a numerical simulation [10] of the $I(x, z)$ intensity distribution of an ideal and a truncated Airy beam along its propagation. The beam parameters in this case are: transverse scale parameter $w_x = 100$ μm, apodization factor $\alpha = 0.05$, and wavelength $\lambda = 0.8$ μm. Besides the parabolic trajectory, Airy beam also preserves the non-diffracting characteristic of an ideal Airy beam. As we can observe from Fig. 1.9 the intensity of the main lode (the maximum intensity feature) is slowly decreasing as it propagates dropping to half of it's original in intensity at $z \sim 43.5$ cm. This distance is by a factor of ~ 6 longer compared to that of a Gaussian beam having the same FWHM as that of the main lobe of the Airy beam [24]. The extension of the 1D Airy beam to it's 2 dimensional counterpart is straightforward [24], thus the initial field distribution in the transverse plane is given by:

$$u(x, y, z = 0) = Ai(\frac{x}{w_x})Ai(\frac{y}{w_y})\exp(\alpha_x \frac{x}{w_x})\exp(\alpha_y \frac{y}{w_y}) \tag{1.21}$$

where, w_x, w_y being the transverse scale parameters in x, and y directions

[¶] $Ai[s - (\frac{\xi}{2})^2]$, $Ai[\frac{x}{w_x} - (\frac{z}{2kw_x^2})^2]$

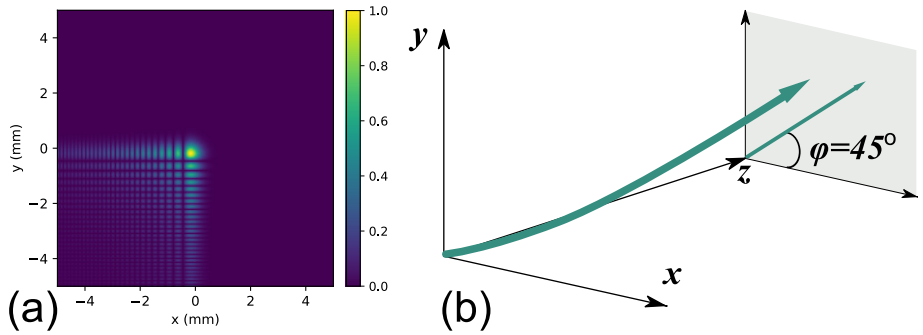

Figure 1.10: (a) Transverse amplitude distribution at the initial plane ($|A(x, y, z = 0)|$), of a 2D Airy beam with $w_x = w_y = 200$ μm and $\alpha_x = \alpha_y = 0.05$, and (b) graphical representation of the main lobe trajectory of the 2D Airy beam.

respectively, and α_x, α_y are the corresponding apodization factors. The transverse amplitude distribution $A(x, y)$, at the initial plane ($z = 0$), of a 2D-Airy beam is shown in Fig. 1.10(a). Likewise, if the 2D-Airy beam has the same scaling parameters $w_x = w_y$ and apodization factors $\alpha_x = \alpha_y$, the trajectory of the beam's main lobe is a parabola with a projection in $x - y$ plane which is a straight line oriented at 45^o as shown in Fig. 1.10(b).

1.2.3 Radially symmetric Airy beams

A radially symmetric Airy beam, where the radial distribution is described by the Airy function, was also recently proposed [26, 25, 27]. In this case the amplitude is described by:

$$u(r, z = 0) = Ai(\frac{r_0 - r}{w}) \exp(\alpha \frac{r_0 - r}{w}) \tag{1.22}$$

where r is the radial coordinate, r_0, and w are the radius and width parameters of the main ring, and α is the apodization factor. This radially symmetric Airy variant, referred to as ring-Airy beam or circular Airy beam (CAB), due to its unique properties has drawn a lot of attention since it was first introduced. Among others it exhibits an abrupt autofocus with high intensity contrast along propagation [26, 25, 27]. Although diffracting it self heals [28] when it is partially blocked. Fig. 1.11(a) shows the transverse amplitude profile of a ring-Airy beam. The beam parameters are: $r_0 = 1.5$ mm, $w = 100$ μm, $\alpha = 0.05$, and $\lambda = 0.8$ μm. Likewise, Fig. 1.11(b) depicts the $I(x, z)$ intensity distribution along propagation where the parabolic trajectory of the primary ring and the abrupt autofocus of the beam are clearly visible.

Moreover, since ring-Airy beams retain low intensity until their abrupt autofocus, non-linear phenomena, that depend on intensity, are affecting the

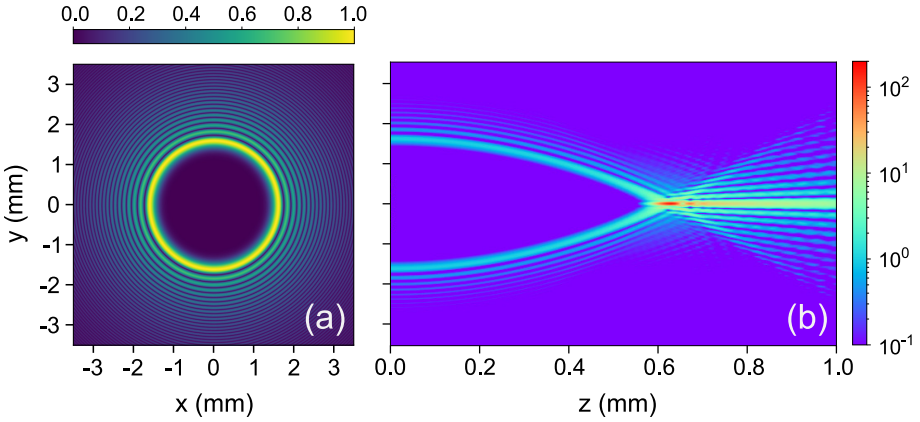

Figure 1.11: (a) Transverse amplitude distribution at the initial plane ($|A(x, y, z = 0)|$), of a ring-Airy beam with radius and width parameters $r_0 = 1.5$ mm, and $w = 100$ μm respectively, apodization factor $\alpha = 0.05$, and wavelength $\lambda = 0.8$ μm, and (b) $I(x, z)$ intensity distribution along the propagation of the ring-Airy beam.

beam propagation dynamics only at the focal region. As it has been recently shown, in the non-linear propagation regime they are transformed to non-linear intense light-bullets [29]. Likewise, compared to Gaussian beams, they show improved results when used for the generation of THz radiation [30]. Furthermore, their characteristic needle-like shaped focal voxel remains practically constant with respect to the focal position. This property is very advantageous for multi-photon polymerization Direct Laser Writing (DLW) applications, especially for the fabrication of high aspect ratio 3D structures at long working distances [31].

1.2.4 Light beams carrying Orbital Angular Momentum

Another category of structured light beams is that of light beams carrying Orbital Angular Momentum (OAM) also referred to as vortex beams. Let us begin by introducing the optical vortex [32, 33]. The phase distribution

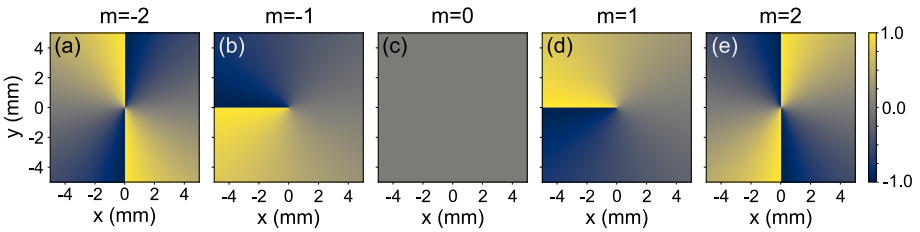

Figure 1.12: Phase distribution of optical vortices with various values of topological charge $m = -2, ..., 2$ (a)-(e).

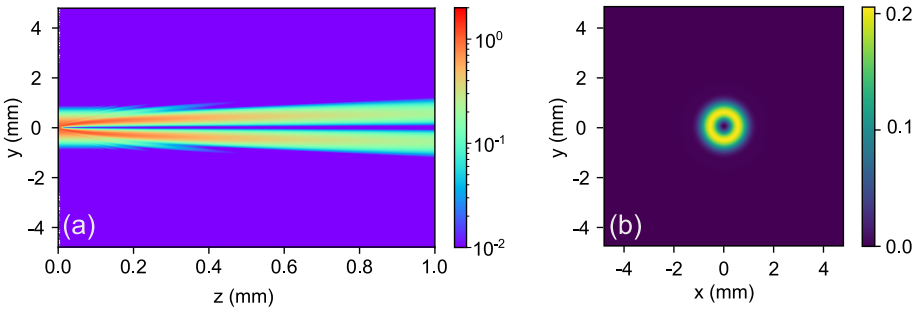

Figure 1.13: (a) Intensity cross-section $I(y, z)$ along propagation, and (b) transverse intensity profile $I(x, y)$ at $z = 1$ m of a Gaussian vortex beam with FWHM = 1 mm and topological charge $m = 1$. (Numerical simulation results [10]).

of a wave that carries a vortex is similar to a helix. Such a wave can be described (in the paraxial regime) as:

$$u(\rho, \phi, z) = A(r, \phi, z) \exp(im\phi) \tag{1.23}$$

where $\mathrm{A}(r, \phi, z)$ is the amplitude, r is the radial coordinate, ϕ is the azimuth angle, and z is the propagation direction. The phase term $\exp(im\phi)$ is a helical phase that describes the vortex, while m is the topological charge. The intensity of such waves is zero on the optical axis $I(r = 0, z) = 0$ due to destructive interference [32] resulting to a beam with a doughnut shaped transverse intensity profile. In 1992 Allen et al. [34] showed that such light carries orbital angular momentum (OAM) by using a Laguerre-Gaussian mode description and comparing it with the eigenfunction of the projection, along z axis, of the orbital angular momentum operator L_z in quantum mechanics [5]. This approach was another example of using the analogy between quantum mechanics and paraxial wave optics to describe a physical phenomenon. Actually, optical vortices carry an OAM of $m\hbar$ per photon. The phase distribution of optical vortices with $m = -2, ..., 2$ is depicted in Figs. 1.12(a)-(e). Note, that the abrupt discontinuities in the phase are due to the presence of the vortex and their number is equal to the absolute value of the topological charge $|m|$.

Light beams can carry OAM as inherent property, like for example Laguerre - Gaussian (LG) beams [34], or OAM can be imposed by imprinting a vortex in the phase of any light beam. Moreover, higher order Bessel beams $J_n(r)$, $(\forall\, n > 0)$ also carry OAM. In this case the topological charge is equal to the order of the Bessel function $m = n$. On the other hand, by imprinting a helical phase $\exp(im\phi)$ we can impose OAM to any light beam, like for example a ring-Airy beam that is transformed to a ring-Airy vortex beam [35].

In Figs. 1.13, 1.14 we depict two examples of such vortex beams. In more

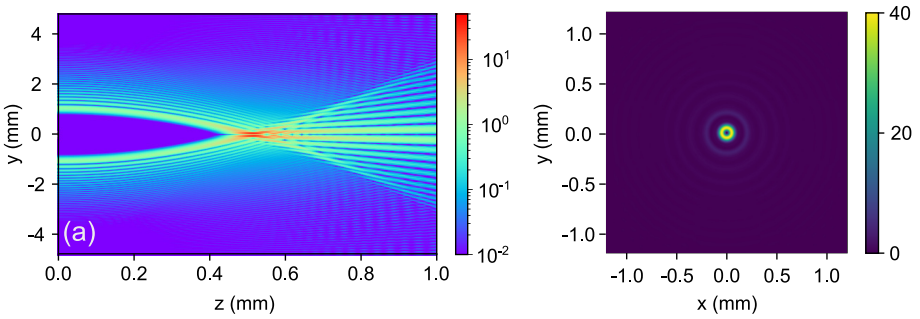

Figure 1.14: (a) Intensity cross-section $I(y, z)$ along propagation, and (b) transverse intensity profile $I(x, y)$ at $z = 520$ mm of a ring-Airy vortex beam with $r_0 = 1$ mm, $w = 100$ μm and topological charge $m = 1$. Numerical simulation results [10].

detail, Fig. 1.13(a) shows the intensity distribution along propagation of a Gaussian beam with an imprinted helical phase $u(x, y) = G(x, y)\exp(im\phi)$ with $FWHM = 1$mm, and $m = 1$. Moreover, Fig. 1.13(b) shows the transverse intensity profile $I(x, y)$ at a propagation distance of $z = 1$ m, of the Gaussian vortex beam, where we can observe the characteristic doughnut-like shape. When a helical phase is imprinted to an abruptly auto-focusing ring-Airy beam, the abrupt autofocus is unaffected, as shown in Fig. 1.14(a). Likewise, the characteristic doughnut-like intensity profile is clearly visible in the focal region as shown in Fig. 1.14(b).

1.2.5 Light beams with exotic distributions

In addition, there is also another category of distinctively shaped beams that, although are not all non-diffracting, exhibit interesting and useful properties. Here, we will show a few of them and discuss about their properties and their applications.

Mathieu beams

One of the first alternatives of a non-diffracting after the first realization of the Bessel beam, were the Mathieu beams that were proposed and experimentally demonstrated by J.C.Gutiérrez-Vega et al. [36, 37]. The distribution of a Mathieu beam, in elliptical cylindrical coordinates[‖], is described:

$$u(\xi, \eta, z; q) = Ce_0(\xi; q)ce_0(\eta; q)\exp(ik_z z) \tag{1.24}$$

[‖] In elliptical cylindrical coordinates $x = h\cosh(\xi)\cos(\eta)$, $y = h\sinh(\xi)\sin(\eta)$, and $z = z$, where $\xi \in [0, \infty)$ and $\eta \in [0, 2\pi)$ are respectively the radial and angular variables and $2h$ is the interfocal separation.

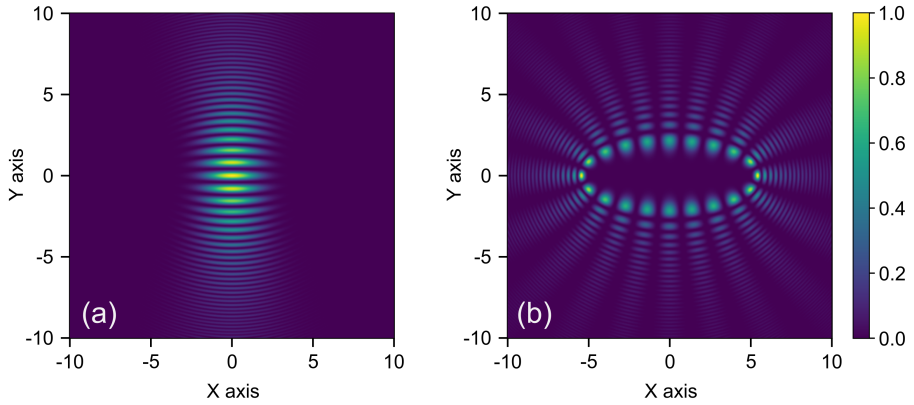

Figure 1.15: Normalized transverse intensity profiles of Mathieu beams with $h = 5$, $q = 25$ and (a) $m = 0$, (b) $m = 10$.

where, Ce_0 is the even radial Mathieu function of the first kind, while ce_0 is the angular Mathieu function, ξ and η are the radial and angular variables respectively, q is a parameter associated with the ellipticity of the coordinate system, and k_z is the magnitude of the longitudinal component of the wavevector. Fig. 1.15 shows typical transverse intensity distribution of Mathieu beams with parameters: $h = 5$, $q = 25$ and Fig. 1.15(a) $m = 0$, Fig. 1.15(b) $m = 10$. Mathieu beam is a non-diffracting solution of the wave equation in elliptical-cylindrical coordinates and is described by the radial and angular Mathieu functions as shown in Eq. (1.24). Since non-diffracting Mathieu beams contain infinite energy, and therefore are not feasible, a truncated version of finite energy, where the initial field is clipped by a circular aperture, was proposed [38]. Mathieu beams have been used in a few applications as an alternative optical tool. For example, such beams were used as light moulds for 3D microparticle structures [38], while femtosecond Mathieu Beams were used for fabrication of complex 3D microcages [39].

Pearcey beams

A more recently introduced exotic beam with interesting properties is the Pearcey beam [40]. These beams are based on the Pearcey function that describes the cusp caustic formed when light experiencing spherical aberration [40] is focused. The Pearcey function is defined by the Pearcey integral:

$$P(x_2, x_1) = \int_{-\infty}^{\infty} \exp[i(t^4 + x_2 t^2 + x_1 t)]dt \tag{1.25}$$

where x_1 and x_2 represent the two dimensionless orthogonal variables that are perpendicular to the propagation axis. The Pearcey beam, although diffracting, exhibits a form-invariant behavior as well as auto-healing along

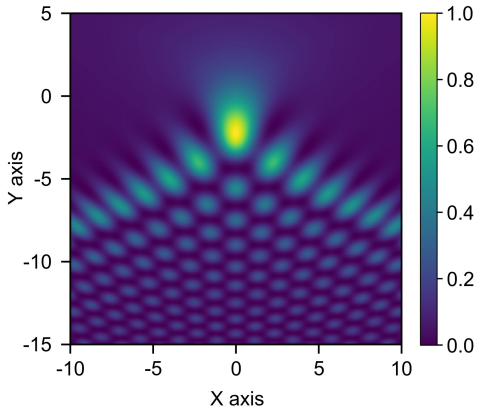

Figure 1.16: Normalized transverse intensity profile of a Pearcey beam.

propagation. The first experimental observation of such beams was presented by J.D Ring et al. in 2012 [40]. In Fig. 1.16 a typical normalized transverse intensity profile of a Pearcey beam is depicted. Furthermore, an extension of the Pearcey beams was proposed and it's propagation dynamics were theoretically investigated in 2018 by X. Chen et al. [41]. In this work a radially symmetric counterpart of Pearcey beam that exhibits auto-focusing behavior similar to that of the radially symmetric Airy beams [26, 42] was demonstrated.

1.3 Structured light for materials science applications

Light finds use in various fields of science and technology. Applications range from metrology, imaging and telecommunications to materials processing. In metrology, light is utilized in order to measure material properties using interferometric, spectroscopic, and other techniques [43, 44, 45, 46, 47]. Moreover, in imaging, light is used for detection, identification and data retrieval. Furthermore, either pulsed of continuous, light beams can provide a volatile tool for the processing of materials in order to cut, structure, or change their properties. Although quite often, a Gaussian beam is utilized for these applications, nevertheless there are several examples in bibliography where a structured light beam is used [48, 30, 49, 39] showing improved results. Especially, when the goal is the efficient energy delivery on a remote target, structured light is a suitable means to achieve this. In Fig. 1.17 we depict an illustration of a device that modulate an incoming wave to create structured light that is afterwards used for materials processing. Such a device can be a simple optical element, a more advanced Spatial Light Modulator (SLM), a device consisting of linear and non linear optical elements, or a combination

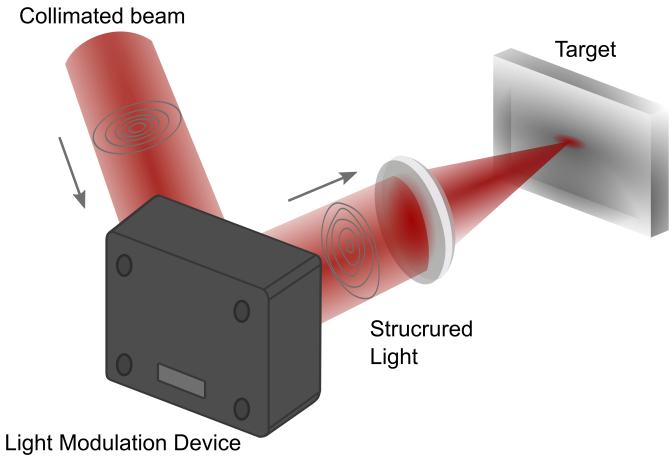

Figure 1.17: Illustration of a typical scheme for light structuring in materials processing applications.

of all of the above.

In materials science applications there is a variety of cases where wave-packets are modulated in their spatial distribution of amplitude, phase, or polarization state, as well as in their temporal profile, such structured light beams have been used and showed improved results [42, 31, 50, 51]. For example, wave-packets, spatially shaped to transform into ring-Airy beams [26, 42], have been employed for the manufacturing of large three-dimensional

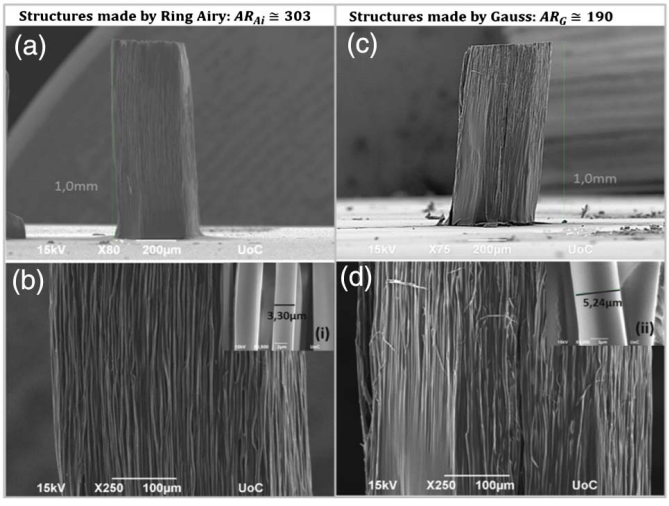

Figure 1.18: Fabricated structures using ring-Airy beams (a,b) and Gaussian beams (c,d): SEM images of hexagonal structures (1 mm in height). Image reprinted from [31] with permission from the authors.

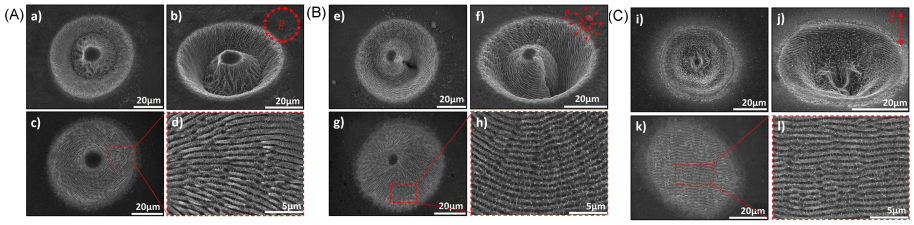

Figure 1.19: SEM images of LIPSS using CV beams with azimuthal (a–d), radial (e–h) and linear (i–l) polarization. Image reprinted from [53] with permission from the authors.

structures with high resolution using multi-photon polymerization [31]. In particular, using the needle-like focal voxel of ring-Airy beams, structures with high aspect ratios were fabricated, exhibiting better results compared to those were the structures were fabricated using conventional Gaussian beams as shown in Fig. 1.18.

Furthermore, there are several materials processing applications where the temporal profile of a wave-packet is modulated [50, 52]. Although this thesis is focused in spatial shaping, it is essential to mention a few applications of temporal light shaping. In 2016, a group in the University of Kassel [50] demonstrated the generation of uniform ablation structures with high aspect ratios in fused silica using temporally shaped Airy wave-packets. In more detail, they compared the ablation results of a 30fs Gaussian pulse with one that was stretched to transform into a temporal Airy pulse of 1.5ps. They observed that when using such temporal structuring the ablation crater that was created was more uniform and with higher aspect ratio reaching values $30:1$ (depth:width).

Furthermore, another crucial parameter that can be controlled is the polarization of a beam. Different polarization states can produce remarkably different results in various materials processing applications [54, 55, 56]. For instance, cylindrical vector (CV) femtosecond laser beams have been used for complex surface structuring [53]. In this work, a linearly polarized Gaussian fs pulse was shaped by a series of waveplates to acquire radial and azimuthal polarization. This resulted to a doughnut-like shape in their transverse intensity profile. These CV beams were used to process thin Ni films (thickness $\sim 100\ \mu$m) to produce LIPSS [**] with their characteristic texture aligned perpendicular to the polarization vector. A typical result of this work is presented in Fig. 1.19.

[**]Laser-Induced Periodic Surface Structures (LIPSS).

1.4 Coherence of light

Based on its electromagnetic nature light is often described as a synchronous oscillation of the electric and magnetic field. In a homogeneous and isotropic medium the two fields are transverse to each other and perpendicular to the propagation direction [3]. Besides the ideal case of a monochromatic harmonic plane wave that propagates along a direction, in a real physical system light is emitted from sources that are confined in space, and emit within a finite spectral content, usually distributed around a central frequency, or wavelength. Furthermore, each point on the spatial extent of the source emits in a somehow uncorrelated or weakly correlated way both in time, compared to a previous instance, and in space, compared to it's neighboring points [2, 57]. This effectively introduces random phase, and polarization, fluctuations [57] to the light field. The theory of coherence elucidates the fluctuations of optical fields in a rigorous manner [57, 58]. It this thesis, we experimentally studied the effect of coherence on the properties of accelerating optical beams. In the following, we are going to present the foundations of coherence theory, in a non exhaustive way, introducing all the important physics that are involved to properly interpret the experimental results. In this context, it is more convenient to present the concepts of spatial and temporal coherence independently [7], an approach we are going to follow in this thesis.

1.4.1 Temporal coherence

Temporal coherence is directly linked to the finite extend of the spectral content of a light beam. It represents a quantitative measure of the self-correlation of a wave in time, namely the correlation of a wave, at a specific

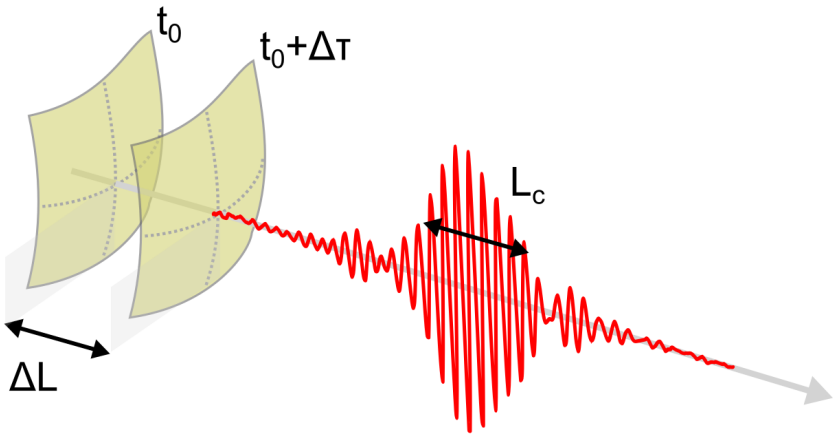

Figure 1.20: Illustration of temporal coherence of a wave.

point in space, at a reference time t_0 with the evolution of the same wave after a finite period of time Δt. The effect of temporal coherence becomes apparent in an interference experiment. For example, in a Michelson interferometer [7], the wave is splitted into two parts and a variable time delay is imposed between them. Afterwards, when the two parts are combined again their superposition depends on the time delay, or the optical path difference $\Delta L = c\Delta t$, where c is the velocity of light. This process is graphically depicted in Fig. 1.20, where it is visible that interference effects are observed within a time delay or an optical path difference range, which we refer to as coherence time t_c and coherence length $L_c = c\Delta t_c$ respectively. According to coherence theory [57], the coherence length depends on the spectral bandwidth of the source. For quasi-monochromatic source the coherence length is [7, 57]:

$$L_c = \frac{\lambda_0^2}{\Delta\lambda}$$

where λ_0 is the central wavelength and $\Delta\lambda$ is spectral width measured at FWHM of the wavelength distribution. For example, a diode that emits at a central wavelength of $\lambda_0 = 1$ μm and spectral bandwidth of $\Delta\lambda \simeq 50$ nm has a coherence length $L_c \simeq 20\mu$m [59], while a continuous wave (CW) laser, due to it's very small spectral bandwidth ($\Delta\lambda \ll \lambda_0$), exhibits considerably longer coherence lengths, ranging form a few millimeters to hundreds of meters [60, 61].

1.4.2 Spatial coherence

Spatial coherence, on the other hand refers to the correlation of different point emitters in a source at the same time. Likewise, the effect of spatial coherence becomes apparent by an interference experiment, particularly the well-known double slit Young's experiment where we split the wave in question into two identical parts passing through two distinct slits, or pinholes. When the two parts are recombined, the superimposing fields result to interference fringes. In more detail, let's begin by assuming that a light source, of square shape and side Δx, illuminates an opaque screen, that contains two pinholes P_1 and P_2 and is located a distance R. According to coherence theory [57], we can observe interference fringes onto the screen if only the two pinholes are inside the spatial coherence area defined as [57]:

$$\Delta A \sim \frac{R^2}{S}\lambda_0^2$$

where $S = \Delta x^2$ is the surface area of the source, and λ_0 is the central wavelength of the light emitted from the source. For example, an incandescent lamp has a spatial coherence area in the order of 1 μm^2, and a typical white-light LED has a coherence area of few μm^2, while a laser is considered fully spatially coherent within the whole beam diameter.

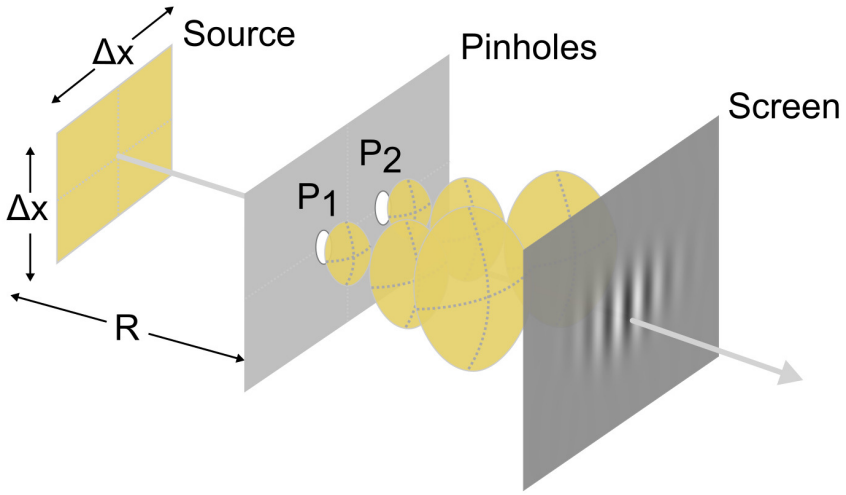

Figure 1.21: Illustration of the manifestation of spatial coherence of a wave in a typical Young's experiment.

Spatial coherence is often described by the equal-time mutual coherence function (EMCF), also referred to as mutual intensity function, between two arbitrary points [58, 62]. The EMCF takes values between 0 and 1, with the lower limit referring to spatially incoherent while the upper limit refers to spatially coherent light. Interestingly, according to the van Cittert-Zernike theorem [2] the propagation of the EMCF is described by a wave propagation equation. Thus EMCF spreads as it propagates, similarly to a wave that diffracts. In this context, the evolution of the EMCF of an incoherent light source of size S can be described in a similar way to the diffraction of a wave from an aperture of the same size. Thus, a convenient method to increase the spatial coherence of a light beam is the spatial filtering, namely passing incoherent light through a small aperture [57]. In this case the spatial coherence of the diffracted beam is inversely proportional to the size of the aperture.

In particular, for light emitted by a circular source of radius a in a plane located at a distance $R >> a$ the absolute value of EMCF between two points P_1, P_2 is described by:

$$|j(p_1, p_2)| = \frac{2J_1(v)}{v} \tag{1.26}$$

where J_1 denotes the first order Bessel function of the first kind, and v is a parameter described by:

$$v = \frac{2\pi a}{\lambda_0 R} d_{12}$$

where d is the distance between the two points, and λ_0 is the central wavelength. From the above it is straightforward to estimate the FWHM of the

coherence area by setting $|j(p_1, p_2)| = 0.5 \Rightarrow v \simeq 2.25$ thus the coherence area will be:

$$d_{12} \simeq 2.25 \frac{\lambda_0}{\pi a} R \tag{1.27}$$

To summarize, as described by Eq. (1.27), the spatial coherence length d_{12} is proportional to the central wavelength λ_0 and to the propagation distance R and inversely proportional to the size of the source.

2 | Design and engineering of structured light

Customised optical fields, referred to as structured light, can provide significant advantages in applications since their focal distribution and propagation dynamics can be tailored. Customisation can be performed by, independently or in combination, spatially modulating the amplitude, the phase, or the polarization of the light wave [6]. Such an optimization process involves two stages, firstly the design and engineering and then the generation of structured light.

The first stage involves the selection of the optimal distribution (amplitude, phase and polarization) of the structured light beam for a specific application. For instance, several examples exist in the bibliography where structured light was adopted [63, 48, 31, 49, 30, 39] resulting to notably better results. From these demonstrations it is obvious that the optimal structured light depends on the application. In cases where longer foci are required Bessel beams prevail compared to Gaussian beams, with the drawback of a much lower intensity contrast at the focal region. Based on this fact and in correspondence to the field of medicine where a wide variety of scalpels is used, it is clear that also a variety of light beams with different focal distributions should be readily available to the optical engineer. The design of structured light that will lead to a variety of tailored focal distributions and the requirement to be able to function in the linear and the non-linear propagation regime makes the task very difficult for iterative numerical optimization techniques.

On the other hand, an analytic approach to design such a toolbox is in principle possible by using non-diffracting beams, like Bessel or Airy beams. These beams exhibit intensity hot-spots that are a result of strong linear phase gradients and interference effects. Due to this, when the beam energy in increased, non-linear effects that depend on intensity are excited only locally near the intensity hot-spots and do not have a significant impact in the focal distribution. An ideal template to achieve this complex task is the recently introduced family of accelerating optical wave packets [19, 24, 26, 42], whose distribution is described by the Airy function. These structured light

waves propagate in curved trajectories [64], exhibit abrupt autofocus [42, 27] and are able to self-heal and bypass obstacles [65]. Furthermore, at high intensities they reshape into nonlinear intense light-bullets with extremely well defined focal position [29].

This design and engineering stage can involve either analytical approaches that rely on the manipulation of a discrete collection of template light distributions, or numerical iterative methods, or even a combination of them. In this chapter we will show that utilizing shaped accelerating beams, we can precisely tailor the focal voxel distribution over an extended working distance. By using analytical approaches, combined with a modular combination of template components, we provide a complete and versatile toolbox of light scalpels, that can be used in variety of applications. In particular, the template components of our toolbox are three: a) abruptly auto-focusing ring Airy beams [26, 42], b) the recently introduced abruptly auto-defocusing inverse ring Airy beams [27], and c) a conical phase gradient (CPG). The first two, enable us to finely tune the focal distribution, while the CPG that acts similar to an axicon [15] is used to control the focus position and an alternative to a lens in order to increase the intensity contrast at the focus. As we show, through numerical simulations, such an approach enables us to produce a double foci that can be independently tuned in terms of position as well as peak intensity, with the exiting feature of being uncorrelated in the presence of an obstacle. Likewise, by overlapping the two foci an sharp high contrast focus is formed.

2.1 Light Scalpels

The idea of using light as a scalpel comes from the field of medicine. There, instead of searching for the "optimal" tool, surgeons have developed a variety of scalpels that are optimal for specific operations. Comparing to the field of Optics, and more specifically structured light, we see that, although there is an equivalent versatility in the applications, most publications are still focused on finding the optimal, unique tool to replace all others. Furthermore, the proposed light distributions become more and more complex, require sophisticated and costly equipment like spatial light modulators (SLM) to be generated, and they are still far from being used from a non-optics specialist community. As we are going to show, bringing the idea of designing versatile light scalpels, that are based on a combination of a limited set of basic ingredients, can provide a complete toolbox to the optical engineer and enable a larger community to benefit from the exiting properties of structured light. Let's first review some of the light distributions that are available, i.e. light scalpels already in hand, and compare them in respect to their focal properties.

The most commonly used intensity profile is the Gaussian distribution.

Gaussian beams, are easy to handle, require no special equipment to generate them, and we can analytically describe their propagation through optical systems [2]. Likewise, they are easily focused to localized and intense foci, using a simple lens. On the other hand, their focal aspect ratio (ratio of focal width to focal length) depends on the focus position and in the non-linear regime the focus shifts towards the source as we increase the beam power [66]. The amplitude of Gaussian beams, at $z = 0$, is described by:

$$u_0(r, z = 0) = A_0 \exp(-\frac{r^2}{w_0^2}) \tag{2.1}$$

where A_0 is a the peak amplitude at $z = 0$, r is the radius in cylindrical coordinates and w_0 is the initial beam waist.

On the other hand, there exists a large variety of structured light beams that are optimized for specific applications. The first one of this kind is the Bessel beam [12, 13]. Bessel beams are non-diffracting solutions of the (2D+1) wave equation, and rely their properties on a conical shaped wavefront. Their transverse amplitude profile is described mathematically by Eq. (2.2) where J_0 is the Bessel function of the first kind and zero order, a is a constant and r is the radius in cylindrical coordinates. Their main characteristic is that they focus in a narrow, in the order of the wavelength, focal spot that does not spread due to diffraction as the beam propagates. An ideal non-diffracting Bessel beam would require infinite energy to be realized. Nevertheless, in practice the generation of finite energy Bessel-like beams is achieved in the case of Bessel-Gauss beams [67] where a Gaussian beam is shaped by a conical phase gradient. In this case, the beam is nearly non-diffracting so its focal spot does not spread over a propagation range, thus the elongated focus is finite in length. These beams are generated by using either a conical lens, referred to as axicon, [15] or by using active wavefront shaping devices such as a Spatial Light Modulators (SLM). Bessel-Gauss beams are not that easily handled through optical systems, for example their focus is distorted when focused by a lens, but analytical or semi-analytical predictions of this behavior are available [68, 18]. As in the case of all non-diffracting beams, the focus is generated by interference effects due to the conical phase gradient. Thus, compared to Gaussian beams, they are robust as their power is increased.

$$u_0(r, z = 0) = J_0(ar) \tag{2.2}$$

Another type of beam, that is the only non-trivial, non-diffracting solution of the (1D+1) wave equation [19, 24] is the Airy beam. Airy beams are described mathematically by the Airy function [64] and have exciting properties. As they propagate, their distribution remains unchanged following a parabolic trajectory, a property referred to as acceleration [64]. Furthermore, as all non-diffracting beams they have the ability to self-heal [65] after being

perturbed by an obstacle. Similarly to Bessel beams, an ideal non-diffracting Airy beam cannot be physically realized. A truncated, with finite energy, version of these beams can be generated by applying an exponential decay apodization [24]. Interestingly the Fourier transform of Gaussian beam with cubic phase modulation is an exponentially apodized Airy beam. While such 1D beams have been successfully applied in light sheet microscopy [69], a later introduced radially symmetric variation [26, 42] seems very promising in a greater range of applications. These variants, which are referred to as circular Airy beams (CABs) or ring-Airy beams, are described by the Airy distribution in the radial coordinate. Their most exciting feature is that they abruptly autofocus without the need of any focusing elements. Counterintuitively, these beams shrink down to a focal spot as they propagate, with their distribution following a parabolic trajectory, a property imparted by their 1D counterparts. These beams are generated by various approaches [42, 70, 30] using SLMs. Although diffracting, ring-Airy beams show self-healing characteristics since their foci is robust to perturbations introduced by obstacles [28]. In the non-linear propagation regime, they show negligible focal shift and are very robust as the power is increased [29], likewise their harmonics also autofocus [23] with overlapping foci. Furthermore, their behavior when propagating through optical systems is unique since two foci appear when focused by a lens [71]. Although interesting, and analytically predictable [72, 71] such a characteristic is not always desirable to applications. To address the problem of further focusing ring-Airy beams an alternative approach using a conical phase gradient was recently proposed [27]. Using this approach these beams can be further focused to create intense, controllable foci.

2.1.1 Focal aspect ratio

As shown in Fig. 2.1 the three basic light scalpels that we described seem complementary to each other. Gaussian beams, see Fig. 2.1(a), result to a localized rather short focal region. On the other hand Bessel-Gauss beams as shown in Fig. 2.1(c) result to a focus that is very long and not localized in the propagation direction. Ring-Airy beams, as shown in Fig. 2.1(b) bridge the behaviour of the previous two by resulting to needle like focal regions, with a degree of localization on the propagation direction. In order to quantify this behavior we will use the focal aspect ratio, which is defined as the ratio of the FWHM of the focus in the longitudinal (Δf) and the lateral (w) directions $A_R = \Delta f / w$. For a Gaussian beam this ratio can take values $A_R^G > 3$ while for the Bessel-Gauss typically is around $A_R^{BG} \sim 10^3 - 10^4$. Notably, ring-Airy beams with values of $A_R^{rAi} \sim 10^2$-10^3 [27] result in a focal aspect ratio that is between of that of the other two aforementioned beams $A_R^G < A_R^{rAi} < A_R^{BG}$. For this behavior to be clearly visible, we have chosen the parameters of all beams in Fig. 2.1 in such a way so that the beams have similar initial size and

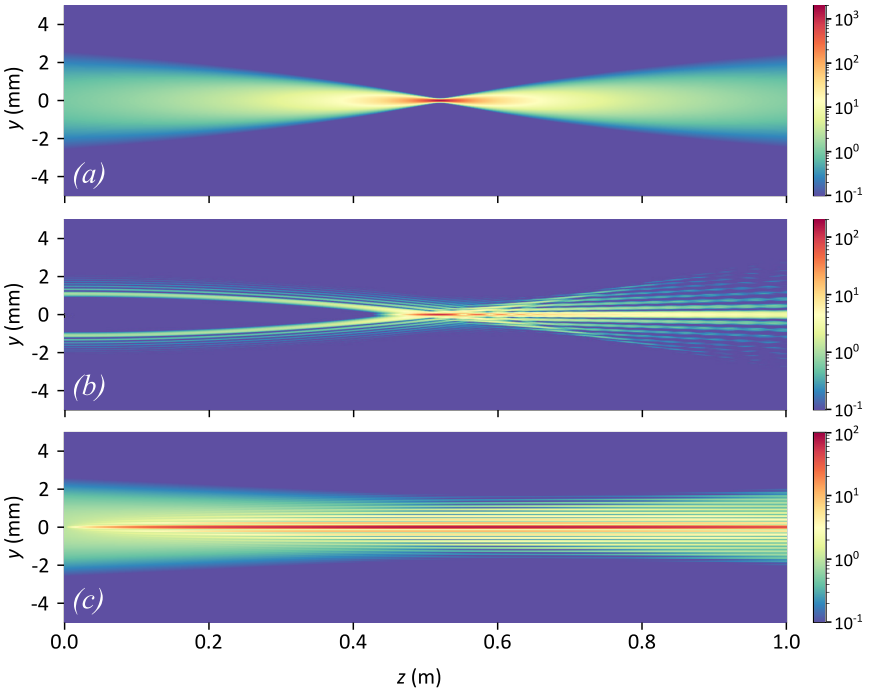

Figure 2.1: Intensity cross-section ($y-z$) of the propagation of various beams. (a) Gaussian focused by a lens, (b) a ring-Airy, and (c) a Gauss-Bessel beam.

focus at the same position. This approach resembles a typical application where, using finite sized optics, a light beam delivers energy to a remote target. Although the beam can in principle be structured, using and SLM for example, the finite size of the optics cannot be exceeded.

2.2 Accelerating beams as a template for light scalpels

As we mentioned in the introduction of this chapter Accelerating beam consist an ideal template for the generation of structured light. Specifically we utilize accelerating Airy beams, and variants of such beams for the creation of structured light. When Berry and Balazs showed, in 1979, that an Airy function is a non-dispersing solution of the Schröndiger equation in quantum mechanics [19], it was hard to imagine that, after nearly three decades, Siviloglou et al. will expand this result in the optical regime to generate non-diffracting, accelerating Airy beams [64, 24]. This interesting transition from Quantum Mechanics to Wave Optics was of course possible due to the mathematical equivalence of Schröndiger equation in Quantum Mechanics and the paraxial wave equation in Wave Optics 1.1.1.

2.2.1 1D, 2D and 3D Airy beams

Along with Bessel beams, 1D Airy beams and 2D Airy beams are nowadays the most widely used non-diffracting beams. Airy beams are intensity invariant over a parabolic trajectory along their propagation [64, 24] and self-heal [65]. These remarkable properties initiated many noteworthy applications ranging from curved plasma channels [73], and trapping and moving particles perpendicular to propagation axis [74], and using Airy beams in light sheet microscopy [49, 75]. In addition, if we take into account the temporal distribution of a wavepacket, we can shape its temporal profile in such a way to achieve a non-dispersing propagation. Combining temporal shaping and spatial structuring of a wavepacket, for non-dispersing and non-diffracting propagation one can create light that remain invariant along propagation. This has been done in 2010 in [76], where an Airy distribution used for the temporal component along with a 2D Airy spatial structuring, leading to spatiotemporal intense Airy-Airy-Airy (Airy3) light bullets. The spatiotemporal intensity of these light bullets is given by:

$$I(x,y,z,t) = \mathrm{Ai}^2(\pm\frac{x}{w_x})\mathrm{Ai}^2(\pm\frac{y}{w_y})\mathrm{Ai}^2(\pm\frac{\tau}{\tau_0} - \frac{(k_0'')^2 z^2}{4\tau_0^4}) \tag{2.3}$$

where Ai denotes the Airy function, x, y, and z are the coordinates in the transverse plane and along propagation, respectively, $\tau = t - (z/v_g)$ is the reduced time, v_g is the group velocity of the envelope of the light bullet, w_x, w_y, and τ_0 are constants associated with the two spatial and temporal widths of the wave packet, respectively, and $k_0'' = \partial^2 k/\partial\omega^2$ is the dispersion coefficient of the medium at the central frequency.

Furthermore, exploiting their accelerating nature and applying cylindrical symmetry the circular Airy beam (CAB) or ring-Airy was introduced [26, 42]. These beams have the exciting property of abruptly auto-focusing, i.e. diffraction leads instead of spreading to a focus. We will deal with this type of beams and their variations in detail in the following sections.

Airy and Gaussian beams, a Fourier Transform relation

As we have already described in the previous chapter (see 1.2.2) ideal Airy beams carry infinite energy, thus some king of truncation is necessary in order to materialize them. Siviloglou et al. have proposed [24] an exponential truncation:

$$u(s) = \mathrm{Ai}(s)\exp(\alpha s) \tag{2.4}$$

where $s = x/w_x$ is a transverse coordinate normalized with a scale parameter w_x that is associated with the width of the main lobe of the Airy beam, while $\alpha > 0$ is the truncation parameter, which ensures that the function is square integrable. Although other truncation functions are also possible,

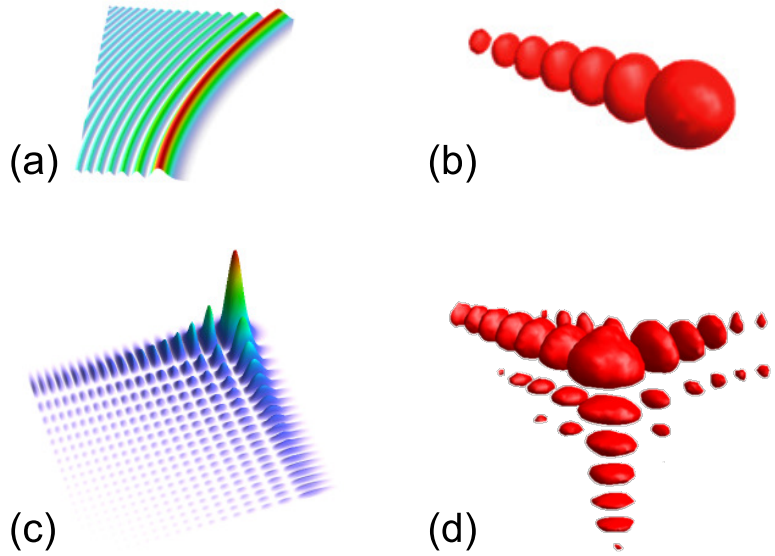

Figure 2.2: Members of the Airy beams family. (a) 1D Airy beam, (b) pulse with an Airy temporal distribution, (c) 2D Airy beam, (d) 3D Airy accelerating light bullet [76].

the exponential truncation has a unique property: it's Fourier transform is simply a Gaussian function with a cubic phase modulation [24]:

$$\Phi(k) = \exp(-\alpha k^2)\exp[\frac{i}{3}(k^3 - 3\alpha^2 k - i\alpha^3)] \tag{2.5}$$

where k is the spatial frequency. Furthermore, for small values of the truncation factor ($\alpha \to 0$) the above equation can be further simplified to:

$$\Phi(k) = \exp(-\alpha k^2)\exp(\frac{i}{3}k^3) \tag{2.6}$$

This relation shows that the Fourier transform of a Gaussian distribution modulated by a cubic phase distribution gives an exponentially truncated Airy function.

Why Airy beams are curved?

Admittedly, the most striking feature of the Airy beam is that it follows a curved trajectory along propagation. This trajectory is described by a parabola given in Eq. (1.20). A rigorous analysis of this behaviour is given in the original Berry and Balazs 1979 publication [19] where the Airy wavepacket was introduced for the first time. In a nutshell they showed that, viewed classically in phase space, an Airy wavepacket corresponds to a family of orbits that are represented by a parabola. Therefore, it is not any

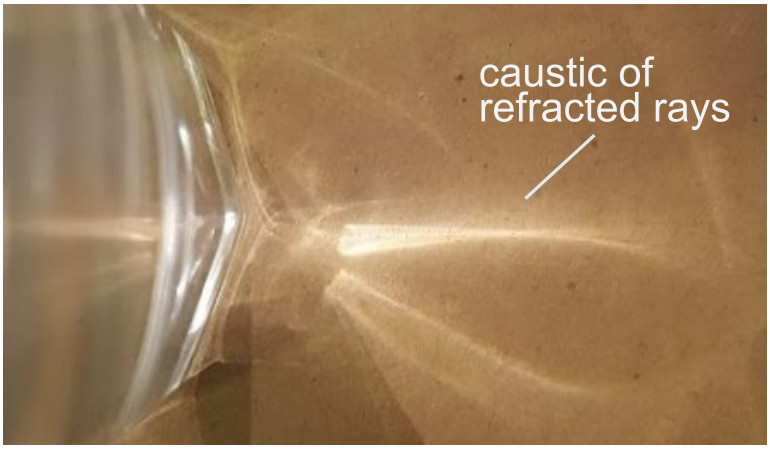

Figure 2.3: Image of a caustic which is formed when rays are refracted by a glass of water.

individual particle that accelerates in the Airy wavepacket but the caustic of the family of orbits. In a similar approach to the above mentioned classical analysis, light ray caustics (a geometrical optics concept) can also help us to reach to a physical understanding of the effect. To begin with, a caustic can be defined as a region to which tangent rays concentrate [77]. We often observe this phenomenon, when light passes through a curved refractive surface, like the ripples on water surface, or a droplet. An everyday example of caustic formation is shown in Fig. 2.3 where rays of light pass through a glass of water. In more detail, as we know [2] in an isotropic medium optical rays are perpendicular to the wavefront, which in shape is the *"mirror image"* of the corresponding phase distribution, as it is graphically shown in Fig. 2.4(a). Moreover, Fig. 2.4(b) shows a spherical wavefront, and the cor-

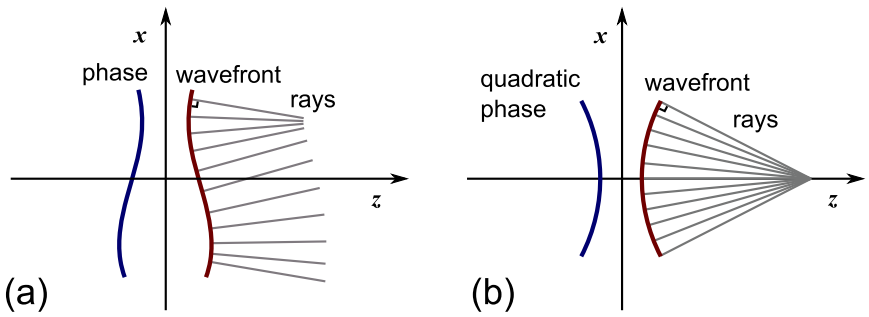

Figure 2.4: Graphical representation of a wavefront with the corresponding optical rays and phase distribution. (a) Arbitrary wavefront, and (b) Spherical wavefront. Note that in this case the phase distribution is described by a quadratic function.

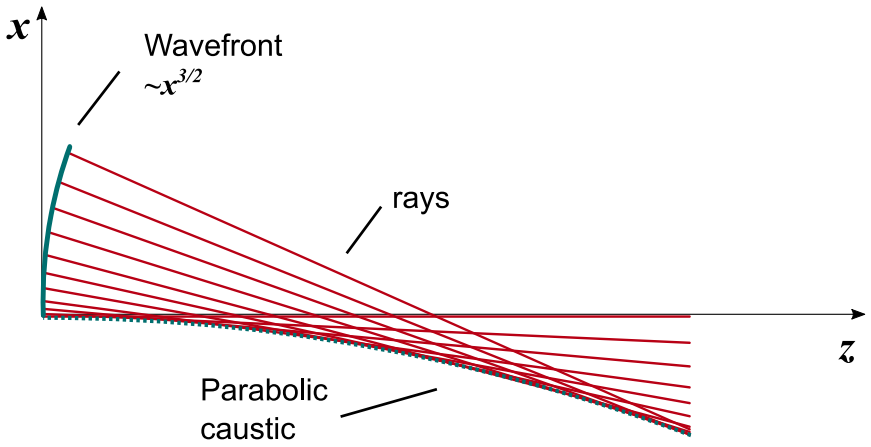

Figure 2.5: Illustration of a wavefront resulting from a $x^{3/2}$ phase distribution. Note that in this case the optical rays form a parabolic caustic. (Raytracing simulation results)

responding a quadratic phase distribution. Note that similar to the action of a lens, all rays converge to a single point which we refer to as the focus.

In this context, by properly shaping the wavefront, we can direct optical rays in such a way so that they follow any trajectory [78]. To apply this concept in the case of the Airy beam we will use a known approximation of the Airy function is [22, 19]:

$$\mathrm{Ai}(x) \sim \frac{1}{x^{1/4}} \exp(iCx^{3/2})$$

where C is a constant. As one can observe, the Airy function can be de-

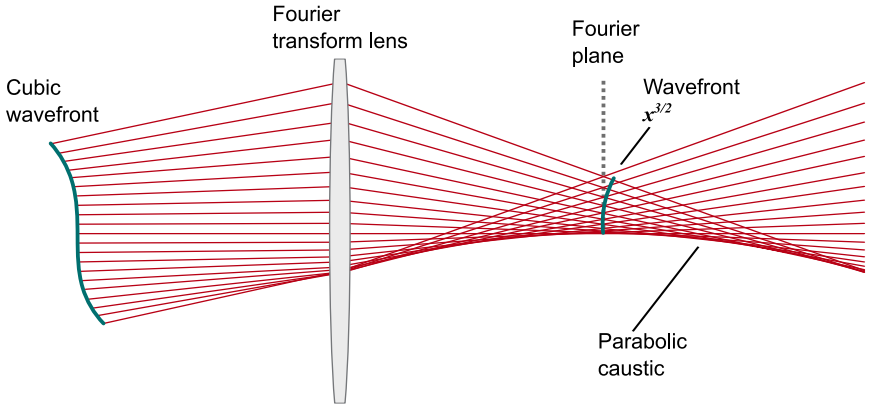

Figure 2.6: Illustration of how an Airy beam can be formed as a result of a caustic of rays. In this case a cubic phase modulated wavefront is Fourier transformed by a lens, resulting to a $x^{3/2}$ phase distribution at the Fourier plane. (Raytracing simulation results)

scribed by an oscillating term $\exp[i\phi(x)]$, where $\phi(x) = Cx^{3/2}$ is the phase distribution, and a decaying amplitude $(1/x^{1/4})$ term. Let's focus now only on the phase distribution and ignore the amplitude decay [79]. Since optical rays are perpendicular to the wavefront we can estimate each ray's direction $\hat{\mathbf{r}}(x)$, by differentiating over the phase distribution $\frac{\partial\phi(x)}{\partial x}$ we get for the Airy distribution:

$$\phi'(x) = \frac{3}{2}Cx^{1/2}$$

Following, the slope of the rays will be:

$$\hat{\mathbf{r}}(x) \propto x^{1/2}$$

As it is graphically visualized through raytracing in Fig. 2.5 these rays form a caustic that is described by a parabola. Furthermore, it is straightforward to show that such a phase distribution $\phi(x) \sim x^{3/2}$ can be generated by Fourier transforming a wavefront with a cubic phase distribution (x^3) *. This behaviour is depicted, using raytracing simulations, in Fig. 2.6. These results although only shown for the 1D case, for simplicity, they can be also generalized for the 2D Airy beam counterpart.

2.2.2 Abruptly auto-focusing beams

Any wave of finite dimensions will diffract [2, 7], and usually this means that it spreads at it propagates. Contrary to this common belief, there exist waves that instead of spreading they focus as they propagate, a behaviour referred to as auto-focusing. An annular beam, where light is emitted through a ring and leads to an needle-like focus is such an example. The introduction of accelerating waves has opened new dimensions to this field. Following parabolic trajectories such fields can result to auto-focusing with an abrupt increase of the intensity in the focal region. A straightforward example for this behaviour is the case of colliding 1D Airy beams [71, 80, 81, 82] where two 1D symmetrical Airy beams, superimpose. In more detail, two 1D Airy beams that are mirror symmetric with respect to the propagation axis, can result into an abrupt focus. Following symmetric parabolic trajectories these beams can either form an abrupt focus or form an elongated focal region. In both cases their characteristics, namely the focal position in the first case of the focal length for the latter, can be tuned by the Airy beam's parameters. The initial field distribution (at $z = 0$) of such beams is:

$$\begin{aligned} u_{col}(x,0) &= u(x,0) + u(-x,0) \\ u(x,0) &= \mathrm{Ai}\left(\frac{x-x_0}{w_x}\right)\exp\left(\alpha\frac{x-x_0}{w_x}\right) \end{aligned} \tag{2.7}$$

where x_0 is a transverse displacement, w_x is a constant, and α is the truncation parameter. An example of such waves is depicted in Fig. 2.7. In more

*A detailed analysis, using matrix theory, is given in 4.4.1

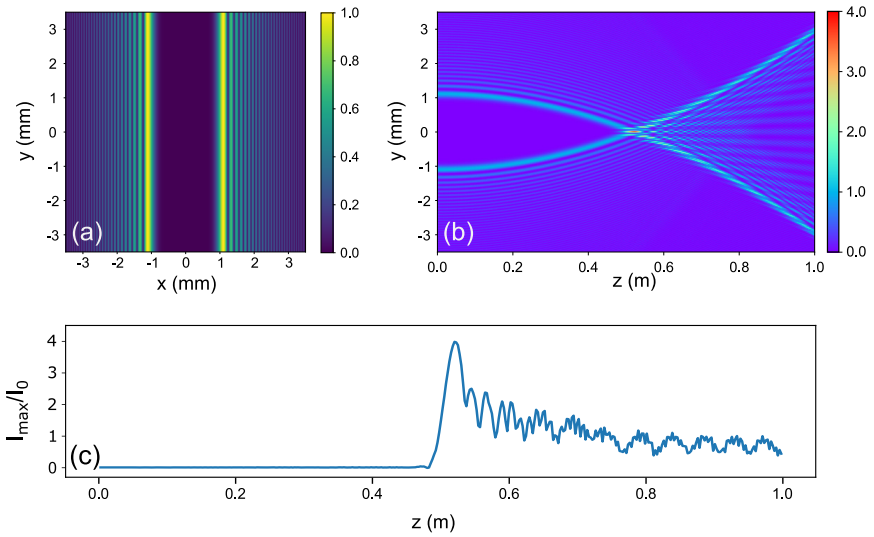

Figure 2.7: Colliding Airy beams with $w_x = 100$ μm, $x_0 = -1$ mm, and $\alpha = 0.05$ parameters. (a) Transverse $I(x, y)$ intensity profile at $z = 0$, (b) intensity $I(y, z)$ cross-section along propagation, and (c) maximum peak intensity along propagation normalized to the maximum intensity at the initial plane I_{max}/I_0. (Numerical simulation results [10].)

detail, Fig. 2.7(a) depicts the transverse (x-y) amplitude profile at the initial plane (z=0) of colliding Airy beams with $w_x = 100$ μm, $x_0 = -1$ mm, and $\alpha = 0.05$, while Fig. 2.7(b) shows the intensity $I(y, z)$ (y-z) cross-section along propagation, and Fig. 2.7(c) shows the maximum peak intensity along propagation normalized to the maximum intensity at the initial plane I_{max}/I_0 .

Radially symmetric Airy beams

A great enhancement of the abrupt auto-focusing behavior is achieved by applying the Airy distribution in the radial coordinate, thus generating a radially symmetric Airy beam [26, 42], referred to as Circular Airy beam (CAB) or ring-Airy beam:

$$u(r, z = 0) = Ai(s) \exp(\alpha s) \tag{2.8}$$

where $s = (r_0 - r)/w$, r is the radius in cylindrical coordinates, r_0, w are the radius and width parameters of the initial ring respectively, a is the truncation factor as before. The idea behind this is approach that each part of the ring-like structure that is formed will follow a parabolic trajectory towards the center thus resulting to an abrupt autofocus. The peak intensity at the focus can be orders of magnitude higher compared to the initial intensity [26, 42, 29].

In Fig. 2.8 the amplitude and phase of a ring-Airy beam is shown along with the corresponding intensity distribution along propagation. In more detail, in Fig. 2.8(a) we see the transverse $x-y$ cross-section of the amplitude of a ring-Airy at the initial plane ($z=0$), from which we observe the characteristic concentric rings that point outwards in decaying fashion. The radius of these rings decreases as the beam propagates until they collapse as shown in Figs. 2.8(b),(c) which shows the $x-z$ cross-section of intensity and the maximum peak intensity I_{max}/I_0 along propagation respectively, is depicted and show the abrupt auto-focusing property of the ring-Airy. Moreover, as we see from Fig. 2.8(c) the intensity contrast at the focus reaches values that exceeds $I_{max}/I_0 > 120$. This contrast in general depends on the ratio r_0/w and reaches it's maximum roughly at $r_0/w \sim 15$ [26]. Because of the mathematical complexity of the paraxial wave equation in cylindrical coordinates, an analytical relation for the propagation of such beams does not exist however a simple equation for the focus position can be derived [42], by using the analytical relation of propagation of the 1D Airy beam.

Ring-Airy beams have been used in various applications, especially in the field of materials science [31, 30, 29, 83]. Likewise, since non-liner effects depend on the intensity the ability of ring-Airy beams to maintain low, practically constant intensity along propagation until the formation of the high intensity focus, makes their propagation, compared to Gaussian beams,

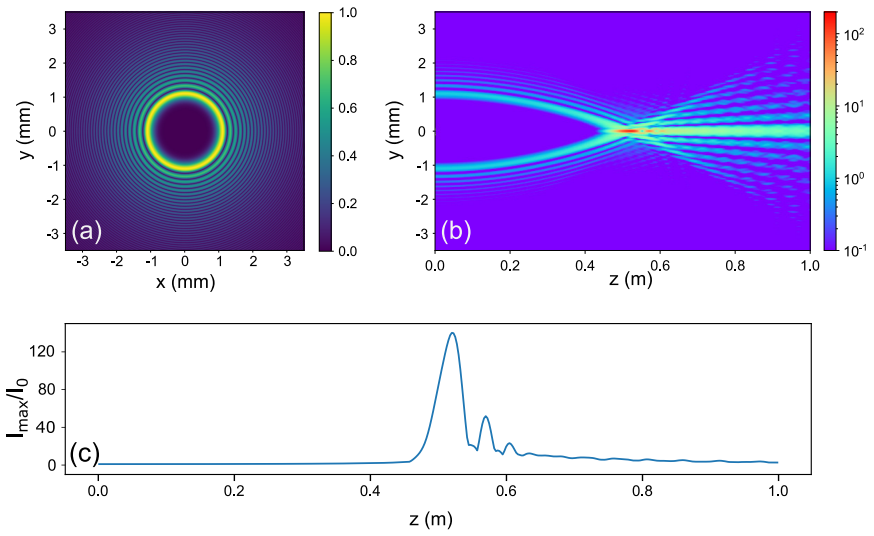

Figure 2.8: Ring-Airy beam (a) Transverse amplitude profile at the initial plane ($|A(x,y,z=0)|$), (b) the corresponding intensity $I(y,z)$ cross-section (Log-scale) along propagation, and (c) maximum peak intensity along propagation normalized to the maximum intensity at the initial plane $I_{max}(z)/I_0$. Numerical simulation results [10], beam parameters: $r_0 = 1$ mm, $w = 100$ μm, $\alpha = 0.05$, $b = 1$, and $\lambda = 0.8$ μm

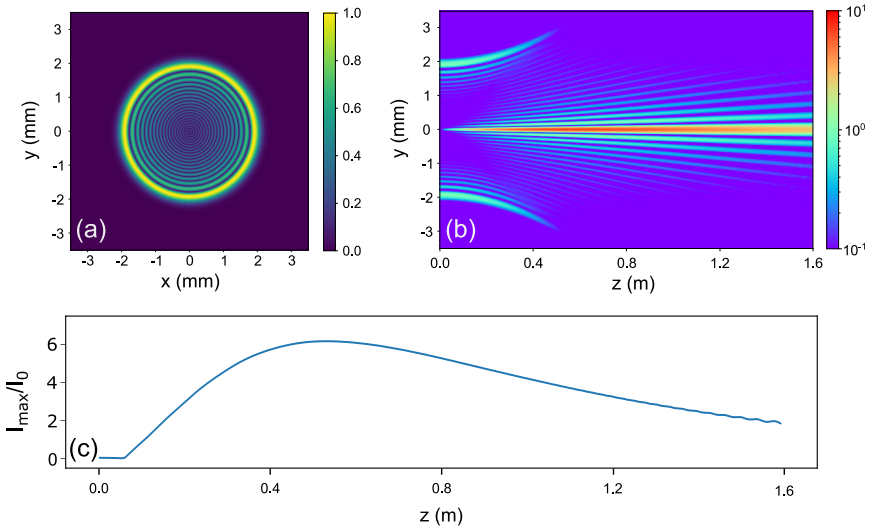

Figure 2.9: Inverse ring-Airy beam (a) Transverse amplitude profile at the initial plane ($|A(x, y, z = 0)|$), (b) the corresponding intensity $I(y, z)$ cross-section (Log-scale) along propagation, and (c) maximum peak intensity along propagation normalized to the maximum intensity at the initial plane $I_{max}(z)/I_0$. Numerical simulation results [10], beam parameters: $r_0 = 2$ mm, $w = 100$ μm, $\alpha = 0.05$, $b = 1$,and $\lambda = 0.8$ μm.

robust to nonlinearities [29].

Recently a variation of the ring-Airy beam, which we refer to as inverse ring-Airy, was introduced [84, 27]. These beams are also described by the Airy function in the radial dimension but, contrary to the ring-Airy, have their ring structure facing inwards. Both beams can be described in a unified manner:

$$u(r, z = 0) = Ai(bs)\exp(\alpha bs) \tag{2.9}$$

where b is a binary type parameter that takes only ± 1 values, and acts as a "switch" between the two variant beams. More specifically, for $b = 1$ Eq. (2.9) describes the auto-focusing ring-Airy, whereas for $b = -1$ Eq. (2.9) describes the inverse ring-Airy. In Fig. 2.9 the amplitude and phase of an inverse ring-Airy beam is shown along with the corresponding intensity distribution along propagation. In more detail, in Fig. 2.9(a) we see the transverse $x - y$ cross-section of the amplitude of an inverse ring-Airy at the initial plane ($z = 0$), from which we observe the characteristic rings that, contrary to the ring-Airy point inwards. Moreover, Figs. 2.9(b),(c) depict the $y - z$ cross-section of the intensity distribution and the normalized maximum peak intensity along propagation I_{max}/I_0, respectively, that show the resulting elongated focal region of the inverse ring-Airy, which is similar to the needle-like focal region of a Bessel beam [16, 18]. For the case of the inverse ring-Airy beam reaching to an analytical description of the propa-

gation it is quite complex because of the oscillatory behavior of the beam around its center [82, 84].

Radially symmetric Airy beams, with a conical phase

In order to further control the focusing properties of ring-Airy beams it is desirable to use some extra focusing mechanism. Using a simple lens leads to the formation of double foci [71] which is not always desirable. Recently we have introduced an alternative way to further control the focusing properties of ring-Airy beams by adding a conical phase gradient [27], equivalent to that introduced by an axicon [15]. The idea of this conical phase originates from the linear phase gradient [†]:

$$\Phi(x) = \exp(-i \sin\theta k x)$$

where θ is the angle, k the wavenumber. Such phase gradient is usually used to steer a light beam. in cylindrical symmetry this linear phase translates into a conical phase gradient:

$$\Phi(r) = \exp(-i \sin\theta k r)$$

where r is the radial coordinate in cylindrical coordinates (r, ϕ). Both of these phase gradients are depicted in Fig. 2.10 where it shows the linear, and conical phase along with their corresponding transverse $(x - y)$ phase distribution.

Following,expanding the generic description of ring-Airy and inverse ring-Airy beams of Eq. (2.8) by adding a conical gradient we get:

$$u(r, 0) = u_0 \mathrm{Ai}(bs) \exp(b\alpha s) \exp(-i \sin\theta k r) \tag{2.10}$$

where, θ is the equivalent cone angle of the linear phase gradient, k is the wavenumber, and as in Eq. (2.8) $s = (r_0 - r)/w$, r is the radius, r_0, w are respectively the radius and width parameters, a is an exponential truncation parameter, and b a "switch" parameter that can take only two values $b = \pm 1$. As we are going to describe in detail later in this section the addition of the conical gradient enables us to finely control the propagation dynamics of both ring-Airy and inverse ring-Airy beams.

Abruptly auto-focusing beams, often referred as CABs or ring-Airy beams, are a subject of intense research effort [85, 86, 29, 30, 87, 88, 35, 89], since they were first introduced [26, 42]. Their most exciting property is that instead of spreading due to diffraction, they abruptly auto-focus [26, 42], exhibiting a more than two orders of magnitude ratio focal intensity to initial intensity. Likewise, in the non-linear propagation regime [29], these beams

[†]The minus sign in the phase indicates that a positive θ corresponds to a leftwards wavefront tilt, i.e. the tilted wavefront will make a θ angle to the x axis.

preserve their abrupt auto-focusing, with a minimal nonlinear focal shift. This makes them ideal candidates for applications that require controlled energy deposition, with minimal effects before the focus [42]. For example, ring-Airy beams are advantageous compared to Gaussian or Bessel beams in multiphoton polymerization [31] and in two color laser plasma THz generation [30]. Furthermore, a tighter focus, and thus further increase of the focal intensity, can be achieved by using a lens. As it has been recently shown [71], due to the twin wave nature of ring-Airy beams, focusing by a lens leads to two foci instead of one. This counter-intuitive behavior is characteristic for a larger family of waves, referred to as Janus waves [71]. Although this effect is interesting and beneficial to some applications [30], it prevents the use of focusing elements in applications where the twin focus is undesirable. An alternative approach for controlling the focal properties is to use a conical phase gradient. As it has been recently shown [90] for the case of abruptly auto-focusing beams this conical phase acts in a cooperative action with the auto-focusing properties of the beam and provides some additional control to the focus position. In addition, when the focus position is brought close enough to the generation plane, where it becomes comparable to the wavelength, non-paraxial propagation effects appear resulting in a significant increase of their focal intensity contrast, due to the coherent constructive effects of the paraxial and non-paraxial parts of the beam [91].

On the other hand, besides the extensive work in the field, to our knowledge analytical expressions that predict the dimensions and position of the focus for abruptly auto-focusing and auto-defocusing beams are sparse and incomplete. The position of the focus is rather accurately predicted for auto-focusing beams [29, 31] even in the case of the presence of a conical phase

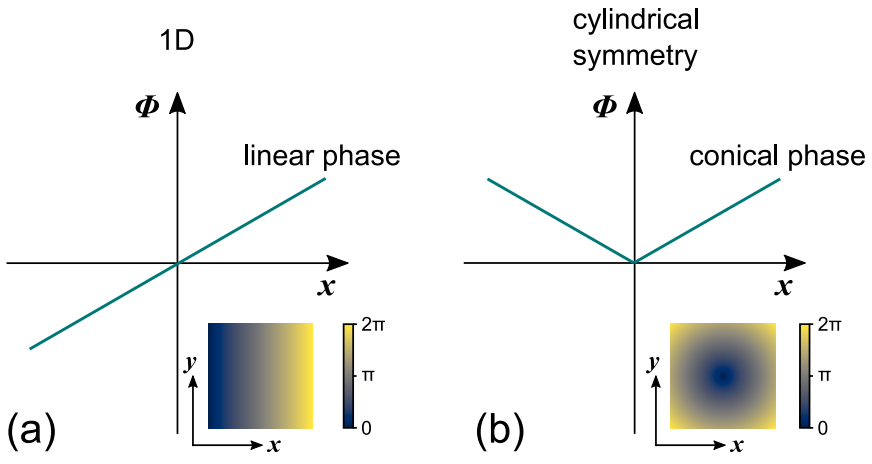

Figure 2.10: Phase gradients. (a) Linear phase, and (b) conical phase. In both cases insets show the corresponding transverse $(x-y)$ phase distribution.

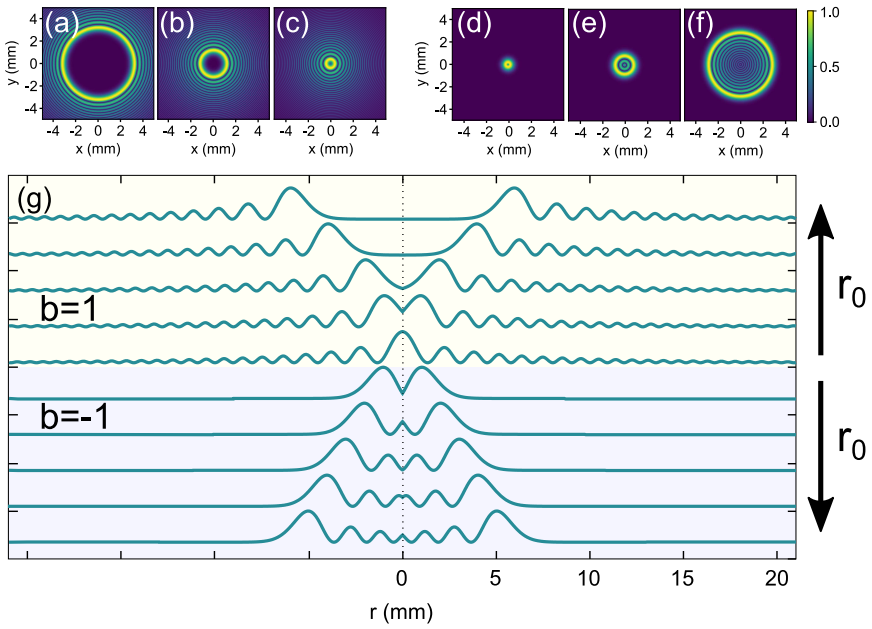

Figure 2.11: Typical amplitude profiles (normalized values) of ring-Airy with $w = 200\mu$m and (a) $r_0 = 3000\mu$m (b) $r_0 = 1000\mu$m (c) $r_0 = 200\mu$m and inverse ring-Airy with $w = 200\mu$m and (d) $r_0 = 400\mu$m (e) $r_0 = 1000\mu$m (f) $r_0 = 3000\mu$m, (g) $I(r, z = 0)$ intensity profiles for rotationally symmetric Airy beams of decreasing radius. $b = 1$ (ring-Airy), $b = -1$ (inverse ring-Airy). Arrows indicate the direction of increasing radius.

gradient [90], but to our knowledge no analytical description exists for their auto-defocusing variant [84]. Furthermore, analytical formulas that predict the focal dimensions [31] are applicable only to abruptly auto-focusing beams for a limited range of beam parameters, and without the presence of a conical phase gradient.

In this work, we follow a unified theoretical analysis for both auto-focusing, and auto-defocusing, ring-Airy beams in the presence of a conical phase gradient. Starting from the analytical expressions that describe the propagation of 1D Airy beams [24], we derive generic analytical expressions that predict the position and dimensions of the focus for both types of beams. Our theoretical predictions are in excellent agreement with numerical simulations, performed over an extended parameters range.

The 1D Airy beams impart their innate properties to ring-Airy beams, their rotationally symmetric variant. As shown in Fig. 2.11(a) the intensity profile of a ring-Airy beam [26] is comprised by concentric rings that become thinner and denser as the radius is increased resembling the characteristic oscillatory shape of the 1D Airy beam, here in cylindrical symmetry. The beam propagation properties are controlled by the dimensions of the primary

ring radius and width [26, 42] but can also be tailored by introducing a tilt though a linear phase gradient [90, 92] which in the case of these rotationally symmetric beams takes the form of a conical phase distribution similar to that of an conical lens (axicon). On the other hand, in the case of the variant of the ring-Airy beam where the secondary rings extend inwards instead of outwards, as shown in Fig. 2.11(b), is an alternative way to define a rotationally symmetric Airy beam. We call this less studied [84, 70] rotationally symmetric Airy beam as inverse ring-Airy.

Airy beam trajectory: From 1D Airy beams to ring-Airy beams

In order to be able to design structured light using a toolbox of template optical beams, one needs to be able to describe their propagation in some kind of analytical form. In the case of 1D Airy beams, a rigorous analytical solution is available [19, 24, 64] and can be directly expanded to 2D Airy [24, 92] and 3D Airy (or Airy^3) beams [76]. This enables us to accurately design structured light using any combination of 1D, 2D or 3D Airy beams. Likewise, another very important member of the accelerating beams family is the cyllindrically symmetric ring-Airy beam. As we have already mentioned, it is not in general possible to directly use a solution derived in the 1D paraxial wave equation in Cartesian coordinates to the cyllidrically symmetric case. The reason behind this is that although the two equations are similar there exists an extra term $\frac{1}{r}u(r,z)$ in the paraxial wave equation in cylindrical coordinates that makes the analogy incomplete:

$$\text{1D Cartesian coordinates}: \frac{\partial^2 u(x,z)}{\partial x^2} + 2ik\frac{\partial u(x,z)}{\partial z} = 0$$
$$\text{Cylindrical symmetry}: \frac{\partial^2 u(r,z)}{\partial r^2} + 2ik\frac{\partial u(r,z)}{\partial z} + \frac{1}{r}\frac{\partial u(r,z)}{\partial r} = 0$$

On the other hand, if we notice more carefully, the extra term $\frac{1}{r}\frac{\partial u(r,z)}{\partial r}$ becomes important near the center $r \to 0$ when $\frac{\partial u(r,z)}{\partial r} \neq 0$. Likewise, the distribution of the ring-Airy beams is such (see Fig. 2.8) that up to their abrupt focus their amplitude near their center is negligible ($u(r,z) \simeq 0 \; \forall \; r < \Delta r$?). This characteristic makes it possible to use the analytic predictions derived for the 1D Airy beam to describe the trajectory of the ring-Airy beam up to the focal point. Furthermore, using this partial analogy we can reach to analytical (although not rigorous) descriptions of all the important beam characteristics that enable us to design structured light that uses combinations of ring-Airy beams.

An ideal 1D model that is analogous to of ring-Airy beams are the symmetric colliding 1D Airy beams [71, 93, 80]. These types of beams are comprised by two symmetric 1D Airy beams propagating along mirrored parabolic trajectories. As they propagate, these beams coherently interfere,

leading to a focus along the propagation axis, a behaviour which is similar to that of the auto-focusing ring-Airy beams. Moreover, for the case of 1D Airy beams there exists rigorous analytic description of the field distribution along propagation [24, 92]. This makes it possible to tailor the focusing behavior of the two symmetric Airy beams and extend these results to their radially symmetric counterpart the ring-Airy beams.

Let's now describe in more detail our reference 1D model that we wish to replicate the behaviour of ring-Airy beams that are further tuned by a conical phase gradient as in Eq. (2.10). The ring structure is replicated by two symmetric 1D Airy beams, while conical gradient is replicated by adding in a symmetric linear phase gradient, or initial tilt angle, to each of the beams. In the initial plane our 1D model is the described as:

$$U_{1D}(x,z;\theta) = \Phi(x,0,\theta) + \Phi(-x,0,-\theta),$$
$$\Phi(x,z,\theta) = Ai(b\frac{x_0+x}{w})\exp(b\alpha\frac{x_0+x}{w})\exp[i(\theta k(x_0+x))]$$

where x, x_0 are respectively the transverse coordinate, and initial displacement, w is the Airy width parameter, θ is the equivalent cone angle ($\sin\theta \sim \theta$), k is the wavenumber, and $\alpha > 0$ is the truncation coefficient. As in Eq. (2.10) the parameter b can take only two values. For $b = 1$ we get the 1D equivalent of the auto-focusing ring-Airy beam, while for $b = -1$ we get the 1D equivalent of the abruptly auto-defocusing inverse ring-Airy beam. Using the rigorous analytic description for the propagation of 1D Airy beams [92] we describe now the field distribution of the symmetric colliding 1D Airy beams at any plane z:

$$\begin{aligned}
U_{1D}(x,z;\theta) =& \Phi(x,z,\theta) + \Phi(-x,z,-\theta),\\
\Phi(x,z,\theta) =& Ai(b\frac{x_0+x}{w} - \frac{z^2}{4k^2w^4} + i\frac{\alpha z}{kw^4} - b\theta\frac{z}{w})\\
&\times \exp(b\alpha\frac{x_0+x-\theta z}{w} - \frac{\alpha z^2}{4k^2w^4})\\
&\times \exp[i(b\frac{x_0+x+b\alpha^2 w}{2kw^3}z - \frac{z^3}{12k^3w^6}\\
&+ \theta k(x_0+x) - b\frac{\theta z^2}{2kw^3} - \frac{\theta^2 kz}{2})]
\end{aligned} \tag{2.11}$$

Clearly, the distribution of the intensity maximum along propagation can be tailored by properly adjusting the initial shift and linear gradient. Our 1D analysis and it's extrapolation to cylindrical symmetry is based on the fact that, up to their focus, ring-Airy beams practically exhibit zero amplitude on their center of symmetry. As shown in Fig. 2.12 numerical simulations confirm that there is a strong analogy between the auto-focusing colliding 1D Airy beams Fig. 2.12(i) and the ring-Airy beams Fig. 2.12(ii). Interestingly, this analogy is also valid for the case of the auto-defocusing colliding 1D

Airy beams Fig. 2.12(iv), and the inverse ring-Airy beams Fig. 2.12(v). Note that besides the position of the focus, the intensity distribution along the propagation axis, especially in the focal region, is almost identical, if we ignore the dynamic range, as shown in Figs. 2.12(iii),(vi). On the other hand, the $I(x, z)$ intensity profiles, as shown in Figs. 2.12(iii),(iv) insets, show some differences especially along x direction, and after the focus. This is an expected result since in one case (colliding 1D Airy beams) we have the interference of two 1D beams carrying a linear phase gradient and in the other (radially symmetric Airy) we have the interference of of a beam modulated with a conical wavefront.

Using the analytic predictions of Eq. (2.11) that refer to the propagation of colliding 1D Airy beams, and taking into account the above-mentioned similarities and differences, we retrieve approximate analytic expressions for the focal properties of radially symmetric Airy beams.

2.3 Focus engineering

Manipulation of a light beam is a crucial component of light applications, particularly the controlled modulation of the initial amplitude and phase distribution that affects its focal region, or as we name it here focus engineering, is more than often a necessity. As we have already discussed in the beginning of this chapter, accelerating beams can be used for a plethora of applications, therefore a rich control of their propagation dynamics is required. For the case of radially symmetric Airy beams an analytical solution of their propagation does not exist, however using the analogy to 1D Airy beams presented in the previous section we can derive semi-empirical analytical equations for the characteristic focal properties. These include, the focal position and focal dimensions longitudinal and transverse size). Let's start from the generic definition of Eq. (2.10) that describes ring-Airy and inverse ring-Airy beams with a conical gradient:

$$u(r, 0) = u_0 \mathrm{Ai}(bs) \exp(b\alpha s) \exp(-i \sin\theta kr)$$

Despite the unified analytical description of Eq. (2.10) for ring-Airy and inverse ring-Airy beams, as shown in Fig. 2.13 their propagation dynamics are quite different. Ring-Airy beams exhibit abrupt auto-focusing. Likewise, their intensity up to the focus is very low, and almost constant as shown in Fig. 2.13(a). On the other hand the inverse ring-Airy beams, when a positive conical phase gradient is added, exhibit abrupt auto-defocusing. Furthermore, as shown in Figs. 2.13(a),(b) we can shift the focus position in a controlled manner for both beams by simply varying the conical phase angle. We have to note here that although the characteristic parabolic trajectory of accelerating ring-Airy beams [26, 42, 71, 31] is shadowed by the presence

of the strong linear gradient, the abrupt auto-focusing behavior is clearly evident in the profiles of the peak intensity along z.

In [31] approximate analytic relations were recently introduced for the estimation of abruptly auto-focusing ring-Airy focal parameters f_{Ai}, Δf_{Ai}, w_{Ai} as a function of the radius r_0 and width w parameters of the initial main ring of the ring-Airy, however valid only for $r_0/w \gg 1$. Using the equivalence to 1D+1 colliding Airy beams, we extended this analysis to radially symmetric Airy beam, to cover abruptly auto-focusing and auto-defocusing ring-Airy beams, under the action of a conical phase gradient at the ini-

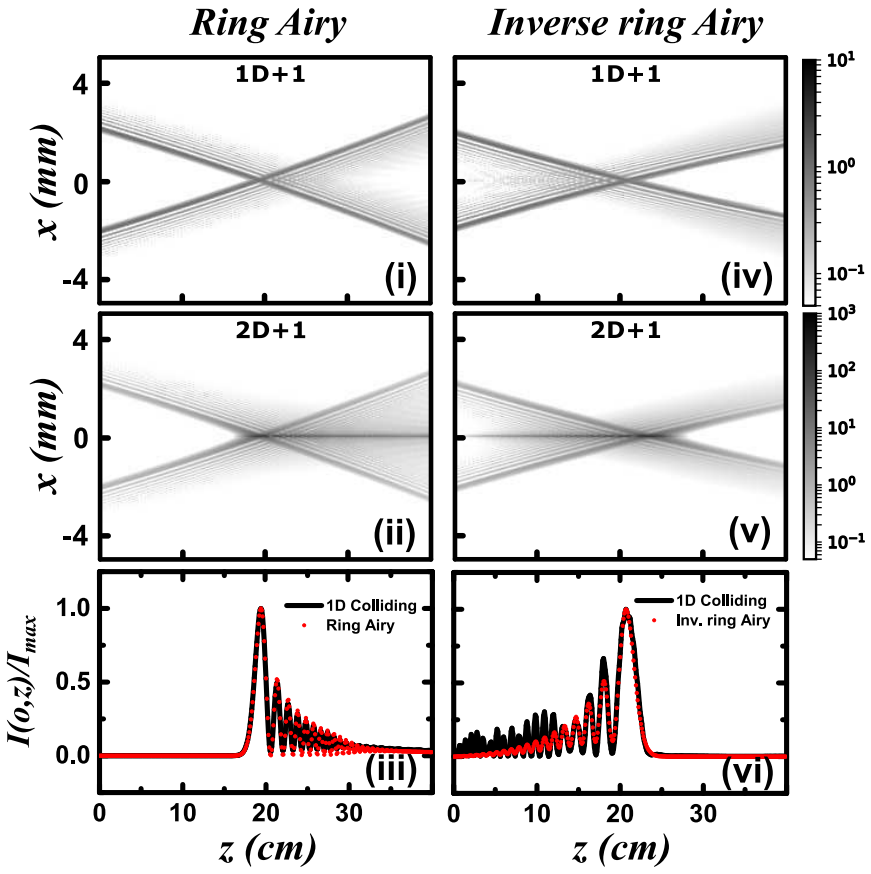

Figure 2.12: Comparison of intensity $I(x, z)$ along propagation for auto-focusing colliding 1D Airy beams (1^{st} row) with with radially symmetric Airy beams (2^{nd} row). 3^d row: Normalized intensities along the z propagation axis $I(0, z)/I_{max}$. Insets: $I(x, z)$ intensity profiles (normalized, false colors), (1D) colliding 1D Airy beams (2D) radially symmetric Airy beams. (Numerical simulation parameters: λ=0.8 μm, $\alpha = 0.05$ (i) $x_0 = -2.0$ mm, w=100 μm, θ=10 mrad (ii) r_0=2.0 mm, w=100 μm, θ=10 mrad (iv) x_0=2.0 mm, w=100 μm, θ=10 mrad (v) r_0=2.0 mm, w=100 μm, θ=10 mrad).

tial plane. Furthermore, our unified analytical description now include an expanded initial parameters range.

Controlling the focus position

The focus position can be accurately predicted by our 1D reference model. When the the truncation coefficient is sufficiently small ($\alpha \ll 1$) it is possible

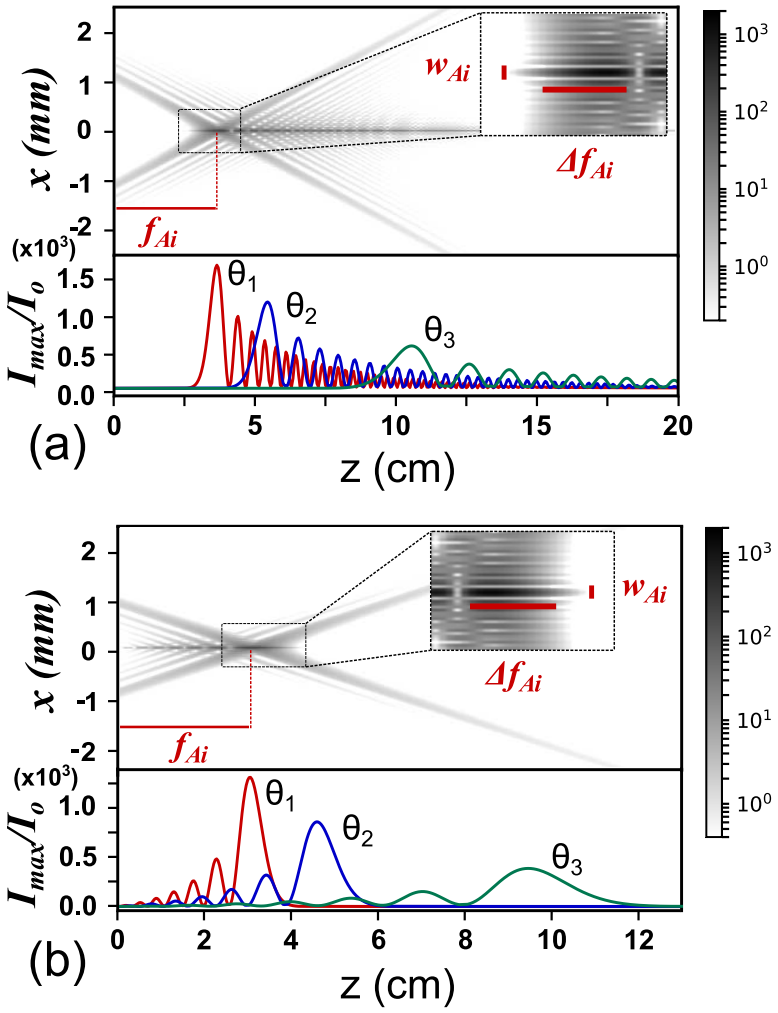

Figure 2.13: Intensity $I(x, z)$ profiles of rotationally symmetric Airy beams and peak intensity along z with different conical phase gradients at the input plane (z=0) $\theta_{i=1,2,3}$=30 mrad, 20 mrad, 10 mrad (r_0=1.0 mm and w=100 μm, u_0=1) (a) ring-Airy (b) inverse ring-Airy. Insets show the position and the dimensions of the focus.

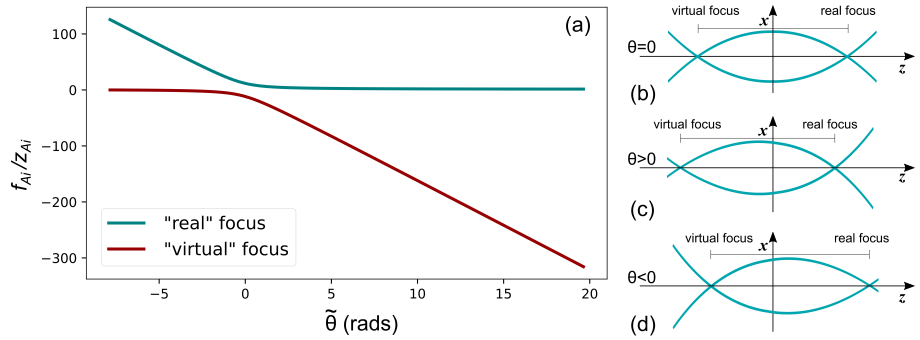

Figure 2.14: Ring-Airy double foci. (a) Position of the real and the virtual foci of ring-Airy beams as a function of normalized angle $\tilde{\theta}$. (b)-(d) Graphical representation of the peak intensity features parabolic trajectory for $\theta = 0, \theta > 0$ and $\theta < 0$ respectively.

to analytically describe the position of the focus:

$$f_{Ai}^{1D} \cong 4bz_{Ai}\left[-2\tilde{\theta} \pm (4\tilde{\theta}^2 + b\tilde{x})^{1/2}\right] \tag{2.12}$$

where $z_{Ai} \equiv kw^2/2$, $\tilde{x} \equiv x_0/w + b$ is a shape factor and $\tilde{\theta} \equiv z_{Ai}\theta/w$ is a normalized cone angle. Two solutions (note the $\pm$ sign) appear in Eq. (2.12)]. These are a result of the Janus nature of these waves [71], and correspond to the foci of the "real" and "virtual" waves. As shown by Fig. 2.14 (a) the position of the "real" focus of the ring-Airy decreases monotonically and abruptly with normalized angle $\tilde{\theta}$, meanwhile "virtual focus" goes further from the initial plane in the negative regime as the normalized angle $\tilde{\theta}$ increases. This behavior is depicted in Fig 2.14(b)-(c) where the trajectories of the primary ring of these beams, for the three cases of the conical angle, are illustrated. By exploiting the relation of the 1D model for the trajectory of the main lobe we translate this into the trajectory of the primary ring of the cylindrical symmetric Airy beams. Thus we can extract an analytic equation for the focus position of the abruptly autofocusing ring-Airy and abruptly auto-defocusing inverse ring-Airy beam shaped by a conical phase:

$$\frac{f_{Ai}}{z_{Ai}} \cong 4b\left[-2\tilde{\theta} \pm (4\tilde{\theta}^2 + bs)^{1/2}\right] \tag{2.13}$$

where $z_{Ai} \equiv kw^2/2$, $s \equiv r_o/w + b$ is a shape factor and $\tilde{\theta} \equiv z_{Ai}\theta/w$ is a normalized cone angle.

A graphical representation of the trajectories of ring-Airy and inverse ring-Airy with conical phase gradient is presented in Fig. 2.15. For negative values of the conical angle θ, the focus of the ring-Airy is formed in a greater distance from the generation plane, while its peak intensity decreases, and after a limit value of θ is disappeared, whereas although the peak intensity

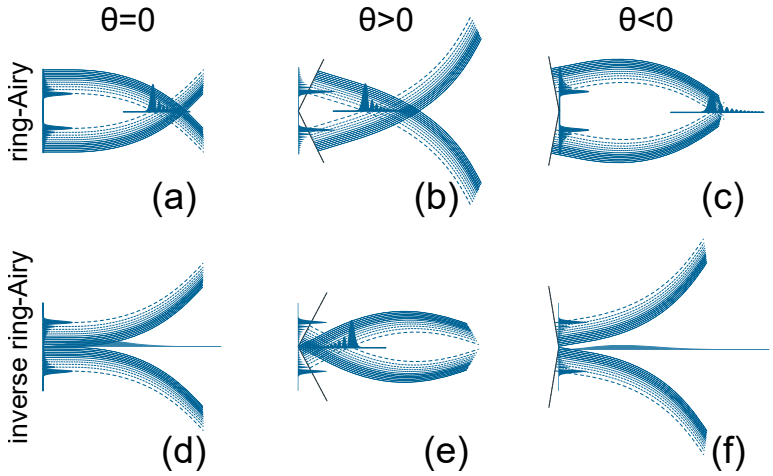

Figure 2.15: Illustration of the trajectory control in the presence of conical phase gradient for (a)-(c) a ring-Airy beam and (d)-(f) an inverse ring-Airy beam .

of the inverse ring-Airy deceases it maintains a similar behavior, forming an elongated focus. Contrary, when the conical angle θ takes positive values, the focus of the ring-Airy is brought closer to the initial plane $z = 0$ while its peak intensity contrast increases, in addition, interestingly, the inverse ring-Airy after a positive limit value of θ forms a focus that abruptly auto-defocuses. furthermore the intensity distribution of the peak intensity along propagation of the inverse ring-Airy, when it forms a focus, is like a mirror image of the of the ring-Airy, this can be seen in Fig. 2.13.

Focal length

The next important focal parameter is the longitudinal dimension of the focus, namely the the focal spot length Δf_{Ai}. Taking into account the trajectory of the 1D toy model of Eq. (2.12), we can estimate the projection of the primary lobe on the axis at the focus, this is illustrated in Fig. 2.16, where the projection is indicated by the red line. Using this approach we reach to an approximate analytic description for the focal spot length:

$$\frac{\Delta f_{Ai}}{f_{Ai}} \cong \frac{42b-1}{50}\left[\left(4\tilde{\theta}^2+bs\right)-2\tilde{\theta}\left(4\tilde{\theta}^2+bs\right)^{1/2}\right]^{-1} \tag{2.14}$$

Focus Width

To derive an analytic description for the transverse dimension of the focus, namely the focal spot width w_{Ai} is a more complicated task. The radially

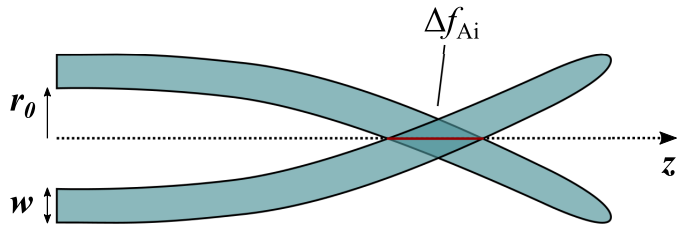

Figure 2.16: Illustration of the derivation of the focal length of ring-Airy beams using the projection of the primary lobe on the axis at the focus.

symmetric nature of the problem enables us to locally approximate the focal spot as a result of the interference of a conically shaped wavefront as shown in Fig. 2.17. Using this approach makes it possible to use the well-known analytic estimations for the spot size of Bessel beams [13]. In order to estimate the incoming wavefront cone angle at the focus we use the tangent of the analytically described from the 1D reference model parabolic trajectory Eq. (2.12). Thus, we reach to an approximate analytic estimation of the focal spot width for ring-Airy and inverse ring-Airy beams:

$$\frac{w_{Ai}}{w} \cong C\left(1-\frac{1}{2-2b\tilde{\theta}^2+bs}\right)\left(\frac{4}{4\tilde{\theta}^2+bs}+\frac{w^2}{z_{Ai}^2}\right)^{1/2} \tag{2.15}$$

where $C \equiv (76+22b)/(65+15b)$ is a constant.

2.3.1 Engineering abruptly auto-focusing ring-Airy beams

To confirm the validity of our analytic predictions as described in Eqs. (2.12) - (2.15) we used numerical simulations of the paraxial wave equation [10], for a broad range of parameters of the initial ring of CABs. More specifically, we quantitatively studied the evolution of the focal properties f_{Ai}/z_{Ai}, $\Delta f_{Ai}/f_{Ai}$, w_{Ai}/w as a function of two parameters; the normalized shape factor s and the normalized conical angle $\tilde{\theta}$. In our numerical simulations we either vary the normalized shape factor s keeping a constant normalized conical angle $\tilde{\theta}=0$ or we vary $\tilde{\theta}$ keeping s constant. In the first case, since $\tilde{\theta}=0$, our results are comparable to the estimations presented in [31]. We have to

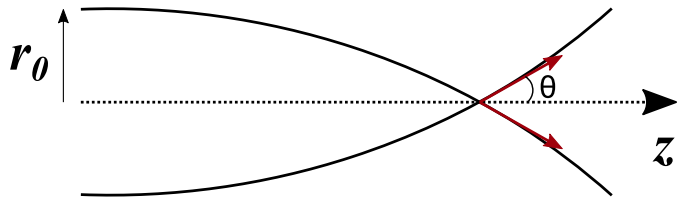

Figure 2.17: Illustration of the derivation of the focal width of ring-Airy beams using the approach of the interference of a conically shaped wavefront.

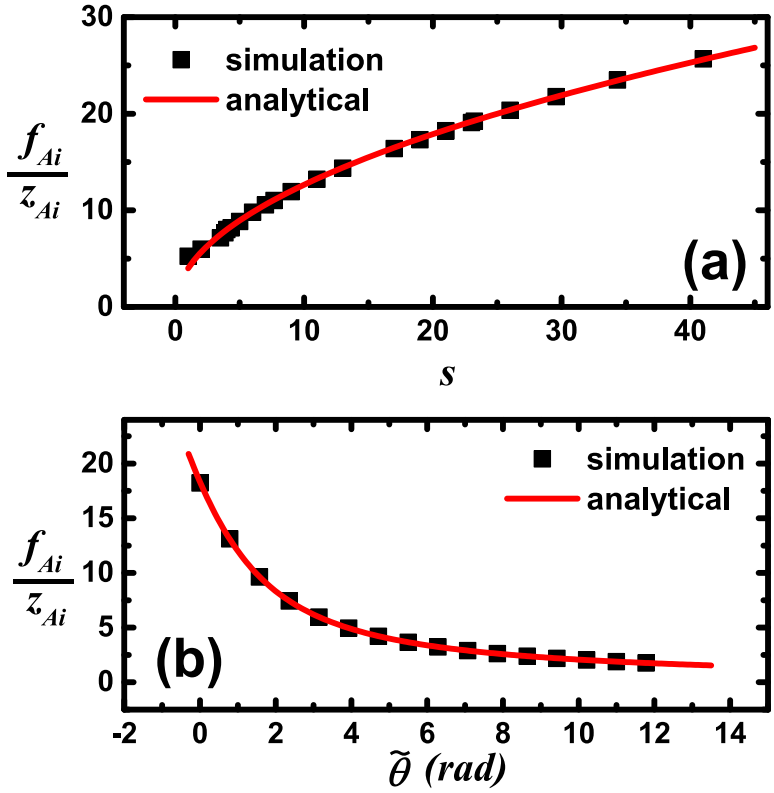

Figure 2.18: Focal distance f_{Ai}, of abruptly auto-focusing ring-Airy beams normalized over z_{Ai} as a function, (a) of the shape factor s ($\tilde{\theta} = 0$), (b) of the normalized cone angle $\tilde{\theta}$ (s=21).

note though that Eqs. (2.12) - (2.15) are now valid for a much larger initial parameters ranging from $r_0/w > 1$, $\tilde{\theta} > 0$ up to $r_0/w \approx 40$, $\tilde{\theta} \approx 15$ rad. Fig. 2.18(a) shows the position of the focus f_{Ai} as a function of the primary ring parameters. The numerical simulations are in both cases in excellent agreement with the theoretical predictions of Eq. (2.12). As the shape factor s is increased, the normalized focal distance is increased proportionally to $\sqrt{s}$ as predicted by Eq. (2.12) for $\tilde{\theta} = 0$. We should note here that increasing the shape factor s by decreasing the ring width w parameter also affects the normalized length z_{Ai}. Likewise, Fig. 2.18(b) depicts the effect of the conical phase angle on the focus position. As expected, increasing the conical angle $\tilde{\theta}$ decreases the normalized focal distance f_{Ai}/z_{Ai}. Clearly, by varying the conical angle $\tilde{\theta}$, instead of the shape factor s, we achieve a similar dynamic range in controlling the focus position, although f_{Ai} saturates for $\tilde{\theta}$ >6 rad.

Fig. 2.19 shows the focal spot length Δf_{Ai} as a function of the primary ring parameters. Again the numerical simulation results are in very good agreement to the analytical predictions of Eq. (2.14). As the shape factor s is increased the normalized focal spot length is decreased. Combining this

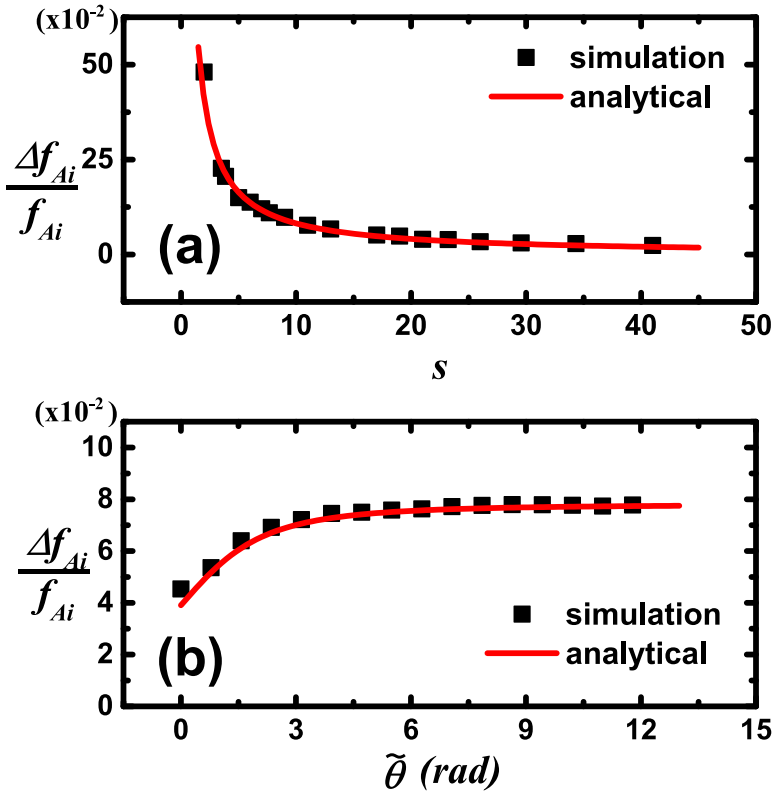

Figure 2.19: Ring-Airy focal spot length normalized over the focal distance f_{Ai} as a function (a) of the shape factor s ($\tilde{\theta} = 0$), (b) of normalized cone angle $\tilde{\theta}$ (s=21).

with the fact that the focal distance f_{Ai} is increased, as shown in Fig. 2.18(a), we get that as the focus is shifted further away it becomes shorter compared to the focal distance f_{Ai}. On the other hand, as shown in Fig. 2.19(b), when the conical angle is increased the the normalized focal length quickly saturates after $\tilde{\theta} > 3$ rad. Likewise, Fig. 2.20 shows the dependence of the focal spot width w_{Ai}, normalized over the width parameter w as function of the initial parameters. The analytical predictions of Eq. (2.15) are in very good agreement with the numerical simulation results. As the shape factor s is increased, the normalized focus width monotonically decreases. A similar behavior is observed in Fig. 2.20(b), where the cone angle $\tilde{\theta}$ is increased.

Another crucial characteristic of the beam's focal region is its shape, which is well described by it's aspect ratio, defined as the ratio of the focal length over the focal width $AR_{rAi} = \Delta f_{Ai}/w_{Ai}$. Fig. 2.21 depicts the analytically estimated values of the aspect ratio AR for auto-focusing ring-Airy beams as a function of the radius r_0 and width w parameters. The results in Fig. 2.21(a) are retrieved for a conical angle $\theta = 0$ while in Fig. 2.21(b)

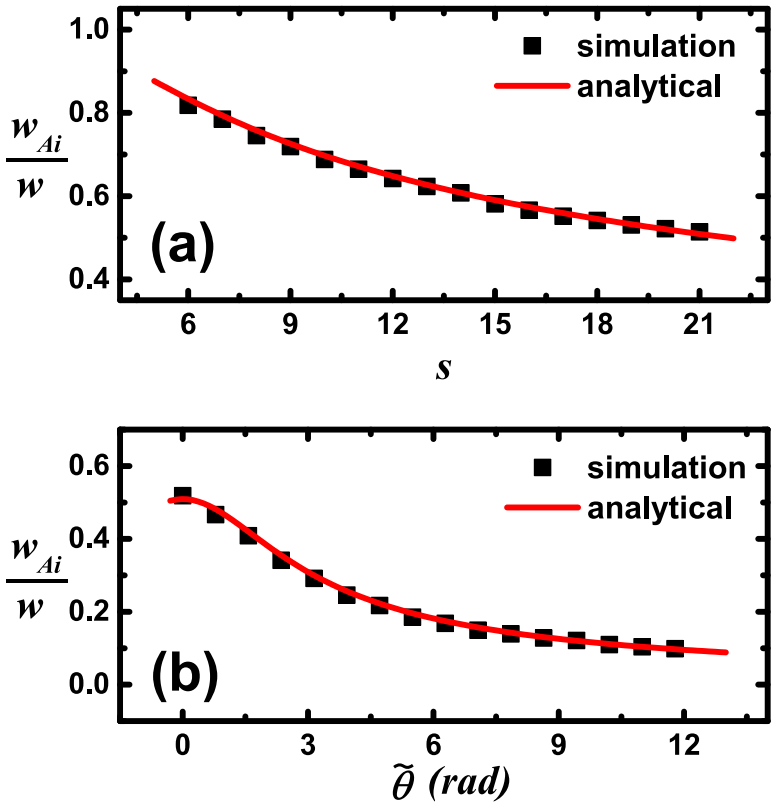

Figure 2.20: Focal spot width w_{Ai} of ring-Airy, normalized over the width parameter w as a function (a) of the shape factor s ($\tilde{\theta} = 0$) and (b) of the normalized cone angle $\tilde{\theta}$ (s=21).

for a conical angle θ=5 mrad. From the contour lines we can observe that a constant aspect ratio, i.e. a preservation of the focus shape, can be achieved

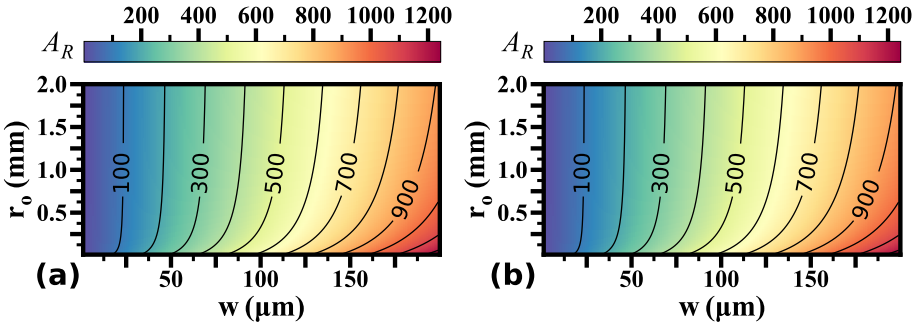

Figure 2.21: Aspect ratio $\Delta f_{Ai}/w$ of the focal region of a ring-Airy as a function of the radius and width parameters (r_0, w). (a) $\theta = 0$, (b) $\theta =$ 5 mrad.

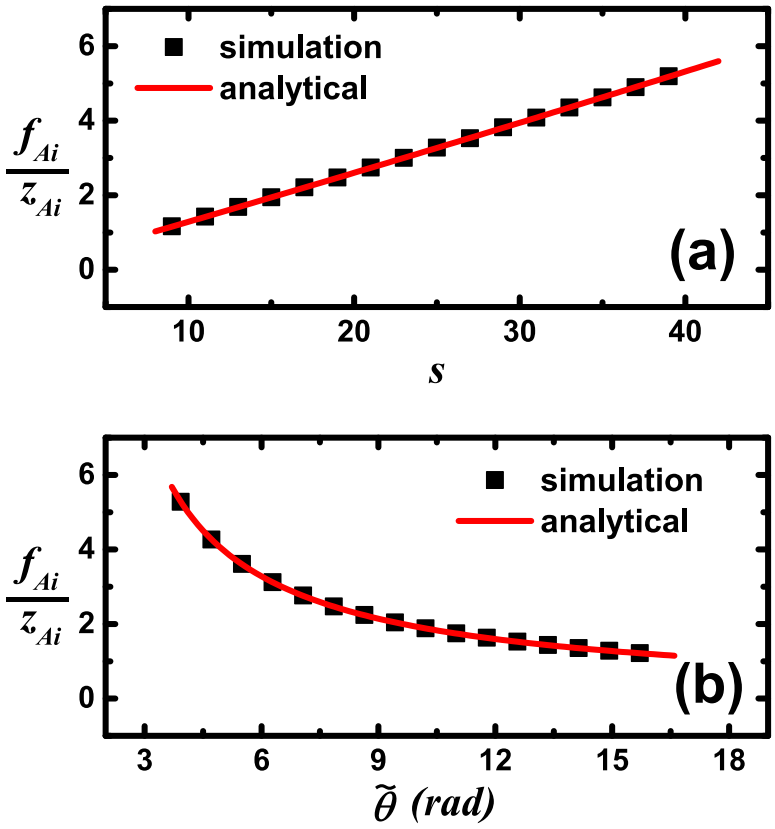

Figure 2.22: Position of the focus f_{Ai} of an auto-defocusing inverse ring-Airy beam, normalized over z_{Ai}. (a) as a function of the shape factor s ($\tilde{\theta} = 7.854$ rad), (b) as a function of the normalized cone angle $\tilde{\theta}$ (s=19).

by controlling the shape parameter through the radius parameter r_0 while keeping the width parameter w constant. This interesting behavior was first demonstrated by [31] for the case of $\theta = 0$. Here we expand this result for the case of a conical angle $\theta > 0$. As it can be seen from Fig. 2.21 a typical characteristic of these beams is the needle-like shape of the focal region since the aspect ratio is quite high ($AR_{rAi} > 100$). This characteristic, from the practical point of view, and in respect of the shape of the focal region, sets auto-focusing ring-Airy beams between Bessel beams [13] where the aspect ratio is much higher and typical Gaussian beams where the aspect ratio can be quite lower.

2.3.2 Engineering abruptly auto-defocusing inverse ring-Airy beams

Inverse ring-Airy beams reveal their abrupt auto-defocusing behavior in the presence of a conical phase gradient. This phase gradient is represented by

conical angle θ in Eq. (2.10). As shown in Fig. 2.13(b) in order for the abrupt auto-defocusing behavior to be observed the conical angle have to be greater than a limit value:

$$\widetilde{\theta} > (s/4)^{1/2}$$

As in the case of auto-focusing ring-Airy beams, to confirm the validity of our analysis we performed numerical simulations of the paraxial wave equation [10]. Our simulations were preformed for a broad range of values of the main ring radius, width, and conical angle with the condition that the beam exhibits abrupt auto-defocus.

Fig. 2.22(a) shows the position of the focus f_{Ai} of an auto-defocusing inverse ring-Airy beam as a function of the scale parameter s. The simulations are performed for a conical angle $\theta = 10$ mrad ($\tilde{\theta} = 7.854$ rad). Numerical simulations are in excellent agreement with the theoretical predictions of Eq. (2.12), showing that the normalized focus position exhibits a practically linear dependence on the shape parameter s as expected. Indeed

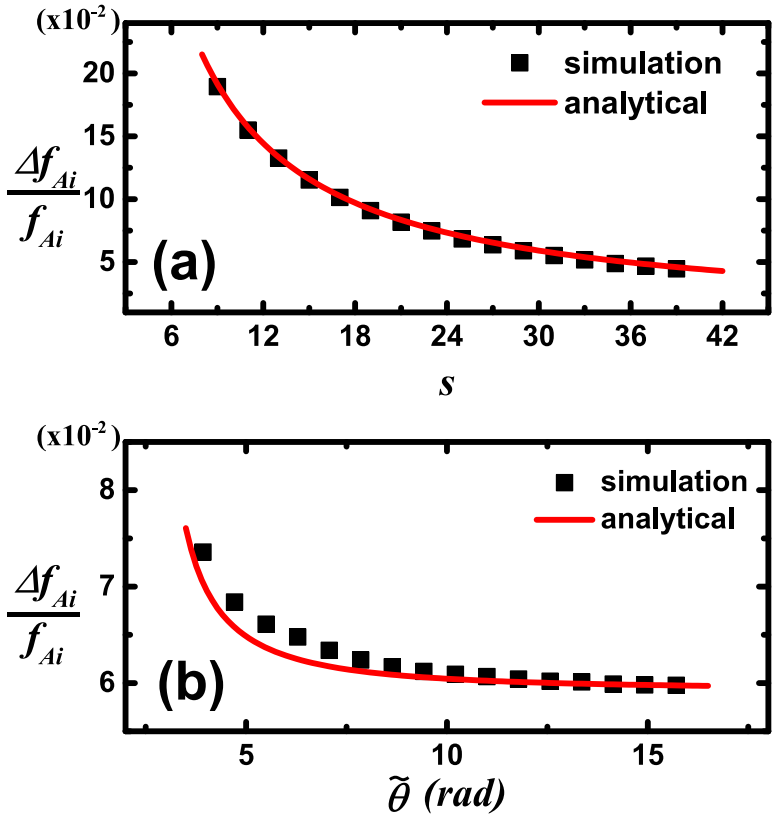

Figure 2.23: Inverse ring-Airy focal spot length Δf_{Ai} normalized over f_{Ai} as a function (a) of the shape factor s ($\tilde{\theta}$ =7.854 rad). (b) of the normalized cone angle $\tilde{\theta}$ (s=29).

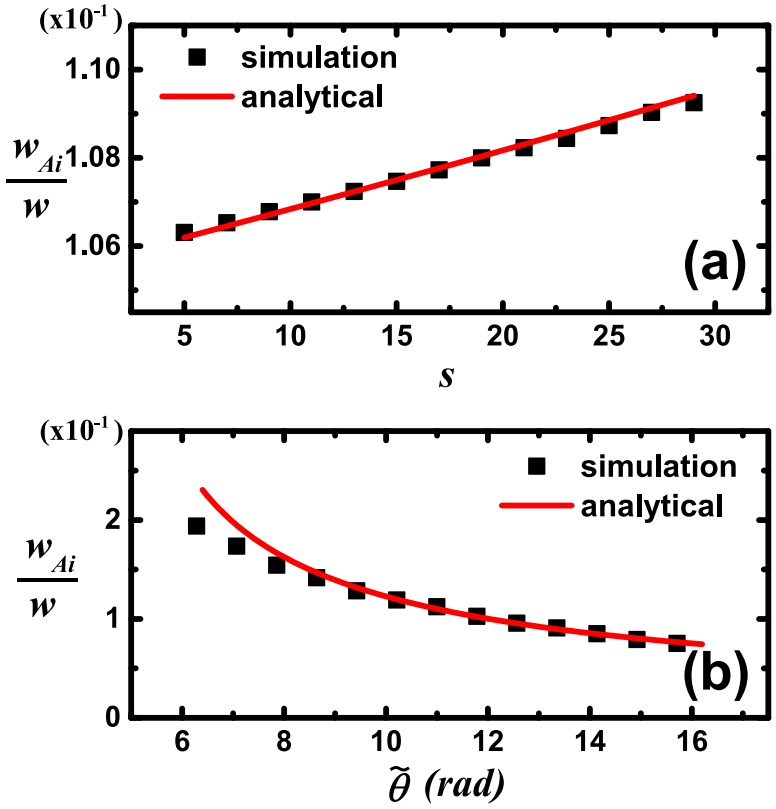

Figure 2.24: Focus width w_{Ai} of an abruptly auto-defocusing inverse ring-Airy, normalized over the width parameter w as a function (a) of the shape factor s ($\tilde{\theta}$ =10.21 rad). (b) of the normalized cone angle $\tilde{\theta}$ (s=19).

from Eq. (2.12) and by setting $b = -1$ we get $f_{Ai}/z_{Ai} \cong s/\tilde{\theta}$ for $s \ll 4\tilde{\theta}^2$. Likewise, Fig. 2.22(b) shows the effect of the conical phase gradient on the focus position of the abruptly auto-defocusing ring-Airy. Again, the numerical simulations are in excellent agreement with the predictions of Eq. (2.12). The normalized focus position shows a monotonic decrease as the conical angle is increased, in a similar fashion as in the case of the abruptly auto-focusing ring-Airy beams shown in Fig. 2.18. Furthermore Fig. 2.23(a) depicts the dependence length of the focus (FWHM) Δf_{Ai} of an auto-defocusing inverse ring-Airy beam normalized to the focus position as a function of the scale parameter s. The numerical simulation results are in excellent agreement with the analytical predictions of Eq. (2.14). Similar to the case of the ring-Airy beams shown in Fig. 2.19(a) the normalized focal length shows a monotonic decrease as the s parameter increases. On the other hand, as shown in Fig. 2.23(b), although there is a very good agreement between the numerical simulations and the analytical predictions for $\tilde{\theta} > 7$ rad, the Eq.(2.14) underestimates $\Delta f_{Ai}/f_{Ai}$ by $< 5\%$ when $\tilde{\theta} < 6$ rad. This is due

to the fact that for low values of the cone angle $\tilde{\theta}$ we are approaching the validity limit of our analysis which in holds for $4\tilde{\theta}^2 > s$.

Fig. 2.24(a) depicts the focal width w_{Ai} of an auto-defocusing inverse ring-Airy beam, normalized over the width parameter w, as a function of the shape parameter s. The analytic predictions are again in excellent agreement to the numerical simulations. Although the normalized focal width w_{Ai} exhibits a linear dependence on the shape parameter s, this holds only for if the width parameter w remains constant, as we can deduce from Eq. (2.15) for the case of $s \ll 4\tilde{\theta}^2$. The dependence of w_{Ai}/w on the conical phase angle $\tilde{\theta}$ is shown in Fig. 2.24(b). While the fit between analytical predictions and numerical simulation results is excellent for $\tilde{\theta}$ >8 rad, Eq. (2.15) overestimates by 10% for $\tilde{\theta}$ <7 rad. As in the case of Δf_{Ai} for such low $\tilde{\theta}$ values we approach validity limit of our analysis.

The aspect ratio AR_{rAi} of auto-defocusing inverse ring-Airy beams as a function of the radius r_0 and width parameters w is shown in Fig. 2.25. The results in Fig. 2.25(a) are for a conical angle $\theta = 10$ mrad while in Fig. 2.25(b) for $\theta = 15$ mrad. In both cases the valid AR_{rAi} values are between $r_0 > w$ and $r_0/w < 2(1 + \tilde{\theta}^2)$ as shown by the respective curves. The contour lines mark the areas of constant aspect ratio. As in the case of abruptly auto-focusing ring-Airy beams AR_{rAi}, and thus the focal voxel shape, is preserved when the radius parameter r_0 is increased while keeping the width parameter w constant. Likewise, the aspect ratio takes large values ($AR_{rAi} > 100$), indicating a needle-like focal region.

2.3.3 Light scalpels using superimposing CABs

As we have shown in the previous sections, the use of accelerating beams can be quite advantageous for engineering the focal characteristics. We can tailor the focus by varying a small number of parameters. Even more exciting possibilities arise when we superimpose such fields to generate exotic

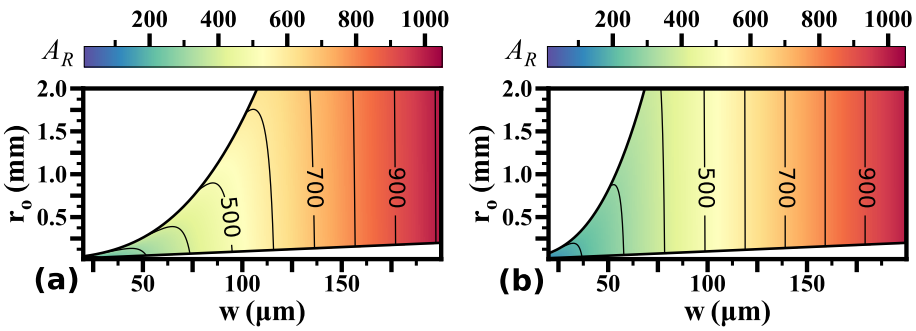

Figure 2.25: Aspect ratio $\Delta f_{Ai}/w$ of the focal region of an inverse ring-Airy as a function of the radius and width parameters (r_0, w). (a) θ =10 mrad, (b) $\theta = 15$ mrad.

focal distributions. In the following we will discuss about some of these superpositions and their unique characteristics.

Engineering Multiple foci

Creating two foci along the propagation axis of a beam, although can be of great use in various applications, is not a trivial task. For example, holographic methods can be used [94] to produce multiple foci in 3D space, but they suffer from interference artifacts they are located along the propagation axis. We take advantage of the unique properties of accelerate beams to generate tailored foci along the propagation axis. Our approach is based on superimposing two ring-Airy beams (autofocusing and autodefocusing) which share a common conical phase modulation like that of an axicon. As a result, two distinct foci are created along propagation.Each focus is independently controlled both in terms of the relative position and relative peak intensity. The field amplitude on the initial plane is then described by:

$$u(r,0) = u_0[C \cdot Ai(s)\exp(as) + Ai(-s)\exp(-as)]\exp(-i\sin\theta kr) \quad (2.16)$$

where C is a parameter which takes values in the range $C \in (0,1]$ and is used to.control the intensity ration between the foci.

In order to study the properties of such a superposition we have performed numerical simulations of the paraxial wave equation [10] in all of our simulations we have set the wavelength $\lambda = 0.8\mu m$, and used a truncation factor $\alpha = 0.05$, while the the parameter C was tune to adjust the intensity contrast between the two foci.

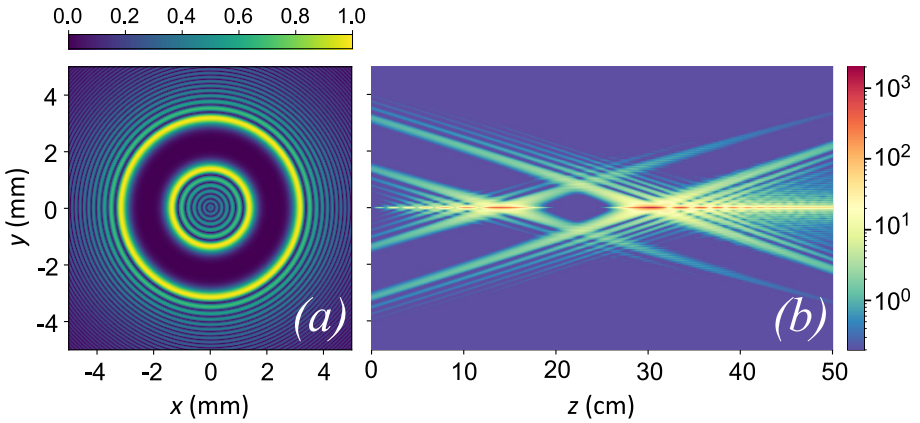

Figure 2.26: Typical (a) transverse amplitude profile at the initial plane ($|A(x,y,z=0)|$) of the combination of a ring-Airy and an inverse ring-Airy at z=0 and (b) its corresponding $y-z$ cross-section intensity distribution along propagation.

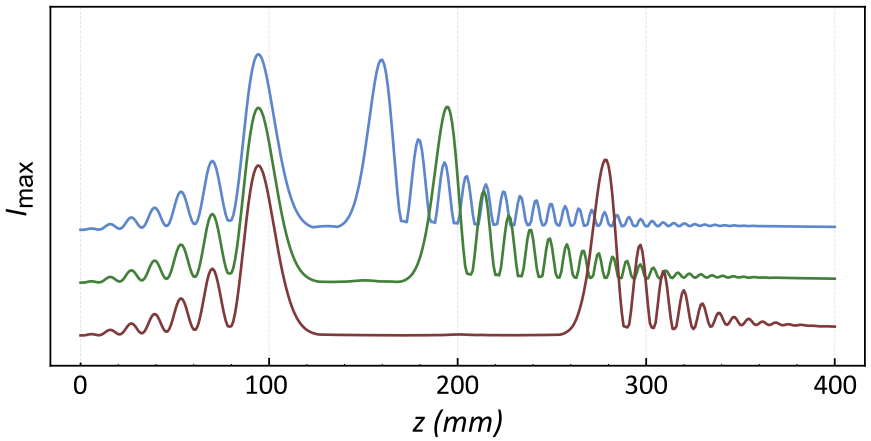

Figure 2.27: Intensity distribution along z of three different cases of shaped accelerating beams controlling the relative position of the double foci. (I_{max} lines are shifted for better illustration.)

A typical example of this superposition and the resulting double foci feature is depicted in Fig. 2.26. As shown in Fig. 2.26(a), which depicts the amplitude of the two beams at the initial plane $z = 0$, we chose the ring parameters r_0, and w in such a way so that the whole inverse ring-Airy is contained within the area that is surrounded by the primary ring of the ring-Airy. The reasoning behind this design strategy is that within this area the ring-Airy amplitude is practically zero, thus we avoid any unnecessary complexity in the initial plane distribution. As we can see in Fig. 2.26(b), the inverse ring-Airy is set to focus first. Likewise, after this abrupt autodefocus, the abrupt autofocus of the ring-Airy is formed. We should note here that although the strong linear conical phase gradient shadows the parabolic trajectory of the beams, the accelerating properties are apparent in the abrupt focal intensity variation.

The control of the position of the two separate foci can be easily achieved in our approach by properly tuning the primary ring parameters r_0, w, and the cone angle θ. Such a control is shown in Fig. 2.27 which depicts the peak intensity $I_{max}(z)$ along propagation for a superposition of an ring-Airy and inverse ring-Airy beam as we move one of the two foci along the axis. To

Table 2.1: **Parameters of CABs in Fig. 2.27.**

Beam	r_0 (μm)	w (μm)	θ $(mrad)$	C
Ring-Airy	1600	100	10	0.65
	2000	100	10	0.6
	3000	100	10	0.52
Inverse ring-Airy	1000	100	10	-

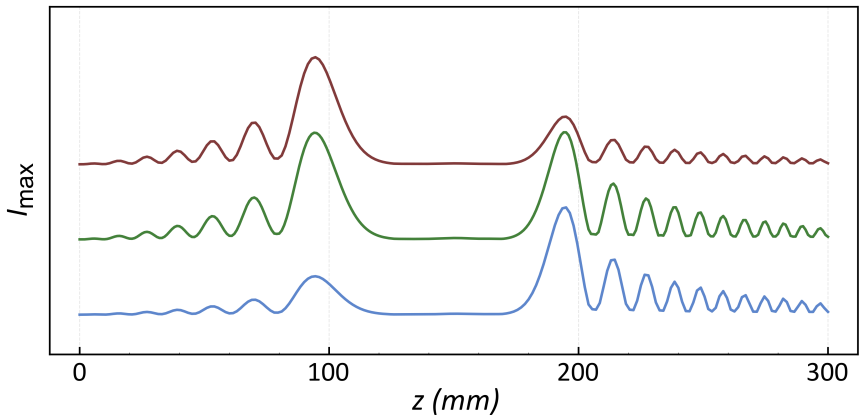

Figure 2.28: Maximum peak intensity distribution along z of three different cases of shaped accelerating beams controlling the relative intensity of the double foci.(I_{max} lines are shifted for better illustration.)

achieve this we properly select the parameters r_0, w, and C (see Table 2.1.) of the ring-Airy beam while keeping the cone angle θ constant. As we can clearly observe from Fig. 2.27 the 2nd foci can be moved back and forth on the propagation axis, with no effect on the 1st focus or their relative intensities. Alternatively, the position of the two foci can be controlled by tuning the primary ring radius r_0 of one of the beams while keeping the width parameter w, and the cone angle θ constant. In this case a proper calibration of parameter C is still required in order to adjust relative intensities. Moreover, we are also able to adjust the relative intensities of the two foci. This is shown in Fig. 2.28 which depicts numerical simulation results of the peak intensity $I_{max}(z)$ along propagation for a superposition of an ring-Airy and inverse ring-Airy beam as we tune their relative intensities. In our simulations we simply finely tune the parameter C, which controls the ring-Airy focus intensity, while keeping the primary ring parameters r_0, w and the angle θ constant (see Tab. 2.2). Note that in this case only the peak intensity of the second focus is affected with practically no effect on the position or distribution of the two foci.

Another exceptional result of the superposition of accelerating beams generating multiple foci along the propagation is that it is advantageous compared to other methods when the beam encounters obstacles. Notably,

Table 2.2: **Parameters of CABs in Fig. 2.28.**

Beam	r_0 (μm)	w (μm)	θ ($mrad$)	C
Ring-Airy	1700	100	10	0.4, 0.63, 0.8
Inverse ring-Airy	1000	100	10	-

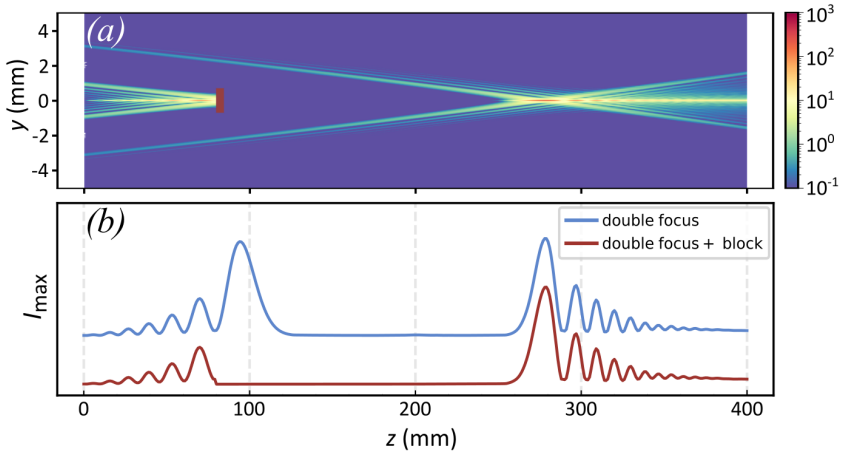

Figure 2.29: Double foci feature with the first foci blocked by an obstacle. (a) Intensity cross-section along propagation $I(y, z)$ and (b) normalized peak intensity along propagation. (I_{max} lines are separated for better illustration.)

our generation scheme is resilient in the presence of an obstacle due to their decoupled trajectories, a property imparted from the Airy distribution. To demonstrate this property we have performed numerical simulations of the paraxial wave equation in the presence of an obstacle that entirely blocks the first of the two foci. As it is clearly shown in Fig. 2.29, although the first focus is blocked the second focus remains intact. This occurs because both foci are formed by interference effects from light that is directed towards the focus though a combination of a strong linear and non-linear phase gradient. We believe that this remarkable characteristic could find great use in many applications, for example in materials processing especially when a simultaneous treatment of a two sided object, like a glass plate, is required. In the previous examples the foci are located a few hundreds of mm away from the source. This is a rather large working distance for many applications, so an obvious question is if we can scale all this down. Recently, it was demonstrated that ring-Airy beams can be scaled down to the paraxial limit [91], with the working distance reducing to mm or even μm. On the other hand, it is straightforward to scale-up to working distances of several meters by using optical components, such as beam expanders. As we are going to show in the following, by properly selecting the parameters that control the focal characteristics of a CAB, we can adjust its focal dimensions, and therefore the focal distance down to the sub-millimeter regime. To demonstrate this flexibility we have performed numerical simulations where, by tuning the beam's parameters we have scaled the focal range over 4 orders of magnitude, i.e. from meters to hundreds of micrometers. For example, Fig. 2.30 shows the peak intensity $I_{max}(z)$ over the propagation distance for three cases of

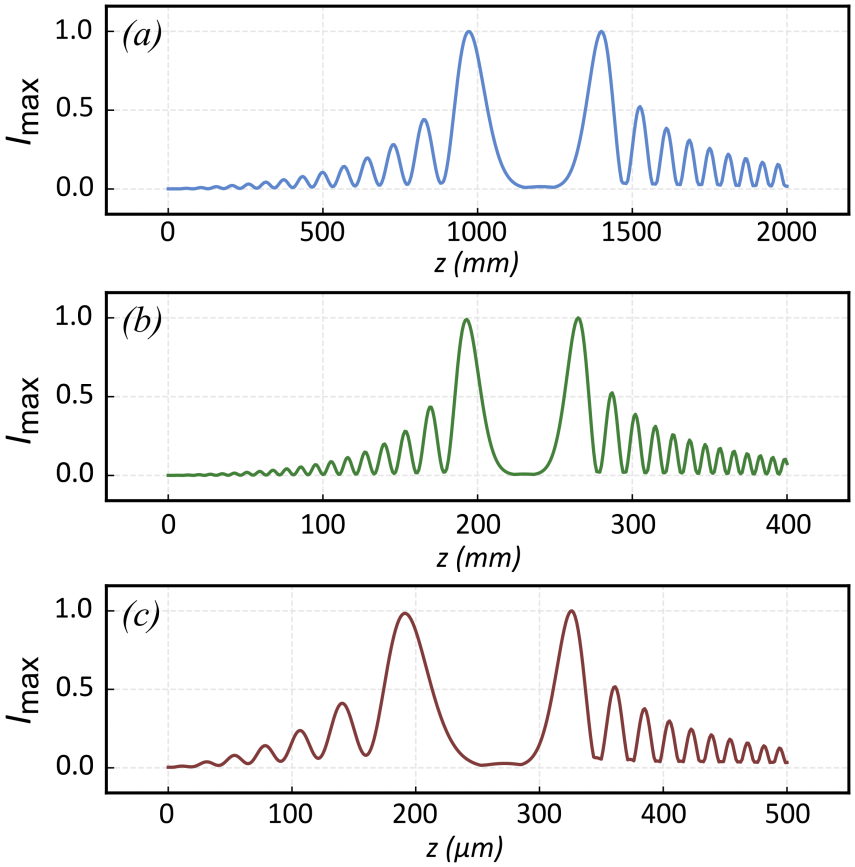

Figure 2.30: Normalized peak intensity distribution along z of three different cases of scaled double foci features produced from ring-Airy and inverse ring-Airy with conical phase gradient.

superimposed ring-Airy and inverse ring-Airy. In all cases a conical phase gradient is used to enhance and control the focus position (see Table 2.3 for the the parameters used in each case). With this we want to show the capa-

Table 2.3: **Parameters of CABs in Fig. 2.30.**

Beam	r_0 (μm)	w (μm)	θ $(mrad)$	C
Ring-Airy	7000	300	5	0.75
	1300	50	50	0.82
	70	4	200	0.59
Inverse ring-Airy	5000	300	5	-
	1000	50	50	-
	40	4	200	-

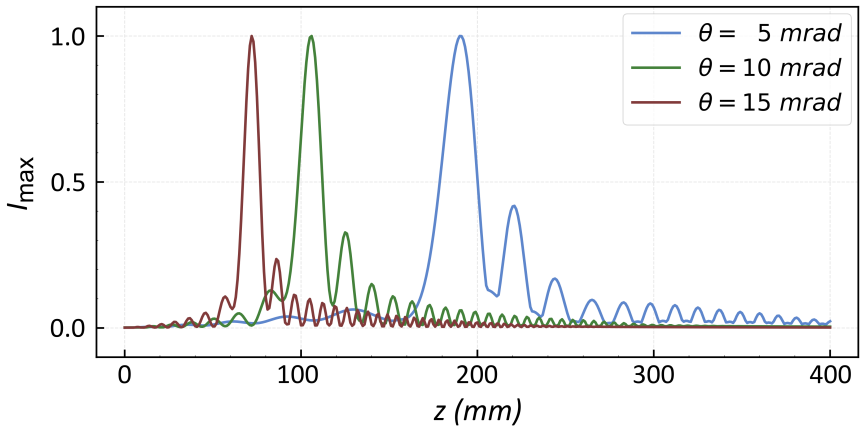

Figure 2.31: Normalized peak intensity distribution along z of ring-Airy and inverse ring-Airy beams with CPG focusing at the same position forming a hyper-focus.

bility of these shaped beams to be utilised in various applications of different scales.

Hyper-focus

As we have shown, the position of the two foci can be finely tuned. Let's study now the case where the two foci are tuned so that they overlap. This superposition of abruptly auto-focusing with an abruptly auto-defocusing beam leads to an intense focus, of high peak intensity contrast focus which we refer to as hyper-focus. The location of this hyper-focus can be estimated from the analytical description of the focus position f_{Ai} as a function of r_0, w, and θ:

$$r_0' \simeq b(\frac{f_{Ai}}{4z_{Ai}})^2 w + f_{Ai}\theta - bw \tag{2.17}$$

where f_{Ai} is the focus position of the CAB, and $z_{Ai} = \pi w^2/\lambda$. By properly tuning the parameters we are able to focus both ring-Airy and inverse ring-Airy beams at the same position along propagation axis. For example, we can select the parameters w, and θ to be the same for both beams. Then by using the value of radius r_0 for the one beam as a parameter, we can solve for the the radius r_0' from Eq. (2.17) under the condition that the two foci overlap. This interesting behaviour can be seen in Fig. 2.31, where numerical simulations results of the peak intensity $I_{max}(z)$ for three different cases are shown (see Table 2.4 for the parameters used). As we can observe from the three distinct cases that are depicted the hyper-focus is fully controllable. We can tune the parameters of the primary ring of both beams in order to adjust the focal characteristics, namely the width, the

length and the position of the hyper-focus. Fuerthermore, this hyper-focus combines the characteristic features of both beams to abruptly auto-focus and auto-defocus. Interestingly as a result of the interference of two beams, their secondary intensity features are suppressed, resulting in a focus with even higher intensity contrast reaching values that of $I_{max}/I_0 \sim 800$.

Twisting light: Tornado Waves

As we described in (1.2.4), we can induce topological charge into e light beam by imprinting a helical phase into it. Such structuring produce optical vortices, where their phase distribution is rotating along propagation as a result of OAM. Moreover, the intensity profile of such beams exhibit a doughnut-like shape due to destructive interference along axis ($I(x = 0, y = 0, z) = 0$). Such beams find application in various fields ranging from optical trapping [95] to communications [96].

Moreover, the interference of two beams carrying OAM of opposite topological charge have been shown to produce a rotating intensity pattern along propagation. Particularly, it has been observed that the superposition of higher-order Bessel beams produce rotating intensity patterns with constant angular velocity [97, 98]. In addition, as shown in [99, 100] through the superposition of complex beams imposed with OAM, the creation of angularly accelerating intensity patterns is possible.

We refer to structured light in which its characteristic intensity features rotate along propagation as twisting light. In particular, here we examine the case of the recently introduced tornado waves [101], where two or more ring-Airy beams modulated by opposite vortices, produce high intensity lobes, accelerating both radially and angularly along propagation.

In a more recent publication, Brimis et. al [101] showed that it is possible to create light that accelerates both in the radial and angular directions, along propagation, called tornado waves. This has been achieved utilizing the inherent property of a ring-Airy to auto-focus in accelerating fashion. Thus, by superimposing two abruptly auto-focusing ring-Airy beams carrying OAM of opposite topological charges and focusing in overlapping regions in space along propagation, a pattern of high intensity lobes that approaching to each other and rotating in an accelerating manner, is created. The initial field

Table 2.4: **Parameters of CABs in Fig. 2.31.**

Beam	r_0 (μm)	w (μm)	θ $(mrad)$	C
Ring-Airy	1000	100	5, 10, 15	1
Inverse ring-Airy	905.6	100	5	-
	1109.8	100	10	-
	1158.1	100	15	-

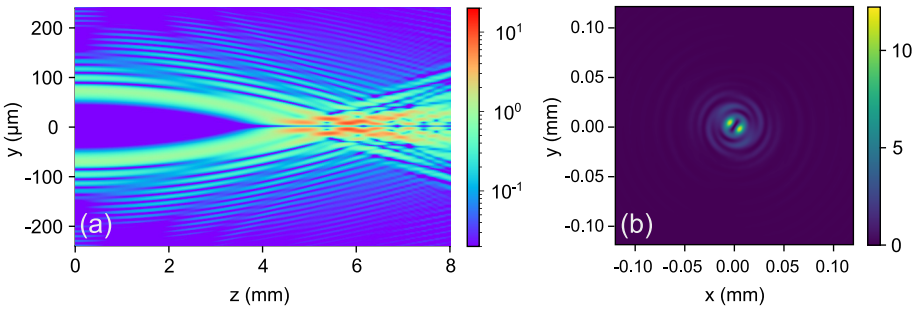

Figure 2.32: (a) Propagation of intensity and (b) transverse intensity profile at distance $z = 5.9$ mm of Tornado waves TWs consisting of two ring Airy beams carrying OAM with parameters: $r_{01} = 62.5$ μm, $r_{02} = 62.5$ μm, $w_1 = 12.5$ μm, $w_2 = 11.25$ μm, $\alpha = 0.03$, $m_1 = 1$, $m_2 = -1$, and $\lambda = 0.8$ μm.

distribution of the superposition of the two ring-Airy beams carrying OAM is given by:

$$u(r, \phi, z = 0) = \mathrm{Ai}(s_1) \exp(\alpha s_1) \exp(i m_1 \phi) + \mathrm{Ai}(s_2) \exp(\alpha s_2) \exp(i m_2 \phi) \tag{2.18}$$

where, Ai denotes the Airy function, $(r,\ \phi,\ z)$ describe the cylindrical coordinates, $s_i = (r_{0i} - r)/w_i$, r_0, w are the radius and the width parameters of the main ring of the ring-Airy, respectively, and m_i denotes the topological charge of the helical phase imposed in each ring-Airy beam. The behavior of TWs along propagation is shown in Fig 2.32 where it shows the $I(y, z)$ intensity distribution Fig 2.32(a) and the transverse intensity profile $I(x, y)$ at a distance $z = 5.9$ mm Fig 2.32(b) of TWs consisting of two ring Airy beams carrying OAM with parameters: $r_{01} = 62.5$ μm, $r_{02} = 62.5$ μm, $w_1 = 12.5$ μm, $w_2 = 11.25$ μm, $\alpha = 0.03$, $m_1 = 1$, $m_2 = -1$, and $\lambda = 0.8$ μm. This behavior resembles a double helix that shrinks as it propagates and is visualized in Fig. 2.33 where the spiraling trajectory of the high-intensity lobes of the tornado waves consisting of two vortex ring-Airy beams with opposite helicities ($m_1 = 1$, $m_2 = -1$) is depicted.

Furthermore it is possible to form a multiple lobe intensity feature, when the ring-Airy beams carry OAM of opposite helicities $m_i > 1$, then the number of intensity lobes N is given by the sum of the absolute values of the topological charges $N = |m_1| + |m_2|$ of each helical phase.

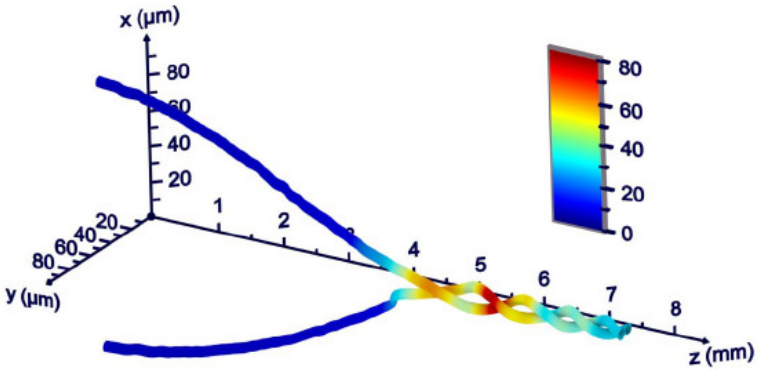

Figure 2.33: Visualization of the spiraling trajectory of the high-intensity lobes of the tornado waves consisting of two vortex ring-Airy beams with opposite helicities ($m_1 = 1$, $m_2 = -1$). The figure is edited from [101], with permission for the authors.

3 | Generation techniques of structured light

3.1 Generation techniques

For the generation of structured light a device, or an optical element, that shapes the wavefront, the amplitude or the polarization of a beam is required. Although light structuring sounds somehow exotic, it is a common practice that often becomes unnoticed. A simple example of such an optical element that performs such structuring is the spherical lens. In this case, a quadratic phase modulation is imposed by the lens to an incoming wavefront [102]. For example, when a collimated beam travels through a converging lens, it's plane wavefront is converted to spherical leading it to focus on the focal plane of a lens. Such a transformation is an example of light structuring through a continuous phase modulation device. Likewise, there are numerous optical elements or devices that shape light in a continuous fashion, ranging form simple reflective optical elements like spherical mirrors to a more complex adaptive optics device such as a deformable mirror [103]. In more detail, adaptive optics is a large category of optical systems that its main goal is to correct the distortions/aberrations of a wavefront by measuring those distortions and calculating the required corrections [104, 105]. Afterwards using a device that shapes the distorted wavefront imposes those corrections. Such a device usually is a deformable mirror that can change its overall shape in a controlled way so that it can compensate for the wavefront distortions. A schematic of a deformable mirror correcting a distorted wavefront is presented in Fig. 3.1, where the incoming distorted wavefront is corrected by the deformable mirror and then reflected.

On the other hand, there are also devices that structure light in a discrete manner. In this case, the phase or the amplitude of a wavefront is modulated using an array of discrete and independently controllable modulation points. Such devices are often referred to as spatial light modulators (SLMs). They can be either transmissive or reflective and can modulate the amplitude (amplitude SLMs) or the phase (phase SLMs). In the case of phase SLMs the device modulates the phase from $0 \rightarrow 2\pi$ so phase wrapping is used to

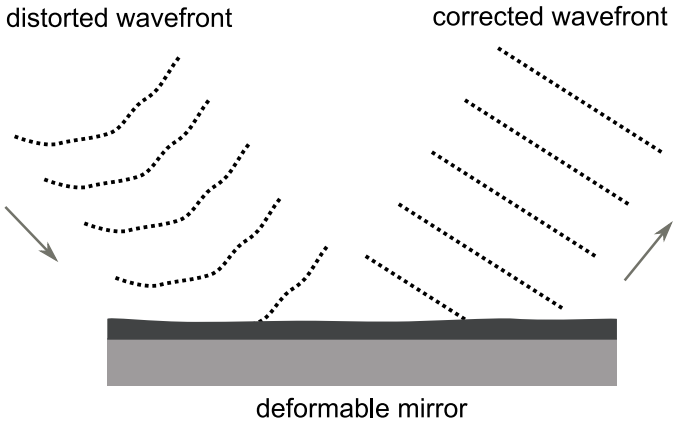

Figure 3.1: Schematic representation of a deformable mirror correcting a distorted wavefront.

cover modulations larger that 2π. Their operation is based either on liquid crystal arrays [17, 106], or on digital micro-mirrors. Digital micro-mirror devices(DMDs), are optomechanical devices that use a large number of independently moving reflective mirrors, each sized a few microns, to modulate the wavefront [107, 108]. Such devices usually used in two positions, selectively deflecting parts of the beam, so they are ideal amplitude modulators for reflective binary Computer Generated Hologram (CGH) applications.

In this work we applied both continuous and discrete methods for the generation of structured light. We developed a reflective phase modulation device consisting of cylindrical mirrors that can operate as a broadband continuous phase mask. We used this device for the generation ultra-broadband white light 2D Airy beams as well for the study of the effect of the spatial coherence upon such beams. On the other hand, we utilized a spatial light modulator (SLM) for the generation of complex structured accelerating beam carrying orbital angular momentum (OAM), called Tornado Waves (ToWs).

3.1.1 Continuous methods

As we mentioned before light structuring methods can be divided in two categories, first the continuous methods, in which the incoming light beam is shaped in a continuous manner, and discrete methods where the wave is shaped independently in small regions. Using the latter method usually there is diffraction to discretization and thus the efficiency is not the optimum, on top of that in most cases there is also the need for phase wrapping, this has a negative effect on the final quality of the structured light. These limitations can be solved using a continuous method to structure light. Such a method make use of devices utilizing components with a smooth surface. Such components can be simple optical elements such as lenses or mirrors, a

deformable mirror, or even a custom made continuous phase mask made of a transparent material. In this thesis we use the first approach, in a nutshell, we exploit the aberrations of cylindrical mirrors to create a continuous phase modulation device.

3.2 Continuous phase modulation using optical aberrations

As we have already described in the previous section, continuous modulation of a wave's properties can be realized with a variety of methods. In the case of phase modulation for example we commonly use spherical lenses and mirrors for this purpose. A direct use of such elements results in a quadratic phase modulation. For a more complex wavefront transformation the standard solution is to use either continuous phase masks or adaptive optics. Here we present a different approach that uses optical aberrations of simple cylindrical reflective optics to modulate the phase of an incoming wavefront

3.2.1 Ultra-broadband and ultra-intense structured light

Optical aberrations

In order to understand the idea behind this counterintuitive approach, let's first describe the nature of optical aberrations. An ideal optical system, images each point from the object space to a single point in the image space. In real optical systems this behaviour, referred to a *Stigmatic imaging*, is possible within the paraxial optics regime [2]. So optical aberrations describe the deviation of an optical system's performance from the ideal stigmatic imaging. Optical aberrations can be quantified in two ways as depicted in Fig. 3.2. The first refers to the ray aberration and is a vector with a starting point on the paraxial image plane and an ending point on the point where the light ray intersects the paraxial image plane [2]. The second is referred to as wavefront aberration and is based on comparing the wavefront that exits from the exit pupil of the optical system to a spherical wavefront that is centered on the paraxial image point.

Therefore, the wavefront exiting form a system where optical aberrations are present, differs form the ideal spherical one since optical aberrations lead to deformations. This deteriorating action of optical aberrations leading to undesired effects on the final result, is the reason behind all this effort to minimize or eliminate them [110, 111, 112]. Although starting from simple geometrical optics principles, analytic formulations of optical aberrations are increasingly complex even for simple optical systems [111, 112]. The absence of a generic solution, and complexity of the problem, drives optical designers to acquire the necessary skills though continuous practice and education

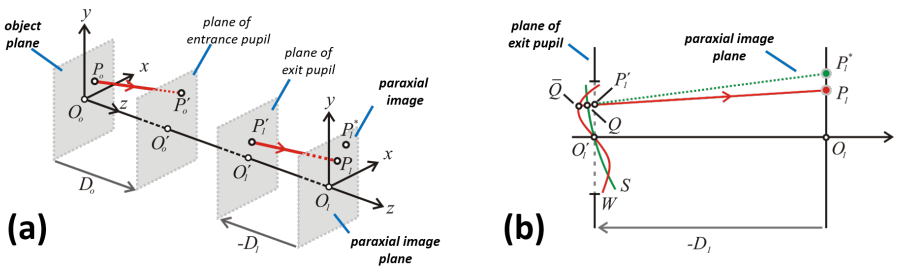

Figure 3.2: Optical Aberrations. (a) Ray aberration is defined as $\bar{\delta} = \overline{P_1^* P_1}$ (b) Wavefront aberration defined as $\Phi = (\bar{Q}Q)_{OPL}$. Figure from [109]

[110, 111].

For example, the wave aberration Φ of an optical system can described [2] as a Taylor series:

$$\Phi = \Phi^{(0)} + \Phi^{(4)} + \ldots + \Phi^{(2\kappa)} + \ldots$$

where $\Phi^{(0)}$ refers to the paraxial regime, $\Phi^{(4)}$ are the Seidel aberration terms, and orders higher than this are referred to as higher order aberrations. Seidel aberration terms can be analytically described for a simple spherical lens

$$\Phi^{(4)} = -\frac{1}{4}B\rho^4 - \frac{1}{2}(2C\cos^2\theta + D)\, r_0^2\rho^2 + E\, r_0^3\rho\cos\theta + F r_0\rho^3\cos\theta \quad (3.1)$$

where B, C, D, E, F are respectively the spherical aberration, astigmatism, field curvature, distortion and coma aberration coefficients, θ is the azimuthal angle at the exit pupil, r_0 is the object height and ρ is the distance, measured from the optical system center, along the normal to the propagation axis. Fig. 3.3(a)-(e) depicts an illustration of primary Seidel illustration.

By closer observation of Eq. (3.1) it becomes clear that the Seidel terms, or the primary aberrations, represent smooth perturbations of an ideal wavefront so we can envisage their action as the action of continuous phase masks. Nevertheless, the term $\cos\theta$ in astigmatism and distortion aberrations lead to a coupling between the Cartesian coordinates x, y, thus we cannot independently control the phase modulation in those axes. A simple solution is to this problem is the use of 1D cylindrical system, which they impose phase modulation only onto their optical axis, thus by cascading two such system orthogonally oriented to each other we can achieve an independent modulation.

In the case of an one dimensional (1D) cylindrical optical system, Eq. (3.1) is simplified to [2, 25]:

$$\phi_{1\mathrm{D}}^{(4)} = -\frac{1}{4}Bx^4 + Fx_0x^3 - \frac{1}{2}(2C + D)\, x_0^2x^2 + E\, x_0^3x, \quad (3.2)$$

where x_0 is the object height and x is the distance, measured from the optical system center, along the normal to the propagation axis. As it is

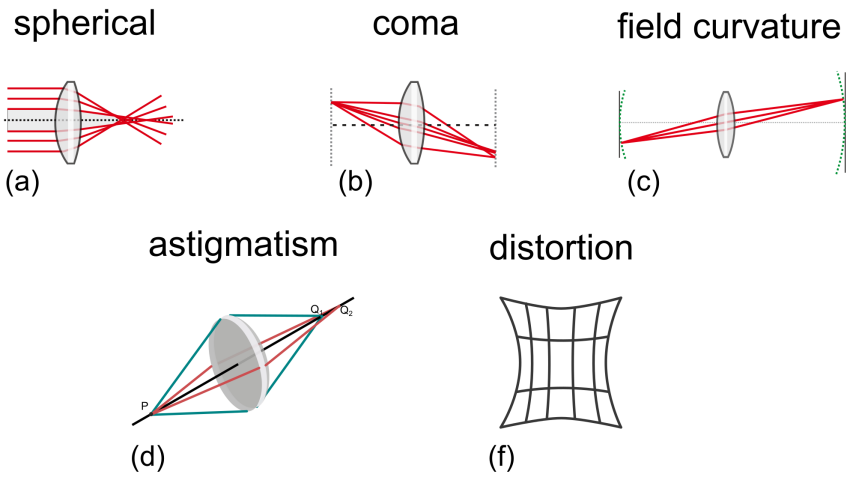

Figure 3.3: Primary Seidel aberrations. (a) Spherical aberration, (b) Coma, (c) Field curvature, (d) Astigmatism, (e) Distortion.

evident in Eq. (3.2) the wavefront primary aberrations are now described as a power series over x while the cross-mixing effect of the azimuth angle θ is eliminated. For example, spherical aberration leads to a pure quartic spatial phase perturbation while coma aberration leads to a pure cubic one.

A initial implementation of the idea of using optical aberrations as continuous phase masks was first demonstrated in [25]. In this early work, the coma aberration of a tilted cylindrical refracting telescope system was isolated to achieve a pure cubic phase modulation. In this thesis, this initial idea was expanded to allow for high-power, ultra-broadband, and tunable phase masks that rely on optical aberrations. As we will demonstrate, reflective cylindrical optics can be properly adjusted so that the resulting optical aberrations can used as polynomial spatial phase modulation devices. In more detail, a simple reflective beam expander can be tuned to isolate polynomial phase terms up to the forth power. Furthermore, these polynomial terms can be combined, by properly tuning the optical system, to lead to non trivial phase distributions. Interestingly, although spectrally ultra-broadband, the simplicity of the design enables the scaling of the system for operation in any part of the electromagnetic (E/M) spectrum.

1D beam expander as a tunable phase mask

Although in a single element optical system the aberrations can not be isolated [110, 25, 113], nevertheless this is possible, as we will show, in an optical system consisting by two elements. As it is well known in optical design, the optical aberrations can be minimized by using consecutive optical elements with aberration coefficients of opposite sign [110, 2, 112]. We use the same

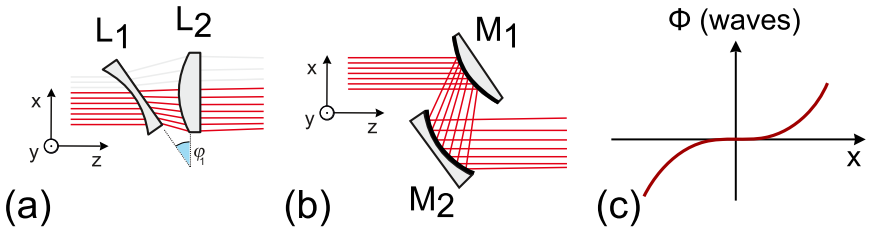

Figure 3.4: Beam expander consisting of (a) two cylindrical lenses L_1 and L_2 as in [25] and (b) two cylindrical mirrors as in [114]. In (c) the corresponding isolated coma aberration which a 3rd order phase is plotted.

basic principle to independently control each of the aberrations in a two element system. The cylindrical beam expander [25] is an ideal template optical system, since it converts a plane wavefront in the entrance to a plane wavefront at the exit. Optical aberrations are in this case introduced by applying small variations in the orientation and the position of the optical elements.

In Fig. 3.4(a), a simple beam telescopic beam expander consisting of cylindrical lenses L_1, L_2 is illustrated as presented in [25], the orientation of the lenses, in space, is such as to isolate the 3rd order coma aberration Eq. (3.2). Although, this device has its advantages as it is continuous there also some limitations to it. First it has limited bandwidth due to dispersion of the lenses as well as limited power threshold because of the absorption fro the lenses. Moreover, with this configuration of the lenses the effective area, where the wavefront has acquired the desired cubic modulation, is only the bottom half as indicated by the red lines in Fig. 3.4(a). An extension of this scheme that tries to overcome these limitations was developed in this thesis, and uses cylindrical mirrors instead of lenses as illustrated in Fig. 3.4(b). When a collimated beam passes through the telescopic expander acquires a cubic phase modulation in the direction of the optical axis, here x direction, as shown in Fig. 3.4(c). Using mirrors the phase modulation through OPD is achieved with propagation in air so the dispersion is minimized, also there is the possibility to use our device in vacuum to avoid the dispersion completely. In addition the effective area in the case of mirrors is limited only by the aperture of the first mirror. Furthermore, using reflective optics expands the power threshold such a device can withstand.

Let's now focus on the design of a simple beam expander composed by two cylindrical mirrors. As shown in Fig. 3.5, in our design light is first reflected from the convex diverging cylindrical mirror M_1, and then by the concave converging M_2. The diverging element placed first in order to allow for the system to withstand the highest input power possible. Since the beam diverges after reflection by mirror M_1, it's intensity will be reduced when it is reflected by mirror M_2, so the highest intensity is expected in the

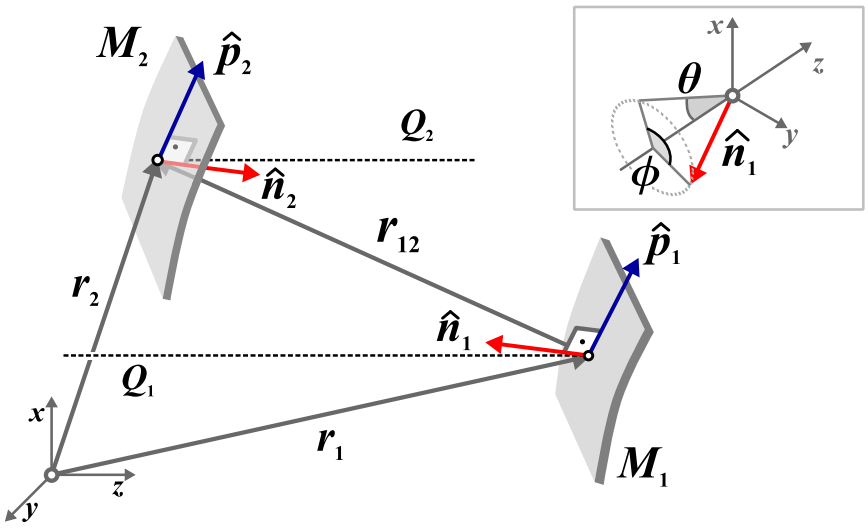

Figure 3.5: Cylindrical mirror beam expander. The mirror position is denoted by vectors $\boldsymbol{r}_i$, while unit vectors $\hat{\boldsymbol{n}}_i$, $\hat{\boldsymbol{p}}_i$ describe respectively the mirror orientation and direction of curvature at its center. The optical axis in the entrance and exit of the system is denoted by Q_i. $(i = 1, 2)$. Inset: Orientation of M_1, detail showing the polar θ and azimuthal ϕ angles of rotation.

input mirror which sets the threshold. If the beam was first reflected by a converging mirror then the intensity would increase inside the system thus setting a lower input threshold. Without loss of generality, we consider that $\boldsymbol{r_1} = \bar{\boldsymbol{0}} \Rightarrow \boldsymbol{r}_2 = \boldsymbol{r}_{12}$, thus the orientation and the position of the mirrors so that the system behaves as a beam expander is described by:

$$\begin{aligned}
\hat{\boldsymbol{n}}_1 =& \cos\phi \sin\theta\ \hat{\mathbf{x}} + \sin\phi \sin\theta\ \hat{\mathbf{y}} - \cos\theta\ \hat{\mathbf{z}}, \\
\hat{\boldsymbol{n}}_2 =& -\cos\phi' \sin\theta'\ \hat{\mathbf{x}} - \sin\phi' \sin\theta'\ \hat{\mathbf{y}} + \cos\theta'\ \hat{\mathbf{z}}, \\
\boldsymbol{r}_{12} =& d\ (\cos\phi \sin 2\theta\ \hat{\mathbf{x}} + \sin\phi \sin 2\theta\ \hat{\mathbf{y}} - \cos 2\theta\ \hat{\mathbf{z}}),
\end{aligned} \tag{3.3}$$

where d is the distance between the mirrors, and θ, $\theta' = \theta + \Delta\theta$, and ϕ, $\phi' = \phi + \Delta\phi$ are, respectively, the polar and azimuthal angles of rotation of M_1 (see inset of Fig. 3.5) and M_2, while $\Delta\theta$, and $\Delta\phi$ denote the small variations in the orientation of M_2.

Because there is no analytic solution of the aberrations such tilted systems add, we utilized a ray-tracing software with an interactive graphical user interface (GUI). Using this GUI allowed us to vary the parameters of that control the orientation of the mirrors and with the ray-tracing to retrieve data about the resulting phase modulation. In Fig. 3.6 we see a screenshot of the software we used and as an example we depict the configuration of the mirrors in order to produce a cubic phase modulation. The parameters in the ray-tracing were: the radii of curvature of the two mirrors were respectively $R_1 = 100$ mm, $R_2 = -200$ mm, the distance between the mirrors

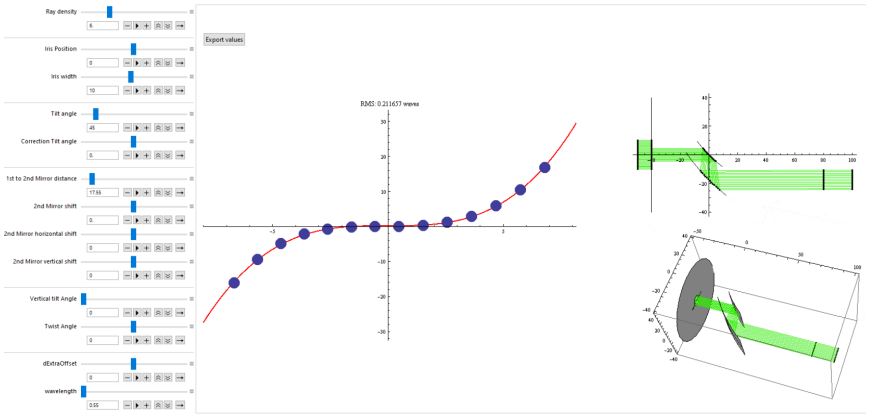

Figure 3.6: Ray-tracing software with interactive GUI. Here is depicted a cubic phase modulation. The parameters are: the radii of curvature of the two mirrors were respectively $R_1 = 100$ mm, $R_2 = -200$ mm, the distance between the mirrors is $d = 17.55$ mm, the tilt angle $\theta = 45^o$, while the wavelength was set to $\lambda_0 = 0.55$ μm.

is $d = 17.55$ mm, the tilt angle $\theta = 45^o$, while the wavelength was set to $\lambda_0 = 0.55$ μm. The resulting dynamic range of operation was $\sim 50 waves$, while the corresponding RMS wavefront error was 0.211 in waves.

We can now demonstrate the capability of the system shown in Fig. 3.5 to selectively introduce optical aberrations, in such a way so that each of the spatial polynomial phase term in Eq. (3.2) can be isolated. Using numerical raytracing we have simulated the optical behavior of the system for various configurations and our results are depicted in Fig. 3.7. Note that in all cases that are depicted in Fig. 3.7 the RMS phase error is less than 0.25 waves while the optical system was slightly perturbed from the basic mirror beam expander configuration to achieve the desired spatial phase modulation.

Quartic phase- In more detail, to achieve, as shown in Fig. 3.7(d), a pure quartic spatial phase distribution, we isolate the spherical aberration by adjusting the system parameters to:

$$d \simeq \frac{f_1 + f_2}{\cos\theta},$$
$$\phi = \pi/2,\ 0^o \leq \theta < 45^o,$$
$$\Delta\theta = \Delta\phi = 0,$$

where f_1 and f_2 are respectively the focal distances of first and second mirror.

Cubic phase- Likewise, to achieve, as shown in Fig. 3.7(c), a pure third power in the spatial phase, we have to isolate the coma aberration, the configuration is different:

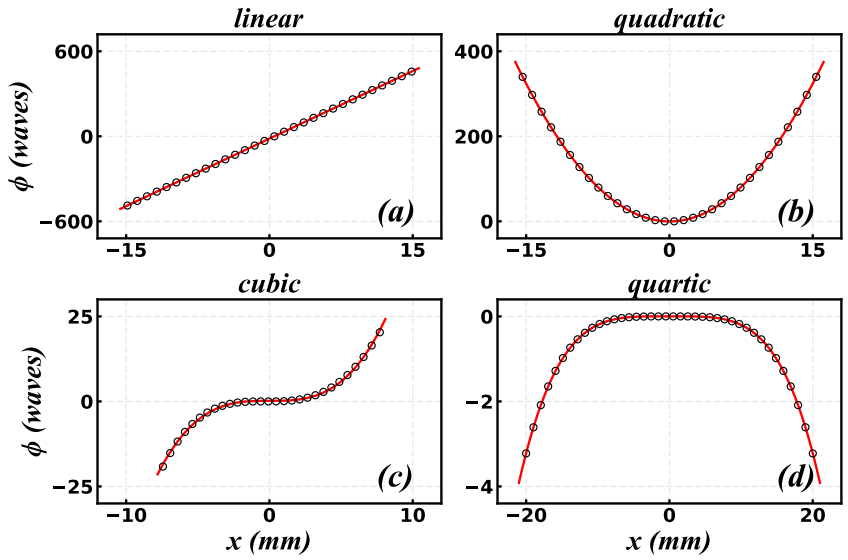

Figure 3.7: Spatial phase modulation introduced by the optical system (raytracing results) for various configurations enabling the isolation of power terms up to the 4^{th} order. Black circles denote the raytracing results while red curves are their respective fits. In our simulations the radii of curvature of the two mirrors were respectively $R_1 = 100$ mm, $R_2 = -200$ mm, while the wavelength is set to $\lambda_0 = 0.55$ μm.

$$d \simeq (f_1 + f_2)\cos\theta,$$
$$\phi = 0,\ 5^o \leq \theta \leq 45^o,$$
$$\Delta\theta = \Delta\phi = 0$$

Quadratic phase- We get a quadratic spatial phase modulation by varying the mirror distance by ΔL so that:

$$d \simeq \frac{f_1 + f_2}{\cos\theta},$$
$$\phi = \pi/2, 0^o \leq \theta < 45^o,$$
$$\Delta\theta = \Delta\phi = 0$$

Linear phase- Finally to achieve pure linear and quadratic spatial phase modulations, as shown in Fig. 3.7(a),(b) we use a similar configuration as in the case of quartic phase. Thus a linear spatial phase modulation is achieved

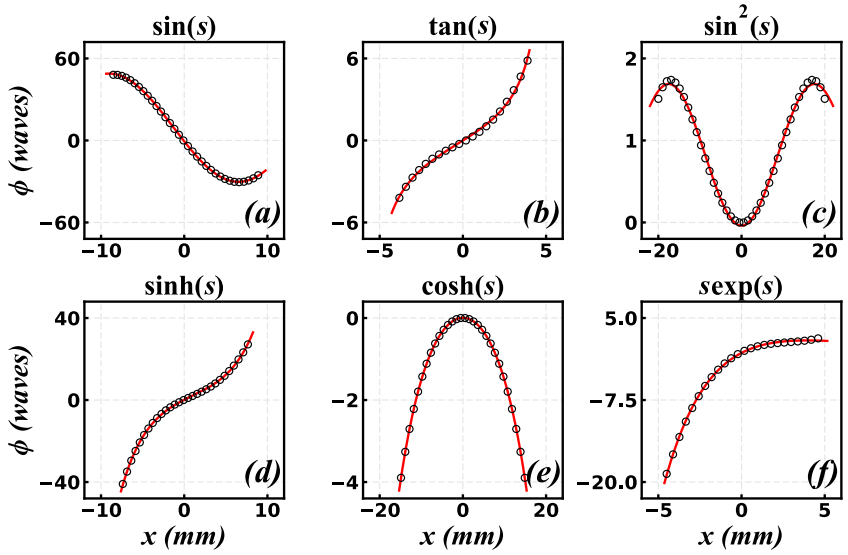

Figure 3.8: Spatial phase modulation (raytracing results) introduced by the optical system enabling the reconstruction of various functions.

by:

$$d \simeq \frac{f_1 + f_2}{\cos\theta},$$
$$\phi = \pi/2,\ 0^o \leq \theta < 45^o,$$
$$\Delta\theta = 0,\ \Delta\phi \neq 0,$$

Furthermore, the effective aperture of this reflective beam expander is practically limited only by the aperture of mirror M_2 since the entire mirror M_1 aperture can, in principle, be used. This behavior is superior compared to the previously presented [25] refractive optics variation of the device, since in that case the effective aperture is limited to only half of the input beam diameter. A direct way to increase the effective aperture of the reflective device is to proportionally increase the size of all elements, though with the cost of increasing the RMS error.

Operation regime

The next step is to demonstrate that this mirror expander can be actually used as a tunable, continuous phase mask. Our approach is to combine the various aberrations, or power terms as described in Eq. (3.2), so that according to the well known Taylor's theorem [22] we approximate any continuous phase distribution within the limits of the exit pupil. Using again numerical raytracing we have simulated the optical behavior of the system

Table 3.1: **Summary of the reconstruction quality of functional phase distributions presented in Fig. 3.8.**[a]

Functions	Polynomial approximation	Dynamic range (waves)	RMS (waves)
$\sin(s)$	$s - \frac{1}{6}s^3$	81	0.247
$\tan(s)$	$s + \frac{1}{3}s^3$	11	0.125
$\sin^2(s)$	$s^2 - \frac{1}{4}s^4$	1.8	0.037
$\sinh(s)$	$s + \frac{1}{6}s^3$	69	0.212
$\cosh(s)$	$1 + \frac{1}{2}s^2 - \frac{1}{24}s^4$	3.9	0.002
$s\exp(s)$	$s + s^2 + \frac{1}{2}s^3 + \frac{1}{6}s^4$	21	0.128

[a] All results are presented as a function of a normalized spatial coordinate $s = (x + x_0)/w$, where x_0 is a shift and w is a scaling factor.

and as depicted in Fig. 3.8 we have managed to achieve a variety of spatial phase distributions. In our numerical tests we have successfully achieved to produce phase perturbations that are described by specific functional distributions than among others include $\sin(s)$, $\cosh(s)$, $s\exp(s)$. A summary of the functional distributions along with the corresponding description by Taylor expansion series with terms up to the 4^{th} power, and their respective achieved dynamic range and RMS wavefront error is presented in Tab. 3.1. Note that in all cases the RMS error is kept either below, or well bellow $\lambda_0/4$, a value that constitutes the upper limit for any accurate wavefront reconstruction [111, 112]. Let's now consider the spectral bandwidth of operation of such a device. In our estimations we assume that all the surfaces of the device elements are cylindrical with ideal surface quality, so any limitations come from the optical design of the device. Since the induced spatial phase distribution is actually a geometric variation of the optical path we can write:

$$\Phi = \frac{2\pi}{\lambda_0} G(x, \lambda_0), \tag{3.4}$$

where λ_0 is the vacuum wavelength and $G(x, \lambda_0)$ is the spatial distribution of the optical path. When all elements composing such a device are achromatic, like the mirror beam expander presented here, G is wavelength independent while $\Phi \propto 1/\lambda_0$. This means that the device is an achromatic optical path modulator, and not an achromatic phase mask.

This type of achromaticity limits the useful spectral bandwidth, since for a device that is designed to operate at a wavelength λ_c to achieve dynamic range $\Phi_{\max}$ to its phase variation, there is a maximum wavelength of operation $\lambda_{\max}$ where the introduced phase variation becomes less than a

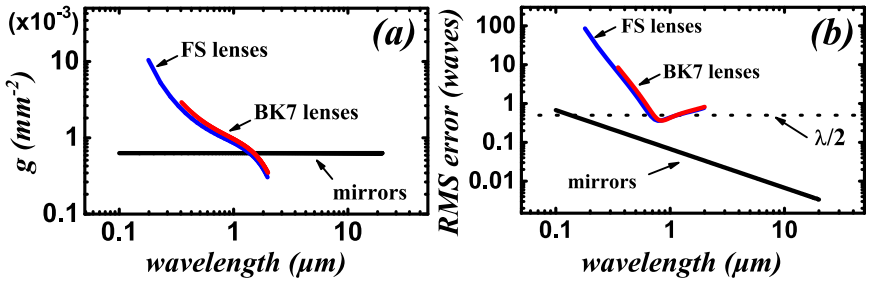

Figure 3.9: Comparison of reflective and refractive [25] beam expander phase generators in a spatial cubic phase configuration (raytracing results). (a) Induced cubic spatial phase strength $g = G/x^3$ and (b) RMS error, as a function of the wavelength. Reflective system (black curves), refractive system: (blue curves) fused silica (FS) lenses, (red curves) BK7 lenses.

threshold value, here set to 2π:

$$\lambda_{\max} = \frac{\Phi_{\max}}{2\pi}\lambda_c \tag{3.5}$$

On the other hand, the limitation from the shorter wavelength range is set by the quality of the acquired phase distribution, which is quantified by the RMS wavefront error of the distribution as compared to the desired ideal distribution. Assuming now that an RMS error $(\mathrm{RMS})_{\min}$ is achieved, at the design wavelength λ_c, there is a minimum wavelength of operation $\lambda_{\min}$ where the introduced RMS error becomes larger than $\pi/2$.

$$\lambda_{\min} = \frac{(\mathrm{RMS})_{\min}}{\pi/2}\lambda_c \tag{3.6}$$

As an example we will estimate the upper and lower spectral limits of operation, using the above mentioned criteria, of the configuration presented in Fig. 3.7(c). In this case since the design wavelength is $\lambda_c = 0.55$ μm, the device, without any alterations, can effectively operate in the range 0.33 $\mu\mathrm{m} \leq \lambda_0 \leq 22$ μm.

The spectral dependence of the device is more complex when its elements are not achromatic. In a beam expander composed by cylindrical lenses [25], the induced optical path G will also depends on wavelength due to the dispersion of glass. In this case we rely on numerical raytracing to analyze the spectral characteristics of the device since analytic, generic formulas like Eqs. 3.5-3.6 are not available. The spectral performance of a refractive device [25] compared to a reflective one, both configured to perform spatial cubic phase modulation, is shown as a function of the wavelength in Fig. 3.9. Clearly, in the refractive variant of the system, the cubic spatial phase strength g, and consequently the optical path G, strongly depends on the wavelength. The simulations have been performed for two glass types

(BK7 and Fused Silica) that have distinctly different Abbe numbers. The reflective system on the other hand shows a constant cubic spatial phase strength g, completely independent from the wavelength. Another important factor is the quality of the phase distribution, which can be quantified by its RMS error compared to the desired ideal distribution. As it is shown in Fig. 3.9(b) in refractive systems the RMS error varies strongly on the wavelegth and increases rapidly as we deviate from the design wavelength ($\lambda_c = 800$ nm in this case), exceeding $\lambda/2$ at a narrow spectral range around λ_c. The reflecting system on the other hand shows a monotonic decrease of the RMS error as the wavelength is increased, and exceeds the upper limit of $\lambda/2$ in the short wavelength range at $\sim \lambda_c/10$.

Scalability

Besides any limitations in the spectral bandwidth of operation, our proposed system is completely scalable in respect to the design wavelength. Let's assume that a device is optimized for operation at a wavelength λ_c and we need a new device that will now operate at a wavelength $\lambda_c' = m\lambda_c$, $(m > 0)$. The original design can be used as is, with all the distances and mirror physical dimensions scaled by a factor m, i.e. distance $d' = md$, radii of curvature $R_1' = mR_1,\ R_2' = mR_2$.

Achromaticity in the optical path versus achomaticity in the phase

As we have already mentioned in the previous section, a reflective device is achromatic in the optical path. In this section we will discuss on the differences between the achromaticity in the optical path and in the phase and their importance to applications. In a nutshell, any wavefront shaping device will modulate the phase of an incoming wavefront by perturbing the optical path. Replicating Eq. 3.4 the phase modulation Φ will be:

$$\Phi(x, \lambda) = \frac{2\pi}{\lambda} G(x, \lambda),$$

where λ is the wavelength and G is the optical path. In the case of a device that is achromatic to the optical phase, Φ does not depend on wavelength, thus the optical path is proportional the wavelength:

$$G(x, \lambda) = \frac{\lambda}{2\pi} G_o(x) \Rightarrow \Phi \propto G_0(x)$$

where G_0 is a function that depends only on x. This means that for a polychromatic input beam all its spectral components acquire the same phase.

On the other hand, in the case of a device that is achromatic to the optical path, G does not depend on wavelength, so the induced phase becomes:

$$\Phi(x, \lambda) = \frac{2\pi}{\lambda} G(x) \Rightarrow \Phi \propto \frac{1}{\lambda}$$

This means that shorter wavelengths will acquire higher phase modulation. Such a property is important to applications [115] as we are going to demonstrate though the following examples.

First, let's consider a device that induces a quadratic spatial phase modulation $\Phi \propto x^2$. Such a device will have an action similar to that of a thin lens and will focus a plane monochromatic wave front at a distance [116] f:

$$f = -\frac{2\pi}{\lambda}\frac{x^2}{\Phi(x,\lambda)}$$

If the device is achromatic to the optical phase Φ then we can safely assume that $\Phi(x,\lambda) = -Cx^2$ so the beam will be focused at a distance $f = \frac{\pi}{\lambda}\frac{1}{C}$. For a polychromatic beam this means that different colors will focus at a different distance so chromatic aberration is observed. On the other hand, if the device is achromatic to the optical path G then we can safely assume that $G(x,\lambda) = -Cx^2 \Rightarrow \Phi(x,\lambda) = -\frac{2\pi}{\lambda}Cx^2$ so the beam will be focused at a distance $f = \frac{1}{2C}$. For a polychromatic beam this means that all colors will now focus at the same point!

In our second example we will consider the more complex case of a cubic phase modulator that is used to generate 1D Airy beams [24]. As we are going to show a device that is achromatic in the optical path length (OPL), like the reflective continuous phase modulator we developed, produces Airy beams that co-propagate independently from their wavelength. This enables us to create broadband, non-spreading, white light Airy beams. In order to clearly demonstrate the differences of a system that is achromatic in phase to one that is achromatic in the optical path we performed numerical simulations of the paraxial wave equation for monochromatic beams at three different wavelengths $\lambda_B = 400\ \mu m$ (blue), $\lambda_G = 550\ \mu m$ (green), $\lambda_R = 700\mu m$ (red). Our comparative results are presented in Fig. 3.10. Clearly, when the device is achromatic in the optical path, as shown in Fig. 3.10(b), all colors co-propagate to result in a white Airy beam. On the other hand, when the device is achromatic in phase, as shown in Fig. 3.10(b), the spectral components of the generated beam are splitting as they propagate.

3.2.2 Discrete methods

Spatial light modulator

A spatial light modulator (SLM) is a device that imposes a modulation onto an incoming light beam, is either reflective or transmissive, and is a common light shaping tool. Spatial light modulators use a digital display, usually a LCOS type, to shape light by controlling each pixel individually and can be categorized to three main groups. First, amplitude-SLMs where they shape the spatial amplitude distribution of an incoming light beam, the phase-SLM where the phase of the light beam is modulated by the device,

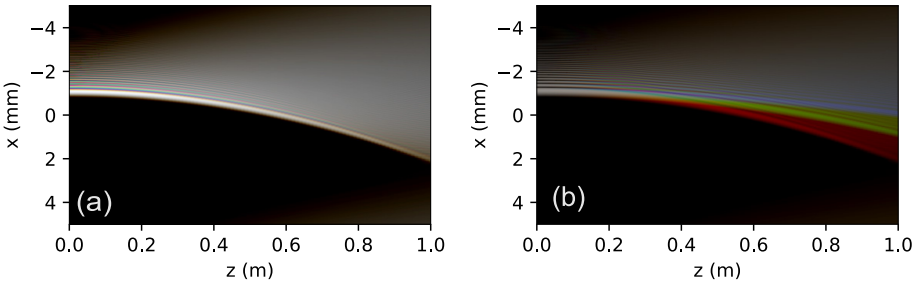

Figure 3.10: Numerical simulation results of Airy beams with width parameter $w = 100\mu m$ and wavelengths $\lambda_B = 400\mu m$, $\lambda_G = 550\mu m$, $\lambda_R = 700\mu m$ generated with a device that is achromatic in (a) optical path length and in (b) phase. The figures combined in ImageJ and we used pseudo-colors for illustration.

and more rarely an SLM that modify both the intensity and the phase of a beam. In this thesis we will focus on the techniques that we used to encode both amplitude and phase information onto a phase-only SLM and on the design of phase-only masks for the generation of complex structured light beams. Usually a phase-SLM exploits liquid crystals to impose a phase retardation to the incoming wave. In more detail, as liquid crystals are birefringent, they are imposing a phase retardation through the change of index of refraction that is dependent to the angle between the direction of the incoming wave, and direction that these crystals are aligned [117]. This behavior is illustrated in Figs. 3.11(a)-(c). The pixel by pixel control of the orientation of the nematic liquid crystals usually is achieved through the use of a CMOS back-plane, thus we are bale to have a pixel by pixel control of the phase modulation. Furthermore, as the display of the SLM is discretized, the reflection/transmission from it, produces diffraction orders, where the desired modulation is on the zeroth order. In order to achieve maximum efficiency on the zeroth order the polarization of the input beam must be aligned to the polarization plane of the SLM. This efficiency is usually $\sim 80 - 90\%$

Normally, a SLM is connected to a computer through a controller device for the transfer and the manipulation of the mask. This mask is loaded to the SLM as an image type file (usually a bitmap image file (BMP)), which is computer generated. For phase SLMs the phase modulation that can be achieved is usually a few wavelengths ($\sim 2\pi$), thus a phase wrapping of the phase imprinted into the phase mask is required. Furthermore, the resolution of the commercially available phase-SLMs * is ranging form 800×600 pixels to 4160×2464 pixels, wile the pixel pitch is between $2\mu\text{m} - 40\mu\text{m}$. A typical setup for the operation of an SLM is illustrated in Fig. 3.12.

*Info taken from hamamatsu.com, holoeye.com, thorlabs.com.

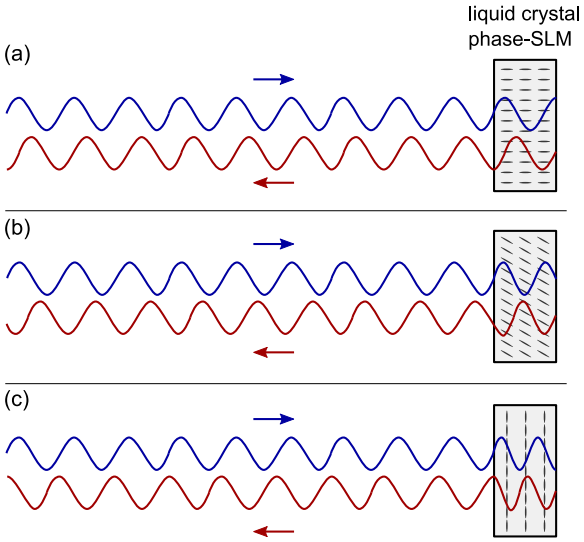

Figure 3.11: Schematic representation of the operation of a phase-SLM using Liquid Crystals.

When an incoming light beam is reflected by an SLM the outgoing beam is imposed with the desired modulation induced by the nematic liquid crystals, by altering the orientation of the crystals with respect to the incoming wave.

The design of the masks loaded into an SLM for the generation of structured light is not a trivial task. Besides the more simple cases, where a straightforward phase distribution, like a polynomial or a helical phase, is needed for the modulation of a light beam, often o more complex phase distribution, and in many cases both intensity and phase modulation, is required.

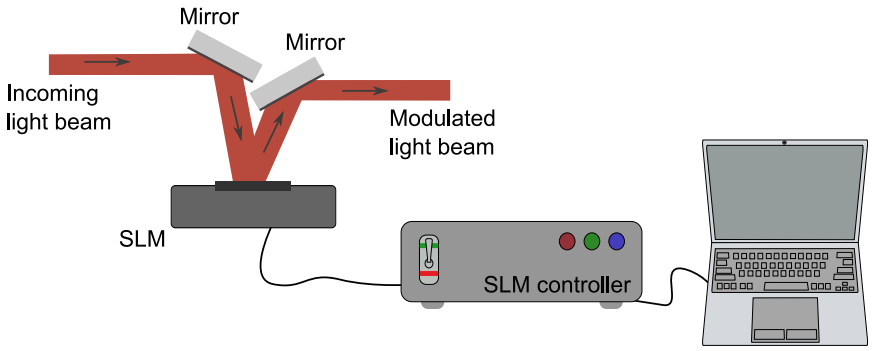

Figure 3.12: Illustration of a typical setup of the operation of a reflective SLM.

3.3 Design of Phase-masks

Although the introduction of SLMs has made it possible modulate light with unrepresented control and precision, the generation of complex structured light, is still not a trivial task. Generating structured light is actually a transformation process, where some input beam is reshaped to transform to the required structured light distribution. Transformation can be a single step process, like for example when a thin lens imprints a quadratic phase on a plane wave to transform it to a spherical. On the other hand, the transformation might require several steps, including propagation over a distance. An example of such a process is holographic reconstruction [118], where a reference light beam is modulated in amplitude by the hologram, and transforms to the object wave as it propagates. Irrespective of the number of steps required, one has to design and apply a specific modulation to an incoming light field. This modulation might refer to the phase, the amplitude, the polarization or any combination of them. In the absence of generic analytical approaches one has to rely on numerical simulations, or even machine learning techniques, that will correlate the required input modulation for a specific output.

Physical or technical limitations of the available equipment can play also an important role and should be taken into account in the design phase. For instance, most of the available SLMs can modulate either the phase or the amplitude, but not both. Furthermore, SLMs are discrete devices with finite dynamic range, pixel size that ranges from $5-40$ μm, physical dimensions in the range of ~ 100 mm^2. For example phase SLMs can modulate a beam with a maximum phase modulation slightly higher than 2π, thus we have to rely on phase wrapping to achieve larger spatial phase modulations. Although a Spatial Light Modulator is a device that gives more degrees of freedom and control, over light structuring, there some limitation that must be taken into account. As they are discretized and consisting of pixels with finite physical dimensions, it is not possible to reproduce modulations that are steeper than the sampling period. Another limitation comes form the physical dimensions of the screen, which limits the resulting NA, of the structured light wave. Moreover is limited in it dynamic range because as the maximum phase modulation it can achieve is $\sim 2\pi - 3\pi$, thus a phase wrap is needed for phase masks with larger value of maximum phase modulation.

3.3.1 Encoding amplitude and phase information onto phase-only masks

Encoding amplitude and phase information onto phase-only masks is a an exciting approach for the generation of structured light. Since the majority of the high-power light modulating devices are phase modulators such an approach can enable us to generate intense structured light. We can better

understand the complexity of such a approach through a simple example. If we modulate the phase of a plane wave $u(\mathbf{r},t) = u_0 e^{i(\mathbf{k}\cdot\mathbf{r}-\omega t)}$, where $\mathbf{k}$ is the wavevector and ω is the angular frequency, by a modulation $b(\mathbf{r})$ we will get:

$$u'(\mathbf{r},t) = e^{ib(\mathbf{r})}u(\mathbf{r},t)$$

We can then take the Taylor series expansion of this modulation to:

$$u'(\mathbf{r},t) \simeq \left[1 + ib(\mathbf{r}) - \frac{b(\mathbf{r})^2}{2} - i\frac{b(\mathbf{r})^3}{6} + \dots\right] u(\mathbf{r},t)$$

We can identify amplitude modulation terms in the above description. Likewise, if the modulation is very weak $b(\mathbf{r}) \ll 1$ then we can keep only the fist order term:

$$u'(\mathbf{r},t) \simeq [1 + ib(\mathbf{r})]\, u(\mathbf{r},t)$$

Clearly we can now identify two components, the original plane wave and an amplitude modulated wave which is $\pi/2$ shifted in phase. So under these conditions a weak phase modulation can actually modulate the amplitude of incoming wave. On the other hand, in our example phase and amplitude modulation seem coupled and difficult to be independently controlled.

A solution to this problem was presented by [119] et al. in 1999. In this paper the imposed phase modulation was the product of the, properly modified, required phase and amplitude modulation. This modification, inspired by analyzing the problem through a Fourier series expansion, made it possible to decouple amplitude and phase modulation.

3.3.2 Phase-only masks for the direct generation of Structured light

Although in general the generation of structured light would require a modulation in both amplitude and the phase, in some cases a direct phase modulation is all that needed. For example, Airy beams require only a phase modulation. This can be either a cubic phase imposed into a Gaussian beam followed by a Fourier transform using a lens [24], or using a direct 3/2 phase modulation [79]. The latter approach is based on the approximation of the Airy function by $Ai(x) \simeq x^{-1/4}\exp(iCx^{3/2})$, where C is a constant.

Generation of ring-Airy beams

Based on this approximation, we use direct phase modulation schemes to generate a variety of accelerating beams, like ring-Airy beams whose amplitude distribution is described by the Airy function. An example of the generation of abruptly auto-focusing vortex beams using phase-only modulation was presented in [35]. Following that, in our work we explored a

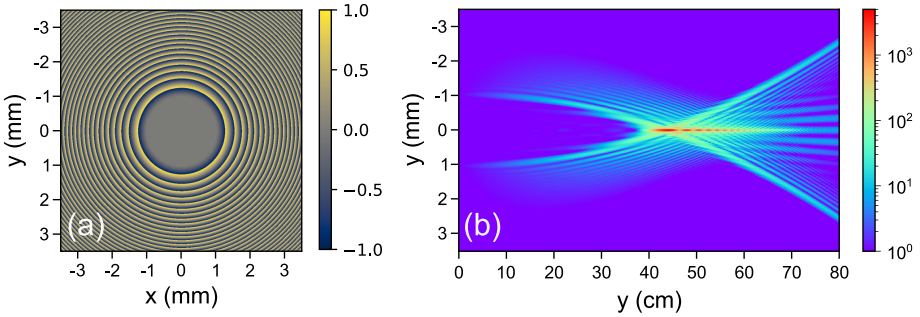

Figure 3.13: (a) phase mask of cylindrically symmetric chirped phase described in Eq. (3.7), and (b) the intensity distribution along propagation of the corresponding ring-Airy.

variation of this approach for the generation of ring-Airy beams, that was first presented in [30]. This technique is based on a chirped phase modulation scheme proposed in [86], which can be viewed as an extension to cylindrical symmetry, of the approach presented by [79]. In our work a phase-only mask is used with a phase distribution described by:

$$\phi(r) = \begin{cases} -kC(r-r_0)^{3/2} & , r \geqslant r_0 \\ 0 & , r < r \end{cases} \tag{3.7}$$

where C is a constant, k is the wavenumber, r is the radial coordinate, and r_0 is a reference radius. Such a phase mask is depicted in Fig. 3.13(a) with $r_0 = 1$ mm and $kC = 0.1$ m$^{-}1/2$, meanwhile the intensity distribution along propagation of an ring-Airy beam generated with a Gaussian beam with $FWHM = 10$ mm illuminating this mask is shown in Fig. 3.13(b).

Adding Orbital Angular Momentum (OAM) to ring-Airy beams

Orbital angular momentum can be added to a beam by modulating it's phase with a vortex. This vortex can be applied as for example, linear azimuthal variation of the phase $\psi(\theta) = m\theta$, where θ is the azimuth angle and m is the topological charge or the number of twists in the phase over a full rotation. Ring-Airy vortex beams, can be directly generated by adding a helical phase to the 3/2 phase chirp described in Eq. (3.7). In this case the phase modulation is described by:

$$\Phi(r) = \phi(r) + \psi(\theta) = \begin{cases} -kC(r-r_0)^{3/2} + l\theta & , r \geqslant r_0 \\ m\theta & , r < r \end{cases} \tag{3.8}$$

Fig. 3.14 depicts a ring-Airy beam carrying OAM of topological charge $m = +1$. Beams that carry OAM exhibit an interesting property. At the center of their vortex ($r = 0$ in our case), due to the phase ambiguity, the

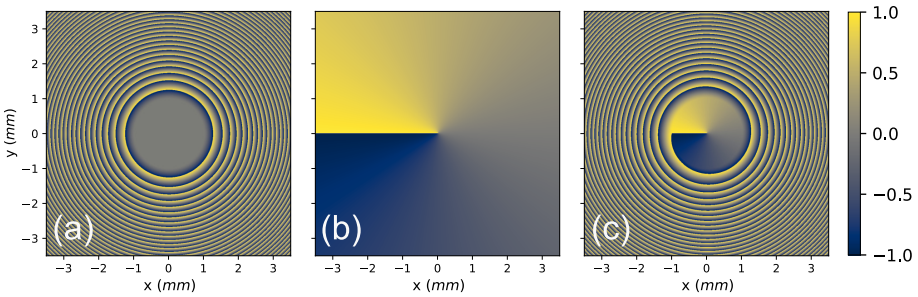

Figure 3.14: Transverse $x-y$ phase distribution of (a) 3/2 chirp phase with $r_0 = 1.0mm$ and $C = 0.100\ m^{-1/2}$, (b) helical phase with topological charge $m = +1$ and (c) combined chip phase and vortex $(\phi(r) + \psi(\theta))$ at the initial plane (z=0). Phase is in π units.

intensity is zero. So, when such beams are focused they from a hollow focal region. This characteristic is also evident in the case of autofocusing beams as we can see in Fig. 3.15. In more detail, Fig. 3.15(a) shows the $I(x, z)$ intensity cross-section of the vortex ring-Airy beam described in Fig. 3.14 using Gaussian beam with $FWHM = 10$ mm to illuminate the phase mask, while in Fig. 3.15(b) the corresponding maximum peak intensity I_{max}/I_0 along propagation is depicted. The characteristic auto-focusing behavior of the ring-Airy beam can be clearly observed.

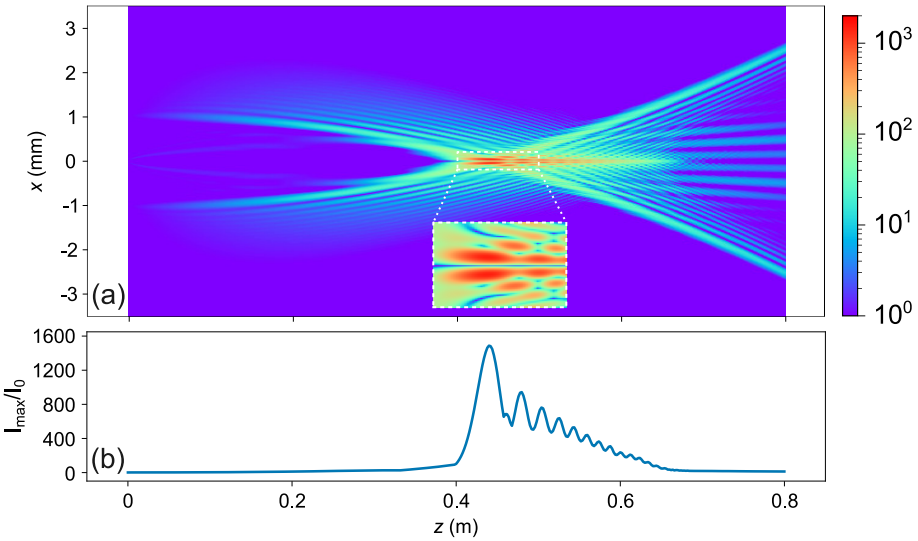

Figure 3.15: Intensity distribution of ring-Airy vortex along propagation (a) $x-z$ intensity cross-section, and (b) maximum peak intensity I_{max} normalized with initial intensity I_0. Inset shows a zoomed-in area of the hollow focal region.

3.4 Interfering structured light beams

Although the generation of a single structured beam that require both amplitude and phase modulation, for instance an abruptly auto-focusing ring-Airy beam, can be achieved using several techniques, and different approaches [42, 30, 86], on the other hand the creation of multiple interfering beams using a single mask is a challenge. There is a variety of cases where the combination of multiple beams is needed, in this work we focus on the design techniques for the generation of Tornado waves [101], which are composed by the interference of two ring-Airy beams, with different initial parameters, both carrying an helical phase of opposite topological charge.

3.4.1 Spatial multiplexing technique

Brimis at al. in [101], showed that ToWs can be generated by superimposing two ring-Airy beams that, although follow different parabolic trajectories, are tuned to abruptly auto-focus at overlapping focal regions while carrying OAM of opposite helicity [101]. For the generation of ring-Airy beams, either using a straightforward phase- only or a Fourier transform method, usually a phase or amplitude SLM is required [42, 30]. To extend these approaches to ToWs that are interfering fields is not straightforward. For instance, taking the simple case of two plane waves, with phase modulation as $\exp(i\Phi_A)$, $\exp(i\Phi_B)$, where Φ_A, Φ_B refer to the spatial phase distribution of each wave. Both of them can be independently generated using a phase SLM by applying the corresponding spatial phase distribution as shown before. On the other hand, their superposition involves an amplitude and phase modulation $\exp(i\Phi_A) + \exp(i\Phi_B) = 2\cos(\frac{\Phi_A - \Phi_B}{2})\exp(i\frac{i\Phi_A + i\Phi_B}{2})$ that a phase SLM cannot directly reproduce. The sum of these two phase terms is not the sum of the two phase distributions, therefore by adding the two phase distributions it does not reproduce the desired amplitude and phase modulation of the superposition of the two vortex ring-Airy. Furthermore, when the two phase distributions are opposite as in the case of the two superimposed waves of the ToWs, the sum of the overlapping region where the helicities are opposite $\exp(i\Phi_A) = -\exp(i\Phi_B)$ is zero. Although a simple solution to this problem is using two independent phase SLMs for the generation of the two distinct vortex ring-Airy beams here we follow simpler approach, using a single SLM device. To avoid the phase cancellation due to the spatial overlap of the phase distributions we apply a spatial multiplexing technique for the design of a single phase mask that imposed onto the SLM. Using this approach, superimposed fields of any complexity in their phase structure can be generated. In more detail the technique we developed is based on time-division multiplexing (TDM), which regularly used to alternately combine different frequencies in telecommunications in the time domain, here applied in the spatial domain. As an example we will first describe our approach

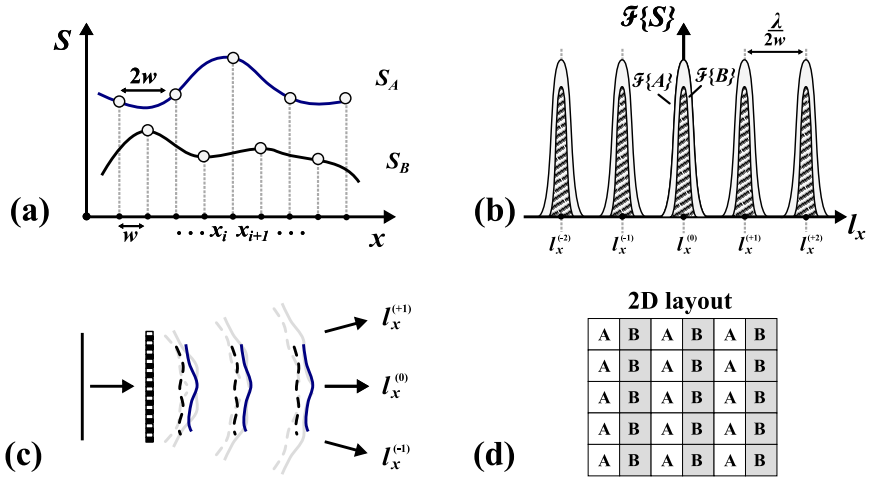

Figure 3.16: Representation of the spatial multiplexing technique (a) Two 1D signals A, B alternatively sampled at $2w$ spatial intervals with a w shift between them (b) Fourier transform $\mathcal{F}$ of the sampled signals, (c) sampling geometries in a 2D SLM array, (d) Propagation and angular separation of the diffraction orders

for 1D phase distributions. Assuming that we use a discrete device with a w sampling interval. As shown in Fig. 3.16(a), two continuous distributions $S_A(x),\ S_B(x)$ can be alternately sampled, each one at $2w$ intervals, with a w shift between them. In this case the signal $S(x)$ on the device is described by:

$$S(x) = S_A(x)comb(\frac{x}{2w}) + S_B(x)comb(\frac{x+w}{2w}) \tag{3.9}$$

where $comb(x) = \sum_{i=-\infty}^{+\infty} \delta(x-i)$ and $\delta(x)$ is the delta function. The Fourier transform of this discrete, multiplexed signal with then takes the form:

$$\mathcal{F}\{S\} = 2w\left\{\mathcal{F}\{S_A\} + \mathcal{F}\{S_B\}\, e^{ikwl_x}\right\} * comb(\frac{kwl_x}{\pi}) \tag{3.10}$$

where $k = 2\pi/\lambda$ is the wave number and l_x is the directional cosine. Assuming that both signals are band limited, i.e their spatial spectrum $\mathcal{F}\{S_A\}$, $\mathcal{F}\{S_B\}$ is non zero in a finite region, the resulting spatial spectrum is comprised by a periodic repetition of the spatial spectra [116] as it is graphically represented in Fig. 3.16(b). The periodic spatial sampling results in a grating like effect where each of the diffraction orders represents a replica of the original distributions. Interestingly, as graphically depicted in Fig. 3.16(c), the diffraction orders propagate in different directions. This angular separation is a key element of our approach since by simple propagation all diffraction orders besides the zero can be easily filtered out by the finite NA of the optical setup. The scheme for applying this multiplexing in a 2D SLM device

is shown in Fig. 3.16(d) where the values of $S_A(x)$, $S_B(x)$ distributions are represented in alternating pixel columns. For example for an SLM device with a typical pixel size of $w = 10$ μm operating at $\lambda = 1$ μm the angular separation between the zero and the first order is 2.86 deg corresponding to a numerical aperture of NA=0.05, or a spatial separation of 50 mm after propagating for 1 m. We have to note here that in a more rigorous representation, that we are going to present elsewhere, one should take into account the finite pixel size and shape as well as the aperture of the SLM device. In this case the diffraction orders are suppressed in power compared to the zero order, further enhancing the effectiveness of our approach.

3.4.2 Phase-masks design for the generation of Tornado waves

For the generation of spiraling structured light that we refer to as Tornado Waves we applied this multiplexing approach to generate by superimposing accelerating waves u_A, u_B carrying OAM. In more detail, for each of the superimposed fields a phase mask was designed following an approach similar to [85, 30, 79] as we described in 3.3.2. The phase in each phase mask can be described as $\Phi(r,\theta) = \varphi(r) + \psi(\theta)$ where $\varphi(r) = -kC(r-r_0)^{3/2}, \forall r \geq r_0$, (and $\varphi(r) = 0, \forall r < r_0$) is a radially chirped phase distribution, $\psi(\theta) = m\theta$, is a helical phase and r is the radial coordinate, r_0 is a reference radius, C is a constant, k the wavenumber, θ is the azimuthal angle, and m is the topological charge.

In our design we have tuned [101] the foci of u_A, u_B to overlap. The position of the abrupt autofocus of a ToW can be estimated with good accuracy using the analytical solution of the one-dimensional Airy beam [101, 27, 42]. In our case, since we are using a generation approach similar to [79] using the parabolic trajectory of the caustic resulting from phase distribution Φ, we estimate that the position of the abrupt autofocus is at

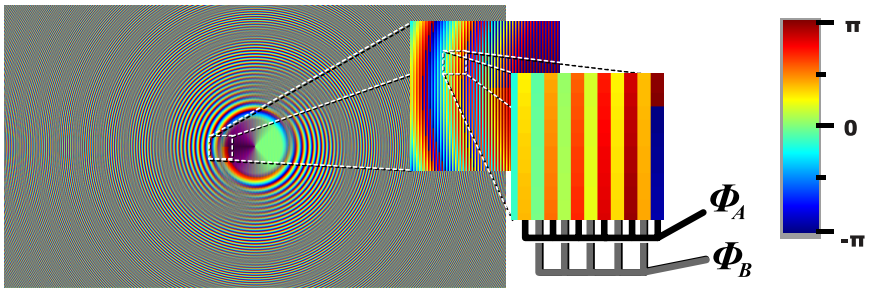

Figure 3.17: Phase mask for the generation of ToWs (wrapped phase). Insets zoom in the phase mask to reveal the alternating sampling geometry for the individual masks Φ_A, Φ_B that respectively generate each of the superimposing accelerating waves.

$f = \frac{4}{3C}\sqrt{r_0}$, where C is the constant determining how strong is the radial chirp phase. As we can observe from the above relation the focus position is independent of the wavelength. The individual phase masks Φ_A, Φ_B were then spatially multiplexed as depicted in Fig. 3.16(d) to a single phase mask that was used in the SLM. The resulting multiplexed phase mask is shown in Fig. 3.17. From the insets we can observe in detail the effect of spatial multiplexing of the individual phase masks Φ_A, Φ_B.

4 | Experimental observation of structured light

4.1 Ultra-broadband White-light 2D Airy beams

For the experimental demonstration of the ability of the proposed mirror beam expander system to operate as a continuous phase mask we have chosen to work in a spatial cubic phase configuration. This configuration enables the generation of accelerating non-diffracting Airy beams, [24, 92, 25, 76, 120], since a Gaussian beam modulated by a spatial cubic phase can be directly converted to Airy beam by Fourier transforming (FT) using a lens [24]. Our proposed phase mask is superior from an SLM but also from the previously reported refractive variant [25] in respect of the bandwidth, efficiency and and input power limit. The ability of such devices to achieve a continuous spatial phase avoids all discretization side effects present in SLM devices. Furthermore, since our device is achromatic in respect of the optical path difference it results in the generation of broadband accelerating Airy beams [115]. In addition using our device we were able to generate accelerating beam with variable partial spatial coherence and study its affect upon their propagation dynamics. As well as to investigate the self-healing properties of partially coherent accelerating beams. An image of the experimental setup of the broadband reflective phase modulation device is shown in Fig. 4.1. Fig. 4.1(a) depicts the system with a configuration to impose a pure cubic phase modulation, while Fig. 4.1(a) show a zoomed-in image of one of the systems that show the direction of the light through the mirrors M_1 and M_2.

Fig. 4.2 depicts a graphical representation of our setup and shows that the 2D cubic spatial phase mask was implemented by cascading two orthogonally orientated cylindrical mirror beam expanders. A broadband white light Gaussian beam, after propagating through the two orthogonally oriented optical systems is modulated by a cubic spatial phase in both transverse axes and is then FT by a lens resulting in a 2D Airy beam [24, 25]. In general the field distribution of a 2D Airy beam at the initial plane is described by

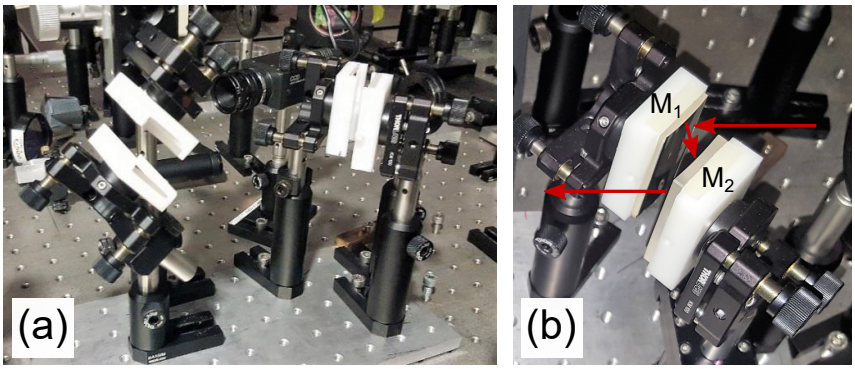

Figure 4.1: Image of the experimental setup of the broadband reflective phase modulation device, (a) configured for a two dimensional pure cubic phase (b) a zoom in image of one of the systems that show the direction of the light through the mirrors M_1 and M_2.

[24]:

$$u(x, y, z = 0) = \mathrm{Ai}(\frac{x}{w_x})\mathrm{Ai}(\frac{y}{w_y})\exp(\alpha_x \frac{x}{w_x})\exp(\alpha_y \frac{y}{w_y}) \tag{4.1}$$

where $\mathrm{Ai}(\cdot)$ denotes the Airy function, $w_x,\ w_y$ are the primary lobe width parameters, and a_x, a_y is the apodization factors in each direction. As the beam propagates it's distribution is displaced in such a way so that the primary lobe follows a parabolic trajectory [24, 92, 25] $\boldsymbol{r}_{\max} \simeq \left(w_x^{-3}\hat{\mathbf{x}} + w_y^{-3}\hat{\mathbf{y}}\right)(z/2k)^2$. Thus the beam exhibits a stronger deflection when the width parameter is decreased or the wavelength is increased.

Since our phase mask device is comprised by achromatic elements the imposed geometric optical path, ignoring the dispersion of air, is $G(x, y) = g_x x^3 + g_y y^3$, where g_x, g_y are constants related to the achieved dynamic range. Taking into account the Fourier transforming action of a focusing element, like a lens, of focal distance f, and the imposed phase distribution described in Eq. (3.4) we can estimate the width and truncation parameters of the generated 2D Airy [24, 92]:

$$w_i = \sqrt[3]{3}\ k^{-2/3} f g_i^{1/3}, \quad (i = x, y) \tag{4.2}$$

$$a_i = k^{-2/3} \frac{g_i^{-2/3}}{\sqrt[3]{9} w_G^2}, \quad (i = x, y) \tag{4.3}$$

where w_G is the waist radius of the input Gaussian beam. Using Eq. (4.2)-(4.3) we can then estimate the transverse displacement of the generated Airy beam as a function of the wavelength.

$$\boldsymbol{r}_{\max} \simeq \left(g_x^{-1}\hat{\mathbf{x}} + g_y^{-1}\hat{\mathbf{y}}\right) \frac{z^2}{12 f^3} \tag{4.4}$$

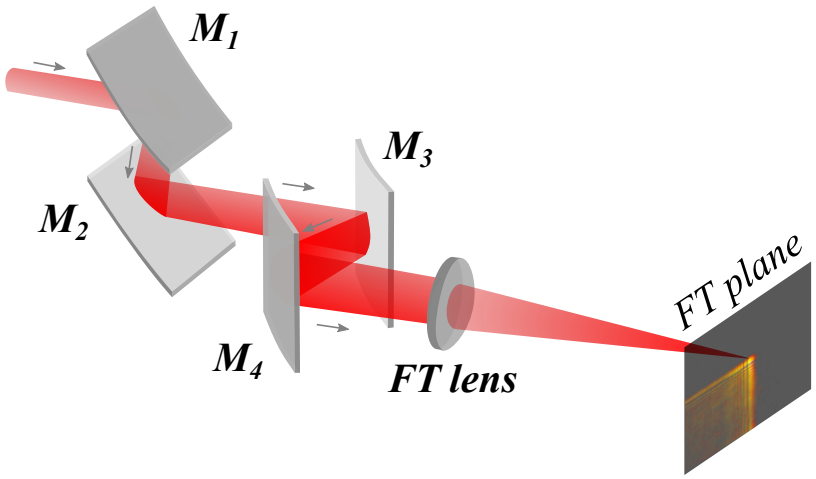

Figure 4.2: Graphical representation of a reflective phase generator (RPG) configured to imprint a cubic spatial phase to the incident wavefront. The radii of curvature of cylindrical mirrors M_i, $(i = 1, \ldots, 4)$ is respectively $(R_1 = R_3 = 102$ mm, $R_2 = R_4 = -153$ mm), (FT) is an achromatic lens of focal length $f = 300$ mm that performs the optical Fourier transform.

Interestingly, for such a phase mask [115], and if the FT focusing element is achromatic, the traverse displacement does not depend on wavelength. In this case the width parameter for each spectral component is effectively auto-adjusted (see Eq. (4.2)) so that it compensates the wavelength related deflection variations. Thus using such a device ultra-broadband Airy beams can be generated [115], which when combined with an Airy temporal profile can support ultra-short Airy^3 light bullets [76]. Using the proposed phase mask we have generated white light 2D accelerating Airy beams as shown in Fig. 4.2. For illumination we used spatially filtered and collimated light from a white light LED (450 nm - 750 nm). The transverse beam profile was imaged using a linear 14bit CCD camera for various propagation distances. Details on the experimental setup can be found in [25]. furthermore we used band-pass interference filters (40nm) to isolate different parts of the LED spectrum and generate 2D Airy beams of different colors. The transverse intensity profiles of these 2D Airy beams are shown in Fig. 4.3. Using those interference filters we have isolated the propagation of each spectral component and as shown in Fig. 4.4(a),(b) the trajectories in the transverse direction of the intensity maximum are, as predicted in Eq. (4.4), independent of the wavelength. The generated white light 2D Airy beam sustains over 50% of its initial peak intensity for a propagation distance of 60mm, a value which is ~ 4 times larger than that of a similarly sized Gaussian beam (FWHM $\simeq 50\mu$m). Our results, retrieved in a broad spectral range $(\Delta\lambda_0/\lambda_0 \sim 0.54)$, are comparable to previously demonstrated white light

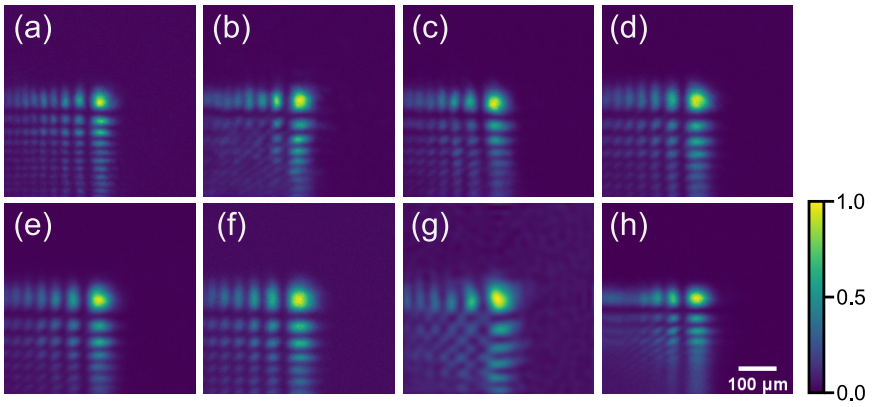

Figure 4.3: Transverse intensity profiles of 2D Airy beams in different part of the spectrum. The corresponding central wavelength is (a) $\lambda_c = 450$nm, (b) $\lambda_c = 500$nm, (c) $\lambda_c = 550$nm, (d) $\lambda_c = 600$nm, (e) $\lambda_c = 650$nm, (f) $\lambda_c = 700$nm, (g) $\lambda_c = 750$nm. (h) Shows a white light 2D Airy beam (450 nm - 750 nm).

Airy beams [121, 115]. Moreover, Fig. 4.4(c) shows a color image of the white light 2D Airy beam captured using a photographic camera. Our experiments clearly show the potential of such an optical device to be used as an ultra-broadband phase mask.

4.2 Coherence control of 2D Airy beams

The formation of Airy beam relies on the wave nature of light since the characteristic curved trajectory is a result of the interference of different parts of the Airy's initial field distribution [122, 72, 123]. Thus, we expect that the spatiotemporal coherence of the light used for its generation would have a strong effect upon the Airy beam properties. Several approaches that study the effect of partial coherence have been presented in the bibliography. In all of them partial spatial coherence was somehow simulated. For example in [122], a rapidly rotating ground glass was used to induce a random spatial phase distribution in a by all other means coherent accelerating beam. In this case, the observation interval (CCD camera integration time) was set to be much longer than the timescale of the induced phase variations, leading to an averaging effect that practically simulates spatial incoherence.

4.2.1 Spatial coherence of 2D Airy beams

For the generation of the ultra-broadband white 2D Airy beams we used a technique described in 3.2.1. Using reflective optics as continuous phase masks in order to generate Airy beams we have significant advantages in

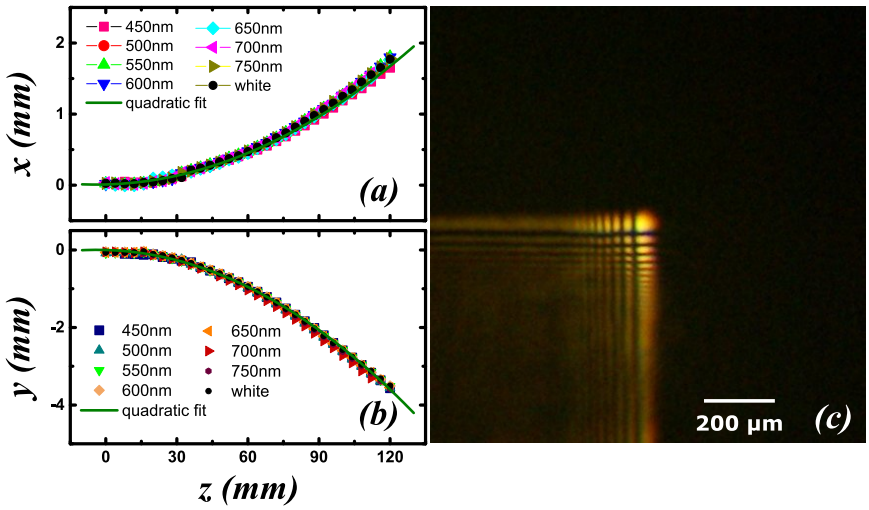

Figure 4.4: Trajectory of the primary lobe of 2D Airy beam generated with RPG in (a) x-axis and (b) y-axis (c) White light 2D Airy beam. (PRG properties: Dynamic range of 20 waves, RMS error of 0.2 waves)

terms of the output quality and the intensity of the beam as well as in its spectral content. As shown in Fig. 4.5, for illumination we used a white LED (450 nm-750 nm), while a condenser lens was used to collect light and loosely focus it on a pinhole. A lens, was then used to collimate the beam that in turn illuminated the telescopic cylindrical mirror system. As we are going to describe in detail later, using pinholes of different diameter, allows us to vary the degree of spatial coherence of the collimated beam. A smaller pinhole increases the spatial coherence while a larger one decreases it the analytic relation is described in 1.4.2. The degree of temporal coherence on the other hand was varied by narrowing the spectral bandwidth using interference filters. Narrowing the spectrum increases the temporal coherence. An achromatic spherical lens was used to finally generate the broadband 2D Airy beam.

Measurement of spatial coherence

Although is rather straight forward to vary the spatial coherence of a beam by changing the size of the illumination pinhole as shown in Fig. 4.5, it is not trivial to quantitatively characterize these changes. In general the mutual coherence function [2] for a field $u(\mathbf{r}, t)$ is described as:

$$\Gamma(\mathbf{r_1}, \mathbf{r_2}, \tau) = \langle u^*(\mathbf{r_1}, t) u(\mathbf{r_1}, t + \tau) \rangle \tag{4.5}$$

where $\mathbf{r_1}, \mathbf{r_2}$ are the positions of two points on the wavefront, τ is a time delay and $\langle\ \rangle$ denotes averaging. To characterise the temporal coherence

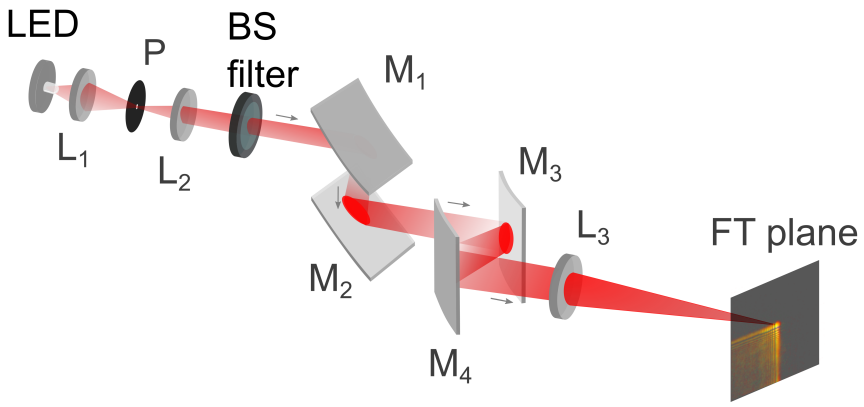

Figure 4.5: Illustration of the setup was used for the generation of 2D Airy beam with partial spatial and temporal coherence. L_1 collects light from the white light LED and loosely focuses it onto the pinhole P. L_2 collimates the beam, which then enters the cubic phase modulation device consisting of mirrors M_i, $(i = 1, \ldots, 4)$. BP is a band pass filter, which is removed in for the white light measurements. L_3 is a Fourier Transforming lens used to transform the cubic phase modulated beam to a the 2D Airy beam.

of a beam one needs to measure $\Gamma(\mathbf{r_1}, \mathbf{r_1}, \tau)$, thus requires some kind of correlation over time. This can be achieved by varying the OPD between two the arms of a Michelson interferometer that is illuminated by our beam. Such a measurement is rather trivial when a beam is spatially coherent, but rather challenging when the spatial coherence is low.

Measuring spatial coherence on the other hand is always a demanding process. Since we need to measure $\Gamma(\mathbf{r_1}, \mathbf{r_2}, 0)$, some kind of correlation over space is required. One needs to bring to interference different parts of the beam and vary their distance without affecting the temporal delay. Most techniques presented in the bibliography rely either on some configuration similar to a Young's experiment [124] or on using mirrors to fold the beam [125] so that symmetric points are brought to interference. A novel approach to solve this technically challenging problem was recently introduced by A. Bhattacharjee et al. [126]. Their technique uses a variation of the Michelson interferometer, in which, as depicted in Fig. 4.6, a converging lens is placed in one of the interferometer arms in such a way so that it's focus is on the plane of the interferometer mirror. In more detail, the collimated beam under study is then splitted using a cube beam splitter, into two parts. One part is reflected by the mirror M_2 while the other part is focused by the lens L_1 onto the mirror M_1 The reflected beams are recombined on beam splitter and their resulting interference pattern is imaged on a digital camera. As show in the inset of Fig. 4.6 the lens L_1 inverses the transverse profile of the beam so at any point $P(x, y)$ on the sensor we observe the superposition of

the original field $u(x, y, t)$ with it's inverted replica:

$$u_{tot}(x, y, t) = u(x, y, t) + u(-x, -y, t)$$

thus at a radial distance $r = \sqrt{x^2 + y^2}$ we observe the correlation of two points on the beam that are separated by a distance $2r$. Adding a small tilt to mirror M_2, and then properly adjusting the delay, breaks the cylindrical symmetry of the interference pattern and leads to linear fringes that can be more easily characterized. A typical measurement for white light illumination is shown in Fig. 4.7 while the inset shows a typical of the fringes. The spatial coherence length is estimated by measuring the FWHM of the of the decaying intensity oscillation. Clearly in this case the spatial dimensions over which the beam is coherent is $\simeq 425\mu$m..

We used the above mentioned modified interferometer to characterize the coherence of the beam used to illuminate the mirror phase generator device. We measured the corresponding spatial coherence for a variety of illumination pinhole diameters. In Fig. 4.8 the spatial coherence as a function of pinhole diameter is given, as expected spatial coherence decreases monotonically with the pinhole diameter.

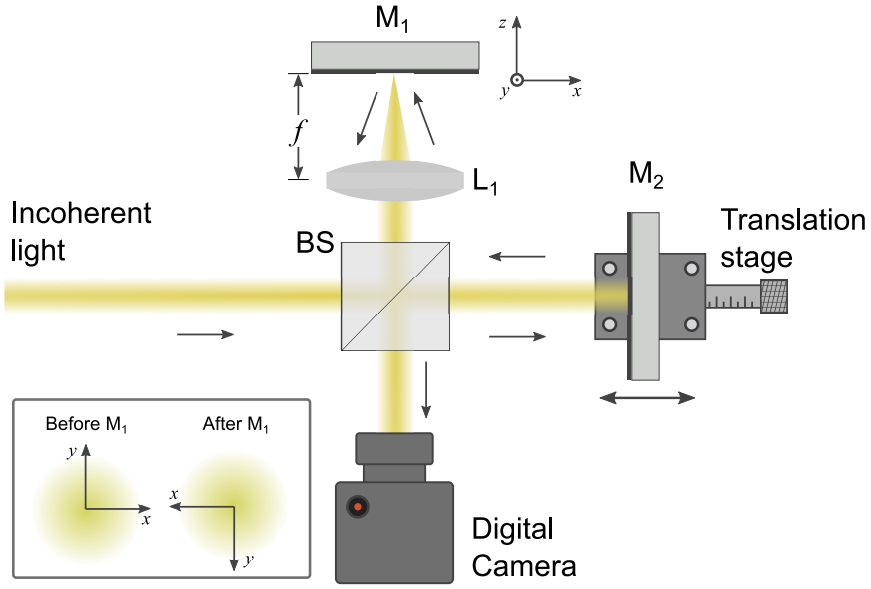

Figure 4.6: Graphical representation of the setup that was used for the measurement of spatial coherence. Lens L_1 is at distance f from the mirror M_1, executing the inversion of the beam. Mirror M_2 is placed on a translation stage. The resulting interference is imaged into a digital camera. Inset show transverse profiles of the beam before and after the the mirror M_1, and displays the inversion of the beam in both x and y axes.

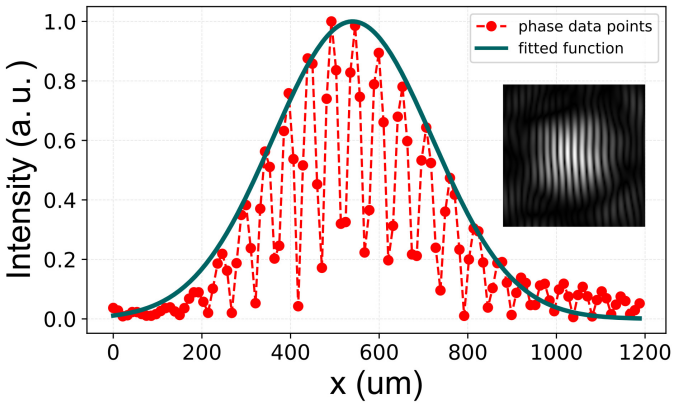

Figure 4.7: Typical measurement of Spatial coherence. Note that the oscillations in the intensity are a result of interference and are periodic to λ optical path difference. While the envelope is related to the spatial coherence and refers to the physical beam dimensions. (inset: filtered experimental image) .

4.2.2 Propagation of partially coherent 2D Airy beams

As we have already discussed Airy beams rely on interference effects so we expect that coherence will have a strong impact on their propagation dynamics. Interestingly, as we are going to show the degree of spatial coherence does not affect their parabolic trajectory.

In Fig. 4.9 normalized transverse $x-y$ intensity profiles of 2D Airy beams with variable spatial coherence are depicted. It is clear that when the spatial coherence decreases the intensity distribution of 2D Airy beams becomes blurred meanwhile the characteristic Airy oscillatory intensity pattern is lost for spatial coherence length $d_{12} < 500\mu m$.

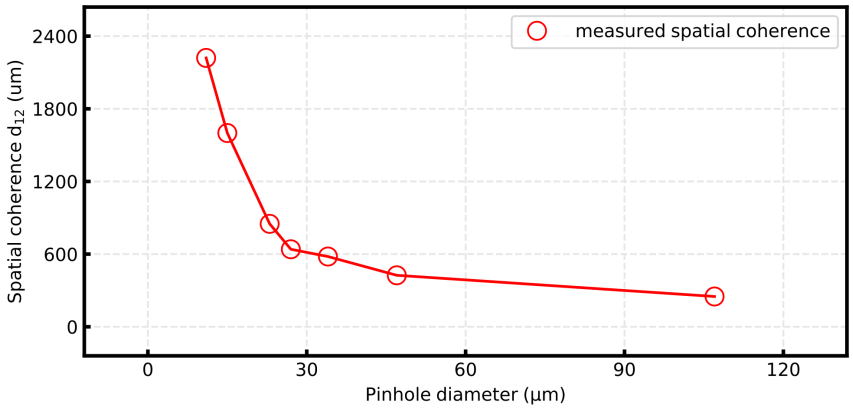

Figure 4.8: Spatial coherence length d_{12} as a function of pinhole diameter.

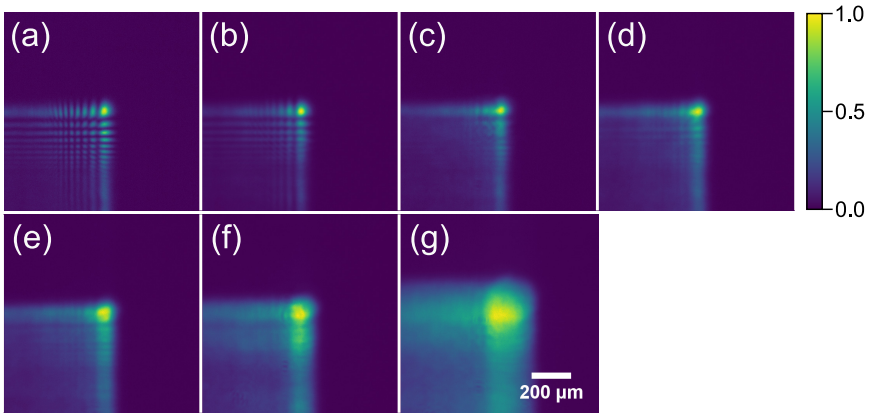

Figure 4.9: Normalized transverse $x-y$ intensity profiles of 2D Airy beams with variable spatial coherence. The corresponding values spatial coherence d_{12} are (a) $2200\mu m$, (b) $1600\mu m$, (c) $850\mu m$, (d) $640\mu m$, (e) $580\mu m$, (f) $425\mu m$, (g) $250\mu m$.

In Tab. 4.1 we summarize the values of spatial coherence, and its corresponding acceleration coefficients along with the main lobe width of the resulting accelerating beam.

Moreover, from Fig. 4.9 we can also observe that the size of the main intensity lobe of the 2D Airy beam is increasing as the spatial coherence decreases. This effect can become more clear in Fig. 4.10(a) where the intensity profiles of 2D Airy beams with different spatial coherence are plotted. In addition in Fig. 4.10(b) the corresponding FWHM of the main lobe as a function of spatial coherence is depicted.

On the other hand, although their transverse distributions are strikingly different the trajectories of the main intensity lobe are not affected by the

Table 4.1: spatial coherence and its corresponding acceleration coefficients with respect to pinhole diameter.

Pinhole Diameter (μm)	Spatial Coherence d_{12} (μm)	Main lobe width (FWHM) (μm)	Acceleration Coefficient c_a ($10^{-4} mm^{-1}$)
11	2200	32	1.15
15	1600	34	1.20
23	850	49	1.17
27	640	64	1.09
34	580	74	1.17
47	425	115	1.19
107	250	185	1.25

spatial coherence of the illuminating beam, as shown in Fig. 4.11. Note that in all cases the accelerating beams were generated using the reflective phase modulation device. Likewise, as we can observe the trajectory of the 2D Airy beams remains parabolic, with the same curvature, regardless of the spatial coherence of the illuminating beam. This interesting behaviour can be explained if we describe the propagation of an Airy beam using caustics of rays. This approach ignores the wave nature of these beams describing the propagation dynamics as a directed flow of energy. Likewise, interference effects that result in the characteristic Airy oscillatory intensity pattern, are also ignored. In this perspective, the caustic description is in principle an incoherent approach. In more detail, the phase distribution of an Airy beam can be well approximated [35] by $\Phi(x) = cx^{3/2}$, where c is a constant. The light rays, which are normal to the Airy wavefront, will form a caustic with a trajectory described by $x = c_a z^2$, where c_a is an acceleration coefficient. Clearly the rays form a caustic that describes a parabolic trajectory. Likewise, the incoming beam is modulated so that a cubic phase is imprinted, irrespectively from the spatial coherence. Therefore, the resulting caustics will be identical.

4.2.3 Self-healing properties of partially coherent 2D Airy beams

Another extraordinary property of coherence accelerating Airy beams is that they have the ability to self-heal [65]. Their intensity distribution is recovered after being partially blocked by an opaque obstacle. Here we show, for the first time to our knowledge, that partially coherent 2D Airy beams also exhibit this property.

In order to experimentally study the self-healing properties of such beams we used the phase modulation mirror device presented in Fig. 4.5. We then placed an opaque object with sharp edges, referred to as obstacle, at the

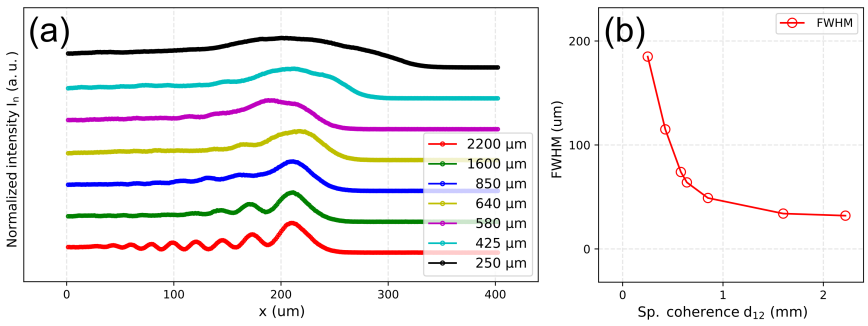

Figure 4.10: Plots of (a) normalized maximum intensity profile of 2D Airy beams with different degree of spatial coherence and (b) the corresponding FWHM of the main lobe as a function of spatial coherence.

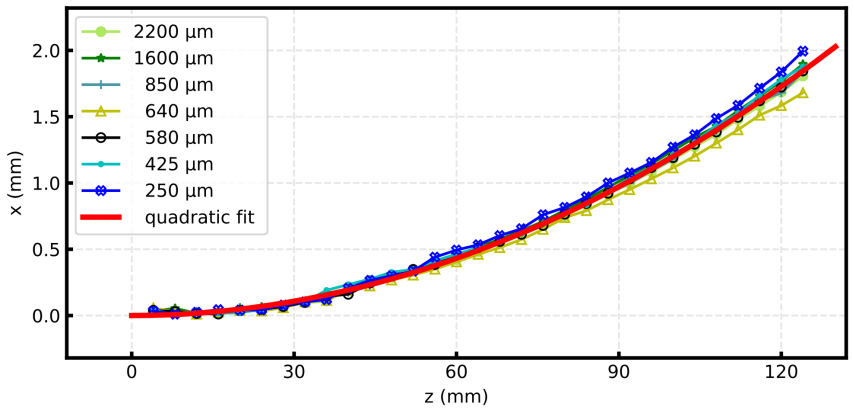

Figure 4.11: Trajectories of the main intensity lobe of 2D Airy beams of different degrees of spatial coherence d_{12} from $250\mu m$ to $2200\mu m$. Red line denotes a parabolic fit on Airy with $d_{12} = 580$ μm.

initial plane of the beam ($z = 0$), i.e. the Fourier plane of the focusing lens. Using a digital camera equipped with a telecentric imaging system, we monitored the position of the obstacle. Using an $x - y - z$ stage we placed the obstacle in such a way so that it blocked the primary intensity lobe of the 2D-Airy beam, this procedure is depicted in Fig. 4.12. As shown in Fig. 4.13, the obstacle lies in the upper right corner of the distribution, and thus selectively blocks only the high intensity lobe.

As shown in Fig. 4.13, for the case of a spatial coherence length $d_{12} =$

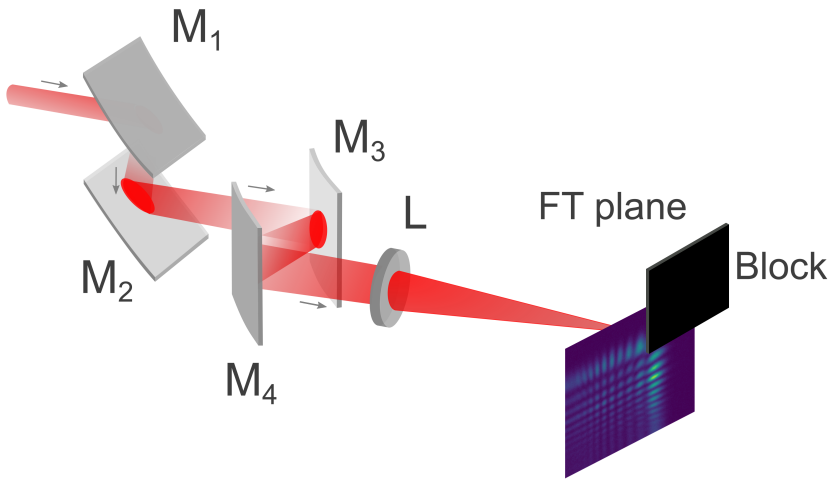

Figure 4.12: Graphical representation of the setup used to block the main lobe of the accelerating beam in order to study the self-healing properties of partially coherent accelerating beams.

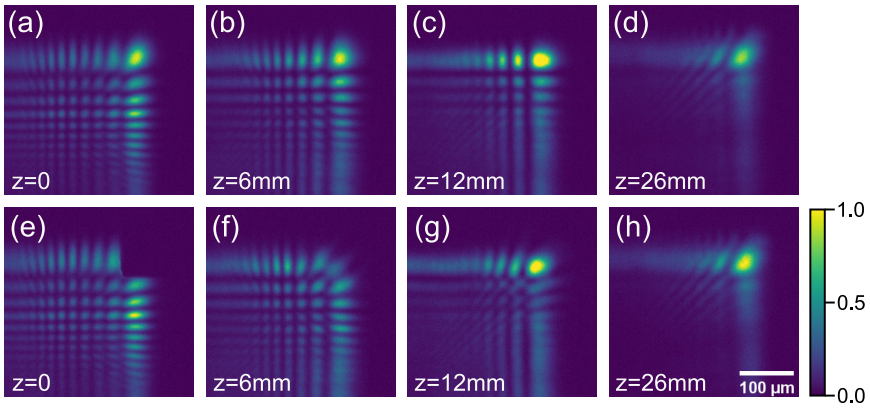

Figure 4.13: Normalized transverse $x-y$ intensity profile of a partially coherent 2D Airy beam (a)-(d) unblocked reference beam and (e)-(h) with a block clipping the main lobe the beam. (In all cases the measured spatial coherence length was $d_{12} = 2200$ μm)

2200 μm, the block initially perturbs the beam by eliminating the primary lobe. As the beam propagates the beam starts to self heal. Compared with the case of undisturbed propagation, shown in the upper row of Fig. 4.13, the primary lobe is fully recovered after ~ 26 mm of propagation. Interestingly, taking into account the primary lobe size w and defining an equivalent Rayleigh length of $z_{Ai} = \frac{\pi w^2}{\lambda}$ we get that $z_{Ai} \simeq 5$ mm, thus when perturbed by an obstacle of size $\sim w$ the beam self heals after a propagation distance of $\sim 5 z_{Ai}$.

Counterintuitively, this is also the case for an accelerating beam with low degree of spatial coherence. In the upper row of the Fig. 4.14 are shown the normalized transverse $x-y$ intensity profiles of an unblocked partially coherent 2D Airy beam with $d_{12} = 250$ μm, while in the bottom row of the Fig. 4.14 we see the same accelerating beam. but in this case we have blocked its main intensity lobe. As we can observe the primary lobe is fully recovered after ~ 26 mm of propagation, even for the case of low degree of spatial coherence.

The spatial coherence length d_{12} of the illuminating beam can vary by roughly one order of magnitude 250 μm $\leq$ d$_{12}$ $\leq$ 2200 μm, as shown in Tab. 4.1. Comparing this with the primary lobe FWHM size $w_0 \simeq 45$ μm of the generated 2D-Airy beam under coherent conditions we observe that in all cases $d_{12} > w_0$.

A quantitative metric of the beam recovery is evolution of the peak intensity I'_{max} of the perturbed beam, compared to the peak intensity I_{max} of the unperturbed one. As we can observe from the evolution of the ratio I'_{max}/I_{max} that is shown in Fig. 4.15, for all degrees of spatial coherence the produced accelerating beams are fully reconstructed after free propagation.

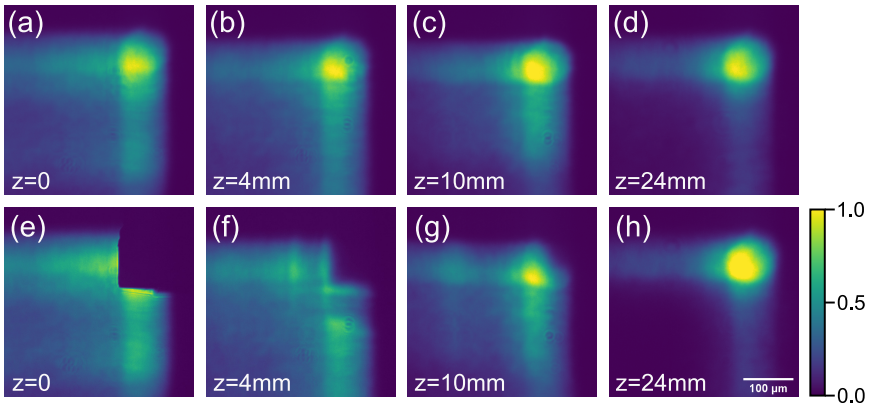

Figure 4.14: Normalized transverse $x-y$ intensity profile of a partially coherent 2D Airy beam (a)-(d) unblocked reference beam and (e)-(h) with a block clipping the main lobe the beam. (In all cases the measured spatial coherence length was $d_{12} = 250$ μm)

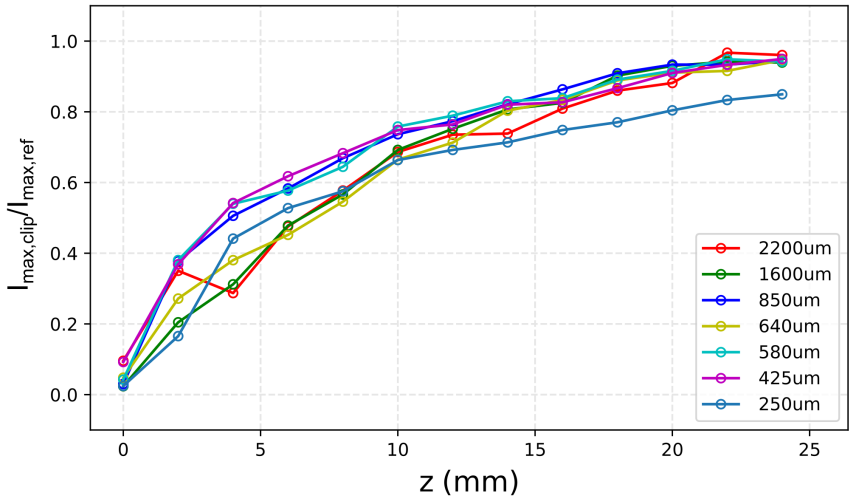

Figure 4.15: Maximum intensity ratio of clipped 2D Airy beams of variable spatial coherence with an unblocked reference beam, as a function of the propagation distance.

Likewise, their maximum intensity is recovered almost up to 95%.

4.3 Ultra-intense Airy Beams generate curved plasma for THz applications

As a clear demonstration of the capability of our setup to generate besides broadband, intense 2D Airy beams, we utilized it to generate such beams

using as a source high power femtosecond fs laser pulses. We utilized this intense curved plasma to generate THz waves through the two-color filamentation approach. This technique is one of the most convenient and efficient sources of pulsed ultra-broadband terahertz (THz) waves [127, 128]. In this process a beam and its second harmonic is combined in order to create a two color plasma filament that by ionizing the air leads to the emotion of THz. The setup for the generation of intense 2D Airy beams is shown in Fig. 4.16. In our experiments we used a Ti:sapphire laser source which provides 35 fs (FWHM) laser pulses, at a repetition rate of 1 kHz and a central wavelength $\lambda = 800$ nm. Using intense pulses with energy up to 1.11 mJ, ($\sim$ 32 GW peak power) to illuminate our setup we were able to deliver 0.73 mJ ($\sim$ 2 GW peak power) for the generation of the 2D Airy beams. This rather low efficiency of 66% is mainly due to beam clipping resulting from the mirror finite size, and their non optimized mirror reflectivity for this spectral range, which is $R \sim 95\%$. Besides these losses and taking into account the primary lobe size and the intensity distribution of Airy beams, we estimate that the peak intensity of the primary lobe is in the order of ~ 0.3 TW/cm^2. This ultra-high intensity is sufficient to excite electrons, through multiphoton ionization [66], in air and thus generate a plasma filament that will follow the parabolic trajectory of the beam.

Moreover, the intensity of our generated 2D Airy beams allowed us to generate it's second harmonic. By adding a non-linear type-I BBO crystal, after the lens that performs the Fourier Transform, along with the (ω) 2D Airy beam, a co-propagating 2^{nd} harmonic (2ω) was generated. As described

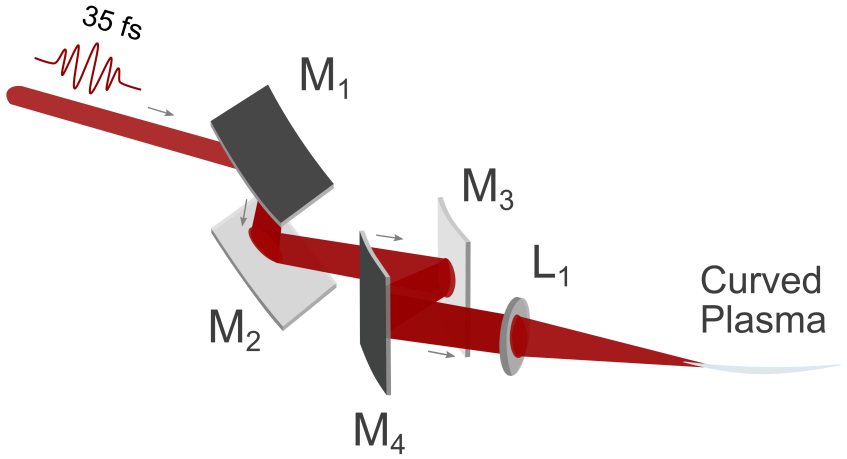

Figure 4.16: Illustration of the experimental setup we used for the generation of a curved plasma. L_1 lens with focal length $f = 100$ mm. Pulse duration 35 fs (FWHM), central wavelength $\lambda = 800$ nm, repetition rate of 1 kHz, and input pulse energy 1.11 mJ.

in detail by Koulouklidis et al. [23] the Airy beam imparts its properties to the 2^{nd} harmonic. Interestingly, the generated ω and the 2ω 2D Airy beams co-propagate following the same parabolic trajectory. This allows them to interact over a long propagation distance, an important property, which we have exploited to generate THz waves induced from 2-color filaments in air.

A side-view fluorescence image of generated plasma channel is depicted Fig. 4.17(a). We can clearly observe that the plasma is curved and that it consists of two distinct intense regions, one short in length (part 1) and one longer (part 2). As we see in Fig. 4.18(a) the transverse distribution of the generated THz waves consists of two doughnut shaped regions, that thy are produced of the two distinct parts of the plasma. To prove our assumption we have isolated each intense region of the plasma and observed the corresponding THz profile. In Fig. 4.18(b) we observe the corresponding THz profile that is generated form the part 1 of the plasma while in Fig. 4.18(c) the THz profile form the second part of the plasma.

Clipping part of the beam right after the focusing lens L_1 we can shape the plasma accordingly, namely it is possible to direct energy either to part 1 of the plasma when the upper part of the beam is clipped or the part 2 of the plasma when the lower part of the beam is clipped, as Figs. 4.17(b),(c) depict.

To isolate part 1 or part 2 of the curved plasma we use a simple but effective approach that is illustrated in Fig. 4.19. A knife-edge, placed after the FT lens, is used to block different parts of the beam. In more detail, as shown in Fig. 4.19(a), clipping the upper part of the beam isolates plasma part 1. On the other hand,as shown in Fig. 4.19(b) when the lower part of the beam is blocked, plasma part 2 is isolated.

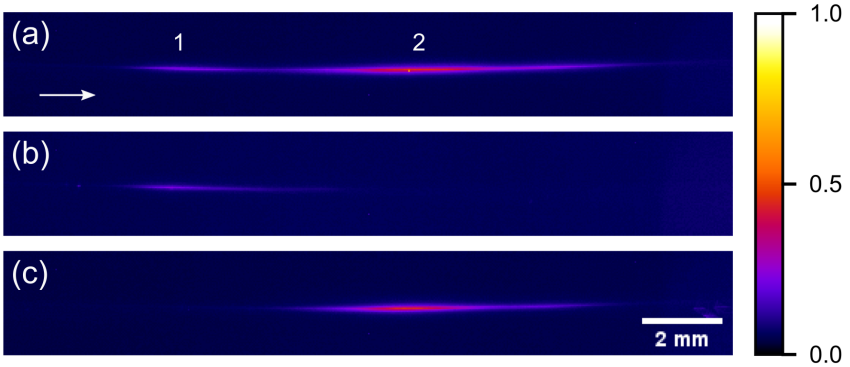

Figure 4.17: Side-view fluorescence image of generated plasma channel (a) whole plasma (b) part 1 of the plasma when the upper part of the beam is clipped, and (c) part 2 of the plasma when the lower part of the beam is clipped.

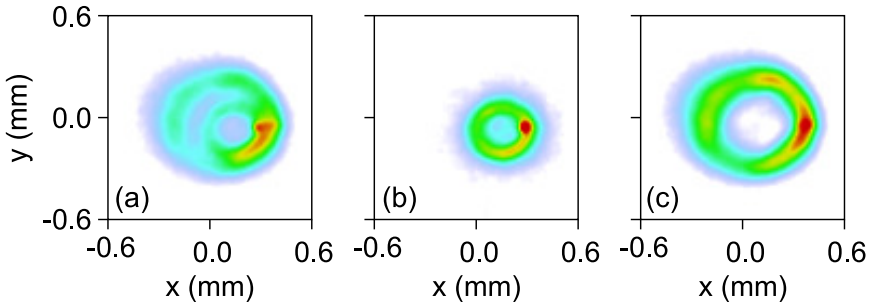

Figure 4.18: Transverse THz profiles, generated from (a) the whole curved plasma, (b) from part 1 of the plasma, and (c) from part 2 of the plasma.

4.4 Generation of spiraling light: Tornado Waves

Structured light, as we often describe the generation of custom light fields, is a topic of wide interest in optics. Structuring can involve, independently or in combination, the spatial modulation of phase, amplitude, and polarization [6] of a light wave. Such fields can provide a significant advantage compared to non-structured light, especially in applications where light is used as means of energy delivery on a target. Controlling of the intensity distribution and the shape of the focus as the input power is increased is a challenge for applications like direct laser writing, non-linear wave mixing and harmonics generation, and high power THz generation. For example, higher powers ignite nonlinear propagation effects that dynamically reshape the light beam [66]. The use of structured light can in principle enable us to control the intensity distribution and the focus position in the linear and the non-linear propagation regimes. To address this open problem a plethora of variations of structured light have been introduced, dramatically extending

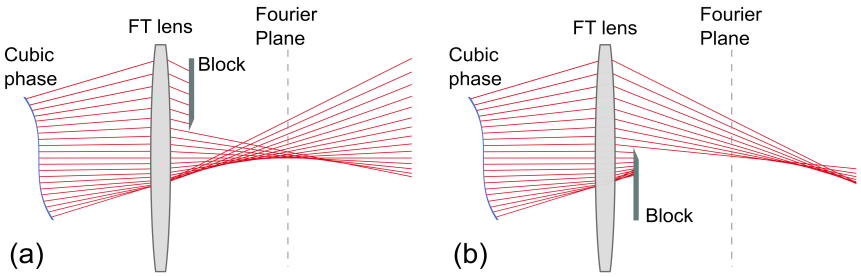

Figure 4.19: Illustration of the method we used to isolated different parts of the plasma by clipping the corresponding parts of the beam (a) clipping the upper part of the beam results into the isolation of the part 1 of the plasma and (b) clipping the lower part of the beam results into the isolation of the part 2 of the plasma .

a collection containing only the, classical now, Bessel beams [129]. The appearance of spatial light modulation devices (SLM) have made it possible to generate a wide range of structured light variations, optimized using various approaches. Besides trial and error numerical approaches some basic design guidelines have emerged that allow us to design the focal distribution. A key element of this approach is the use of stationary, non-diffracting light like Bessel [129] and Airy beams [24]. The propagation of such light is dominated by a strong linear energy flux that through interference generates the high intensity features of the beam. As the power is increased, nonlinear effects are exited only locally at the high intensity regions, making it possible to tailor the propagation dynamics. In this context, an ideal template for this tailored control is the recently introduced family of rotationally symmetric accelerating beams, often referred as circular Airy beams (CAB) or ring-Airy beams, whose radial distribution is described by the Airy function [26, 42]. These waves propagate in curved trajectories, and exhibit abrupt autofocus, while at high intensities they reshape into nonlinear intense light-bullets with extremely well defined focal position [29]. Interestingly, by imprinting a helical phase, shaping can induce topological charge to the wave, often referred to as optical vortex. Such waves carry orbital angular momentum (OAM) and exhibit a rotating phase structure as they propagate [6]. Twisting structured light, where the intensity pattern rotates forming a helical pattern, can be generated by superimposing structured light that caries (OAM) of opposite helicity [130, 131, 6]. Furthermore, by properly tuning the interfering (OAM) carrying waves, this twisting can occur inward and angularly accelerating, or decelerating, fashion forming a helix of variable pitch as light propagates [132, 133]. Recently, Tornado waves (ToWs) [101], a new type of structured light that combines the radial acceleration with the angular acceleration was theoretically introduced. Like a tornado, ToWs intensity maxima outline a spiral of decreasing radius and pitch as they propagate. In this thesis we experimentally realize, for the first time to our knowledge, Tornado Waves and demonstrate their unique property to twist and accelerate both over the radial and the angular direction. Using a novel experimental approach, which involves spatial multiplexing, we generate such complex interfering fields using a single phase mask imprinted onto a SLM. this technique is described in more detail in 3.4.1. Furthermore, we explore various approaches to create dynamic ToWs that also rotate in time, and focus our study on two color ToWs which exhibit rotational frequencies in the THz regime.

The propagation of such beams is described by the paraxial wave equation [101, 42]:

$$\nabla_{\perp}^{2} u + 2ik\frac{\partial u}{\partial z} = 0 \tag{4.6}$$

where $\nabla_{\perp}^{2}$ denotes the transverse part of the Laplacian, z the propagation distance and u the electric field envelope.

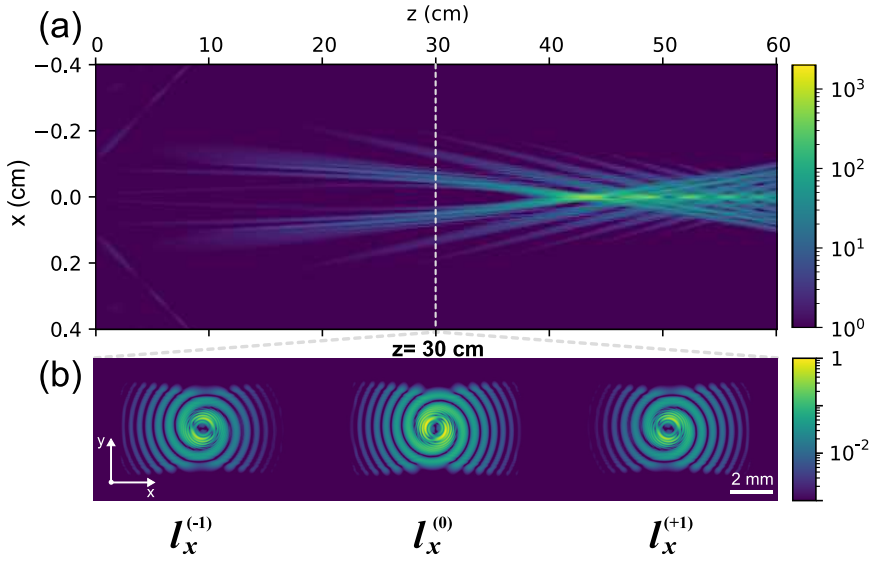

Figure 4.20: Simulation of the propagation of Tornado waves (a) x-z Intensity profile distribution. Note the diagonal stripes that represent the diffracted orders and (b) x-y Intensity profile (normalized to peak value) at $z = 30$cm. The ± 1 diffraction orders are clearly separated from the zero order

In order to investigate the validity of our approach for generating ToWs we performed numerical simulations of Eq. (4.6). In our simulations we considered a linearly polarized Gaussian beam along the **y** direction that illuminates the phase mask which is shown in Fig. 3.17. The intensity profile along propagation direction is presented in Fig. 4.20(a). The abruptly autofocusing characteristics are clearly reproduced.

The diagonal stripes appearing in this $x - z$ section are due to the presence of the diffracted orders. A clear demonstration of the effectiveness of the spatial multiplexing approach is shown in Fig. 4.20b where an $x - y$ intensity profile at $z = 30$ cm is depicted. The Gaussian intensity profile of the propagating beam has already been transformed to a vortex shape, characteristic of ToW's [101]. Furthermore, besides the zero order, two replicas representing the ± 1 diffraction orders are clearly visible. As expected the

Table 4.2: Design parameters for the generation of ToWs.
(f refers to predicted values)

	r_0 (μm)	C $(m^{-1/2})$	l	f (mm)	λ (nm)
Φ_A	800	0.089	+1,2	424	594
Φ_B	1000	0.100	-1,-2	422	594

± 1 diffraction orders, due to their angular separation, are spatially separated from the zero order and do not affect the central foci distribution.

For the generation of Tornado waves we use a simple experimental setup as shown in figure 4.21. A CW laser beam of Gaussian profile and wavelength $\lambda = 594$ nm polarized in $\mathbf{x}$ direction in order to match the polarization plane of the SLM that is in the horizontal plane, is expanded by a factor of 2 by lenses L_1, L_2, reaching a $FWHM = 8.9$ mm and then illuminates the phase mask, depicted in Fig. 3.17 imprinted on a reflective phase SLM (HOLOEYE-PLUTO 0.7" HDTV) with 8 μm pixel and resolution 1920x1080 pixels. The modulated beam is then directed using reflecting mirrors M_1, M_2 towards a 1280x1024 pixels 8bit digital camera. In order to record the transverse intensity profile $I(x, y)$ of the modulated beam along propagation, the camera is translated along the z axis. Meanwhile, the diffraction orders that are produced as a side effect of the multiplexed phase mask, depicted in Fig. 4.20, are not imaged by the camera sensor due to their large spatial separation from the zero order. The angular separation of the orders is affected by the SLM pixel size as described in Eq. (3.10) and depicted in Fig. 3.16.

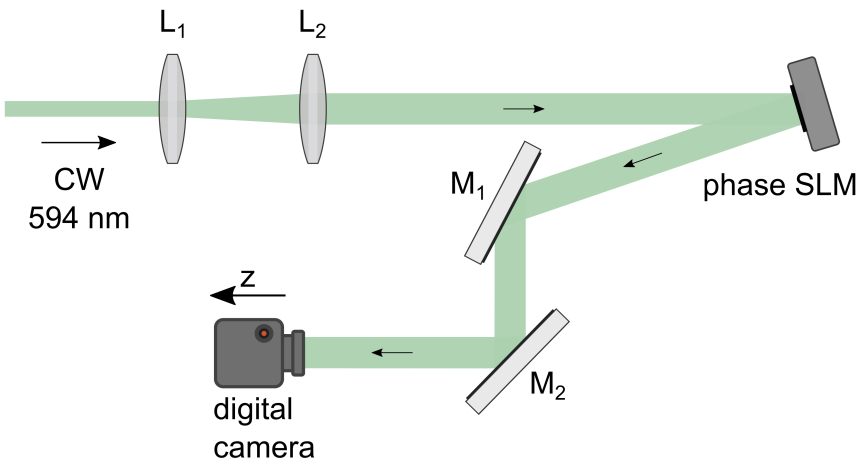

Figure 4.21: Experimental setup for the generation of Tornado waves. Lenses L_1, L_2 comprise a 2x beam expander.

4.4.1 Observation of Tornado waves

Using the experimental setup depicted in Fig. 4.21 and applying the multiplexing technique we generated ToWs by superimposing accelerating waves carrying OAM using the design parameters presented in Tab. 4.2. The number of twisting intensity lobes appearing in the transverse $I(x, y)$ intensity profile depend [101] on the topological charges $N = |m_A| + |m_B|$. In our experiments we used 3 combinations of topological charge: $(m_A = 1, m_B =$

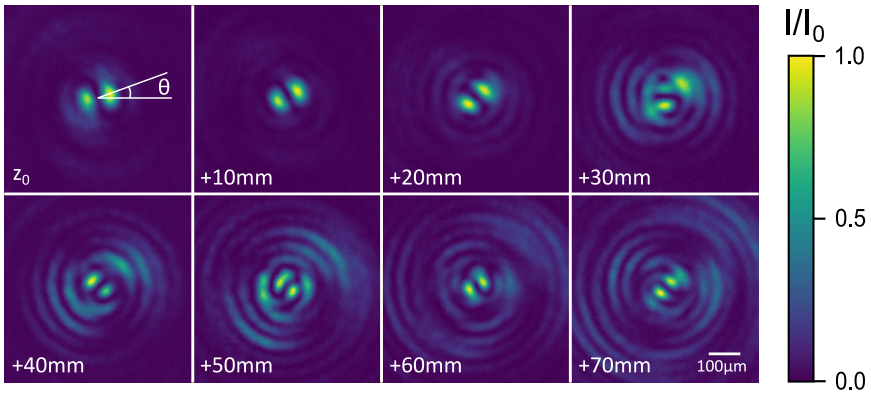

Figure 4.22: Normalized transverse x-y intensity sections of tornado waves with 2 lobes, $m_A = 1$, $m_B = -1$, along propagation.

-1), $(m_A = 1, m_B = -2)$, $(m_A = 2, m_B = -2)$ resulting respectively into 2, 3 and 4 twisting intensity lobes. The evolution of the cross sectional intensity $I(x, y)$ distribution as a ToW propagates along z is shown in Fig. 4.23. Starting from a reference point $z_0 = 414$ mm along the propagation we can observe that the intensity lobes rotate at a varying rate and a decreasing radius around z axis (located in the center of each image). This is a typical behavior of ToWs where light twists and accelerates both in the angular and in the radial dimension [101].The $I(x, y)$ intensity pattern becomes more complex as the number of lobes N is increased [101].In all cases the high intensity lobes rotate at a varying rate and a decreasing radius around z axis, although, as we observe by comparing Fig. 4.23a to 4.23b and 4.23c, this becomes less profound as the number of lobes is increasing. In order to evaluate the accelerating characteristics of these ToWs we retrieved and analysed the $I(x, y)$ cross sectional images. By monitoring the radial and angular position of each twisting intensity lobe we were able to track their trajectories. In Fig. 4.24(a) we depict the evolution of the angular orientation θ of the two lobes (see Fig. 4.23a) and the normalized peak intensity as a function of the propagation distance. The angle θ increases at a varying rate as indicated from its oscillatory behaviour. From these measured values we can estimate the angular velocity $v \equiv \dot{\theta}(z)$ and the angular acceleration $\gamma \equiv \ddot{\theta}(z)$ that are depicted in Fig. 4.24b,c respectively. The vertical gray shaded areas highlight the zones where we observe angular acceleration. We observe a typical ToW behaviour, where the angular velocity v varies in a quasi-periodic fashion between 0 and ~ 10 deg/mm. These areas are related to angular acceleration, where γ takes values between $\sim \pm 1$ deg/mm^2 as one can observe in Fig. 4.24c. The estimated angular acceleration values are in good agreement with the values theoretically predicted [101] for ToWs in this range of autofocusing values. Furthermore, the maximal angular acceleration is observed when the peak intensity of the rotating lobes decreasing

Table 4.3: Peak values for angular velocity and acceleration for various topological charge combinations

m_A	m_B	v_{max} (deg/mm)	γ_{max} (deg/mm^2)
+1	-1	10.3 ± 1.4	1.2 ± 0.4
+1	-2	5.0 ± 0.7	0.5 ± 0.2
+2	-2	4.0 ± 0.8	0.4 ± 0.2

as we can observe by comparing to the peak intensity distribution shown Fig. 4.24a.

Following a similar procedure to Fig. 4.24 we analysed the $I(x, y)$ cross sectional images to retrieve the radial and angular position of the twisting intensity lobes, and estimate their angular velocity and acceleration. A visualization of the trajectory of the high intensity lobes is shown in Fig. 4.25 while an overview of the peak values of the angular velocity v and angular acceleration γ is given in Tab. 4.3. Both the peak intensity and the peak values for v_{max}, γ_{max} decrease as the the number of lobes N is increased. The drop in the peak intensity is a result of distributing the beam energy in the ToW funnel [101] to an increasing number of lobes.

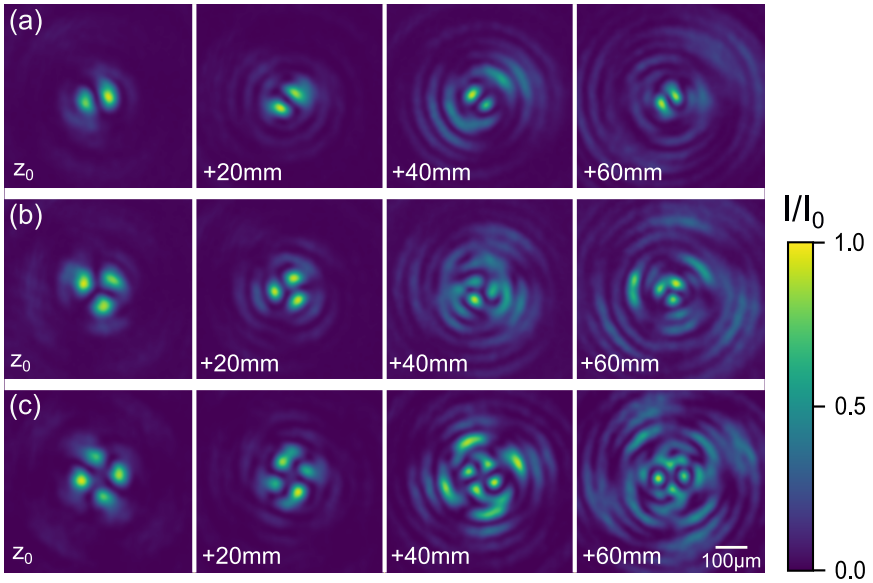

Figure 4.23: Normalized transverse x-y intensity sections of tornado waves with 2, 3, and 4 lobes respectively (a) $m_A = 1$, $m_B = -1$, (b) $m_A = 1$, $m_B = -2$, (c) $m_A = 2$, $m_B = -2$.

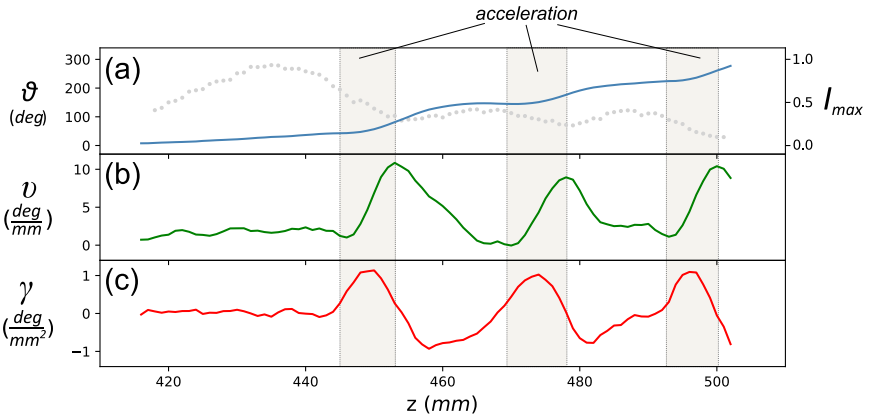

Figure 4.24: Evolution of the two lobes of Tornado waves with $m_A = 1, m_B = -1$, along propagation. (a) angle θ (cyan line) and normalized maximum peak intensity (grey dotted line), (b) angular velocity v, and (c) angular acceleration γ.

Tornado waves in the temporal domain

We believe that the efficient generation of such complex superimposed fields that carry orbital angular momentum of opposite handedness using a single phase modulation device is a milestone for using such waves in applications. In the work where this wave first introduced [101] it have been revealed that simple scaling laws apply to the angular velocity v and acceleration γ of any twisting light structure as we scale it's spatial dimensions. Here we extend this analysis to the effect of the number of lobes and demonstrate that it is possible to generate dynamically twisting light that rotates at an angular frequency ω_r around z axis, by using two different colors. Using a generic description of two superimposing OAM carrying waves of different frequency

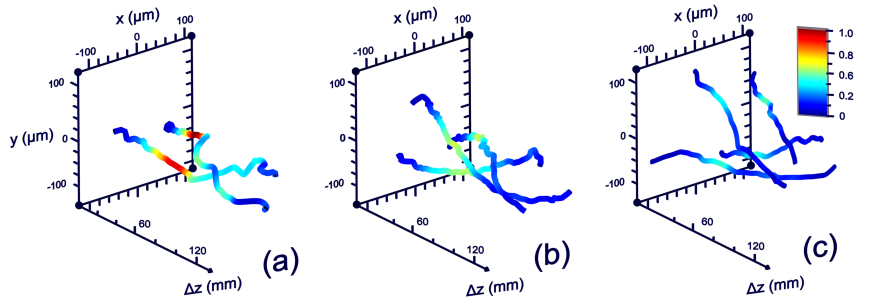

Figure 4.25: Visualization of the trajectory of high intensity lobes for Tornado waves with (a) $m_A = 1, m_B = -1$, (b) $m_A = 1, m_B = -2$, (c) $m_A = 2, m_B = -2$.

$(\omega_A,\ \omega_B)$, and respectively of different wavelength $(\lambda_A,\ \lambda_B)$ can be described as:

$$\begin{aligned} u_s(\mathbf{r},t) = & u_A(\mathbf{r};\lambda_A)e^{i[\varphi_A(\mathbf{r};\lambda_A)+\psi_A(\theta)-\omega_A t]} \\ & +u_B(\mathbf{r};\lambda_B)e^{i[\varphi_B(\mathbf{r};\lambda_B)+\psi_B(\theta)-\omega_B t]} \end{aligned}$$

where $\varphi_i(\mathbf{r};\lambda_A)$ refers to the spatial phase, $\psi_i(\theta) = m_i\theta$ is the azimuthal phase (vortex) and m_i is the topological charge. It is straightforward to show that this superposition will result to an intensity profile that will twist in space with an angular velocity

$$\upsilon = \frac{1}{N}\frac{\partial\Delta\varphi}{\partial z} \tag{4.7}$$

and angular acceleration of:

$$\gamma = \frac{1}{N}\frac{\partial^2\Delta\varphi}{\partial z^2} \tag{4.8}$$

where $N = |m_A| + |m_B|$ is the number of high intensity lobes, and $\Delta\varphi \equiv \varphi_A - \varphi_B$ is the spatial phase difference. Clearly, increasing the complexity of the wave by increasing the topological charge results in decreasing the angular velocity and acceleration.

Furthermore, these two color twisting light structures will dynamically rotate around z axis with a temporal frequency f_r, or a temporal period $T_r = 1/f_r$:

$$\begin{aligned} f_r =& \frac{1}{N}f_0 = \frac{c}{N}\frac{\Delta\lambda}{\lambda_A^2}\left(1+\frac{\Delta\lambda}{\lambda_A}\right)^{-1} \\ T_r =& N\ T_0 = \frac{N}{c}\frac{\lambda_A^2}{\Delta\lambda}\left(1+\frac{\Delta\lambda}{\lambda_A}\right) \end{aligned} \tag{4.9}$$

where $f_0 = (\omega_A - \omega_B)/2\pi$, $T_0 = 1/f_0$ are respectively a reference beat frequency and period [134], and $\Delta\lambda = \lambda_B - \lambda_A$. Clearly, the period for a full rotation of the N high intensity lobe pattern is proportional to the number of lobes. In principle, due to symmetry these high intensity lobes are identical and they are angularly distributed at $2\pi/N$ intervals, so as they rotate they will periodically overlap at a period T_o. Of course any break of the perfect symmetry, a common situation in experiments, would lead to a variation of the intensity between the lobes.

In order to demonstrate the viability of this approach in generating dynamically twisting light structures we have performed numerical simulations with two-color ToWs. Using the ToW parameters of Tab. 4.2 and $\lambda_A = 594$ nm, $\Delta\lambda = 20$ nm we have studied the temporal evolution of a two-color ToW for the case of two ($N = 2$, $m_{A,B} = \pm 1$) and three ($N = 3$, $m_{A,B} = +1, -2$) high intensity lobes. The reference period is in this case ($T_o \sim 61$ fs). A visualization of the evolution of the ToW peaks as a function of time is shown in Fig. 4.26. The $I(x, y, z_o, t)$ intensity cross

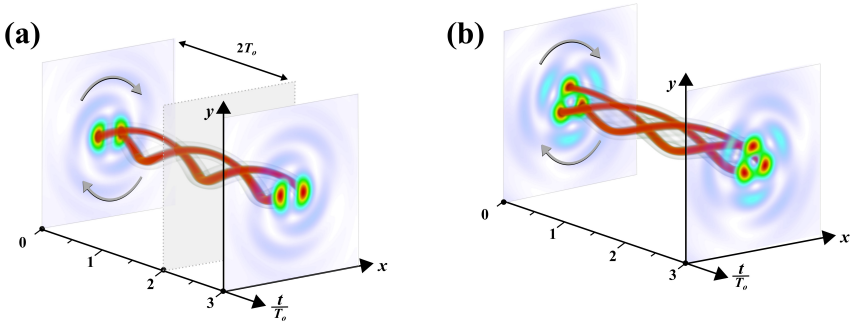

Figure 4.26: Numerical simulation results visualizing the rapid rotation of high intensity lobes in a two color Tornado wave (a) for the case of $N = 2$ and (b) $N = 3$ high intensity lobes. ($T_o \sim 109$ fs).

section is retrieved at the autofocus position $z_o = 42$ cm of the two color ToW. As predicted by Eq. 4.9 the high intensity lobes perform a full rotation in $2T_o \sim 122$ fs for $N = 2$ and in $3T_o \sim 182$ fs for $N = 3$. Such structured light, that rotates rapidly within the pulse duration, can be quite appealing in direct laser writing applications.

Conclusions

In this Thesis, we have studied the properties of the focal region of abruptly autofocusing ring-Airy, and their variants autodefocusing inverse ring-Airy beams, under the action of a conical phase gradient. Exploiting the similarities between the propagation of 1D Airy beams and radially symmetric Airy beams, we present analytic approximations for the position, length and width of the focus, using a unified formulation for both beam types. Our results enable the tailoring of the focal region of such abruptly autofocusing and autodefocusing beams by simply tuning the dimensions of the initial primary ring and the conical angle. Furthermore, We have confirmed the validity of our analytical results by numerical simulations over a broad parameters range. We expect that our results will have a significant impact to applications that exploit the unique properties of radially symmetric Airy beams like for instance, materials processing, optical trapping, and deposition of high-laser powers at remote locations.

In addition, we presented a new method for the generation of a double foci feature along propagation, by superimposing two radially symmetric Airy beams with a presence of a conical phase, where the two distinct foci are independently controllable. Moreover, using this technique the produced feature exhibits a remarkable property where its second focus remains unaffected even if the first one is completely blocked. Furthermore, we showed that using this approach enables us to create a single focus with ultra high peak intensity contrast. Therefore, we believe that these shaped accelerating beams constitute a new set of scalable tools, finding use in numerous laser applications, ranging from materials processing to particle manipulation.

Moreover, we have demonstrated that by exploiting optical aberrations a properly adjusted cylindrical mirror beam expander can effectively operate as a broadband, high power continuous phase mask. By correlating each of the Seidel wave aberrations to a specific power term, we have shown that smooth phase distributions can be generated using, an up to the forth power, polynomial approximation. Raytracing numerical simulations have confirmed the potential of the device to generate such phase distributions. Using a cascade of two orthogonally oriented phase masks we have generated accelerating white light Airy beams, that due to the specific spectral

properties of such devices, do not break up as they propagate. Furthermore, using this device we created accelerating beams with variable partial spatial coherence and studied their propagation dynamics in free space as well as their self-healing properties when a the main lobe of the beam is blocked. Finally, we also demonstrated the capability of our device to withstand high powers by creating intense curved plasma channels to generate THz waves.

Lastly, we have realized light spiraling like a tornado by superimposing abruptly auto-focusing waves, that carry OAM of opposite handedness, using a single spatially multiplexed phase modulating device. Furthermore, we have shown that by using a two-color scheme it is possible to generate dynamically twisting light that can rotate at ultrahigh angular frequencies $100\text{GHz} < \omega_\text{r} < 50\text{THz}$. These results may pave the way for various novel applications that rely on the spiralling behavior of ToWs, like direct laser writing, optical tweezers and nonlinear optics.

Bibliography

[1] John A Scales and Roel Snieder. What is a wave? Nature, 401(6755):739–740, oct 1999.

[2] Max Born and Emil Wolf. Principles of Optics. Pergamon Press, 4th edition, 1980.

[3] David J Griffiths. Introduction to electrodynamics. Prentice Hall New Jersey, 1962.

[4] Min Gu. Advanced optical imaging theory, volume 75. Springer Science & Business Media, 2000.

[5] Stefanos Trachanas. An introduction to quantum physics: a first course for physicists, chemists, materials scientists, and engineers. John Wiley & Sons, 2018.

[6] Halina Rubinsztein-Dunlop, Andrew Forbes, M V Berry, M R Dennis, and et al. Andrews. Roadmap on structured light. Journal of Optics, 19(1):013001, jan 2017.

[7] Eugene Hecht et al. Optics, volume 5. Addison Wesley San Francisco, 2002.

[8] Orazio Svelto and David C Hanna. Principles of lasers, volume 1. Springer, 2010.

[9] Guy Indebetouw. Nondiffracting optical fields: some remarks on their analysis and synthesis. JOSA A, 6(1):150–152, 1989.

[10] Dimitris G. Papazoglou. PyWp: A versatile wave propagator in Python, 2016.

[11] Hugo E Hernández-Figueroa, Michel Zamboni-Rached, and Erasmo Recami. Non-diffracting waves. John Wiley & Sons, 2013.

[12] J. Durnin. Exact solutions for nondiffracting beams I The scalar theory. Journal of the Optical Society of America A, 4(4):651, apr 1987.

[13] J. Durnin, J. J. Miceli, and J. H. Eberly. Diffraction-free beams. Physical Review Letters, 58(15):1499–1501, apr 1987.

[14] Nico M Temme. Special functions: An introduction to the classical functions of mathematical physics. John Wiley & Sons, 1996.

[15] John H. McLeod. The Axicon: A New Type of Optical Element. Journal of the Optical Society of America, 44(8):592, aug 1954.

[16] David McGloin and Kishan Dholakia. Bessel beams: diffraction in a new light. Contemporary Physics, 46(1):15–28, 2005.

[17] Narupon Chattrapiban, Elizabeth A Rogers, David Cofield, Wendell T Hill III, and Rajarshi Roy. Generation of nondiffracting bessel beams by use of a spatial light modulator. Optics letters, 28(22):2183–2185, 2003.

[18] Tomáš Čižmár and Kishan Dholakia. Tunable bessel light modes: engineering the axial propagation. Optics express, 17(18):15558–15570, 2009.

[19] Michael V Berry and Nandor L Balazs. Nonspreading wave packets. American Journal of Physics, 47(3):264–267, 1979.

[20] George Biddell Airy et al. On the intensity of light in the neighbourhood of a caustic. Transactions of the Cambridge Philosophical Society, 6:379, 1838.

[21] D. Hammer. Airy's theory of the rainbow. Journal of the Franklin Institute, 156(5):335–349, 1903.

[22] Milton Abramowitz and Irene A. Stegun. Handbook of mathematical functions. Dover Publications, 1970.

[23] Anastasios D. Koulouklidis, Dimitris G. Papazoglou, Vladimir Yu Fedorov, and Stelios Tzortzakis. Phase Memory Preserving Harmonics from Abruptly Autofocusing Beams. Phys. Rev. Lett., 119(22):223901, nov 2017.

[24] G. A. Siviloglou, J Broky, A. Dogariu, and D. N. Christodoulides. Observation of Accelerating Airy Beams. Physical Review Letters, 99(21):213901, nov 2007.

[25] D. G. Papazoglou, S. Suntsov, D. Abdollahpour, and S. Tzortzakis. Tunable intense Airy beams and tailored femtosecond laser filaments. Physical Review A - Atomic, Molecular, and Optical Physics, 81(6):061807, jun 2010.

[26] Nikolaos K Efremidis and Demetrios N Christodoulides. Abruptly autofocusing waves. Optics Letters, 35(23):4045–4047, 2010.

[27] Dimitris Mansour and Dimitris G Papazoglou. Tailoring the focal region of abruptly autofocusing and autodefocusing ring-airy beams. Osa Continuum, 1(1):104–115, 2018.

[28] Nan Li, Yunfeng Jiang, Kaikai Huang, and Xuanhui Lu. Abruptly autofocusing property of blocked circular airy beams. Optics express, 22(19):22847–22853, 2014.

[29] P Panagiotopoulos, D G Papazoglou, a Couairon, and S Tzortzakis. Sharply autofocused ring-Airy beams transforming into non-linear intense light bullets. Nature communications, 4(October):2622, 2013.

[30] Kang Liu, Anastasios D. Koulouklidis, Dimitrios G. Papazoglou, Stelios Tzortzakis, and Xi-Cheng Zhang. Enhanced terahertz wave emission from air-plasma tailored by abruptly autofocusing laser beams. Optica, 3(6):605, jun 2016.

[31] Maria Manousidaki, Dimitrios G. Papazoglou, Maria Farsari, and Stelios Tzortzakis. Abruptly autofocusing beams enable advanced multiscale photo-polymerization. Optica, 3(5):525, may 2016.

[32] KT Gahagan and GA Jr Swartzlander. Optical vortex trapping of particles. Optics Letters, 21(11):827–829, 1996.

[33] Alison M Yao and Miles J Padgett. Orbital angular momentum: origins, behavior and applications. Advances in Optics and Photonics, 3(2):161–204, 2011.

[34] Les Allen, Marco W Beijersbergen, RJC Spreeuw, and JP Woerdman. Orbital angular momentum of light and the transformation of laguerre-gaussian laser modes. Physical review A, 45(11):8185, 1992.

[35] Jeffrey A Davis, Don M Cottrell, and David Sand. Abruptly autofocusing vortex beams. Optics Express, 20(12):13302, jun 2012.

[36] Julio C Gutiérrez-Vega, MD Iturbe-Castillo, and S Chávez-Cerda. Alternative formulation for invariant optical fields: Mathieu beams. Optics letters, 25(20):1493–1495, 2000.

[37] JC Gutiérrez-Vega, MD Iturbe-Castillo, GA Ramırez, E Tepichın, RM Rodrıguez-Dagnino, S Chávez-Cerda, and GHC New. Experimental demonstration of optical mathieu beams. Optics Communications, 195(1-4):35–40, 2001.

[38] C Alpmann, R Bowman, M Woerdemann, M Padgett, and C Denz. Mathieu beams as versatile light moulds for 3d micro particle assemblies. Optics express, 18(25):26084–26091, 2010.

[39] Chaowei Wang, Liang Yang, Yanlei Hu, Shenglong Rao, Yulong Wang, Deng Pan, Shengyun Ji, Chenchu Zhang, Yahui Su, Wulin Zhu, et al. Femtosecond mathieu beams for rapid controllable fabrication of complex microcages and application in trapping microobjects. ACS nano, 13(4):4667–4676, 2019.

[40] James D. Ring, Jari Lindberg, Areti Mourka, Michael Mazilu, Kishan Dholakia, and Mark R. Dennis. Auto-focusing and self-healing of pearcey beams. Opt. Express, 20(17):18955–18966, Aug 2012.

[41] Xingyu Chen, Dongmei Deng, Jingli Zhuang, Xi Peng, Dongdong Li, Liping Zhang, Fang Zhao, Xiangbo Yang, Hongzhan Liu, and Guanghui Wang. Focusing properties of circle pearcey beams. Optics letters, 43(15):3626–3629, 2018.

[42] Dimitrios G Papazoglou, Nikolaos K. Efremidis, Demetrios N. Christodoulides, and Stelios Tzortzakis. Observation of abruptly autofocusing waves. Optics Letters, 36(10):1842, may 2011.

[43] Derek Albert Long. Raman spectroscopy. New York, pages 1–12, 1977.

[44] Richard L McCreery. Raman spectroscopy for chemical analysis, volume 225. John Wiley & Sons, 2005.

[45] David W Hahn and Nicoló Omenetto. Laser-induced breakdown spectroscopy (libs), part ii: review of instrumental and methodological approaches to material analysis and applications to different fields. Applied spectroscopy, 66(4):347–419, 2012.

[46] AS Woutersen, U Emmerichs, and HJ Bakker. Femtosecond mid-ir pump-probe spectroscopy of liquid water: Evidence for a two-component structure. Science, 278(5338):658–660, 1997.

[47] Michele Ortolani, Andrea Mancini, Arne Budweg, Denis Garoli, Daniele Brida, and Francesco de Angelis. Pump-probe spectroscopy study of ultrafast temperature dynamics in nanoporous gold. Physical Review B, 99(3):035435, 2019.

[48] F Courvoisier, P-A Lacourt, M Jacquot, MK Bhuyan, L Furfaro, and JM Dudley. Surface nanoprocessing with nondiffracting femtosecond bessel beams. Optics letters, 34(20):3163–3165, 2009.

[49] Tom Vettenburg, Heather I.C. Dalgarno, Jonathan Nylk, Clara Coll-Lladó, David E.K. Ferrier, Tomáš Čižmár, Frank J. Gunn-Moore, and

Kishan Dholakia. Light-sheet microscopy using an Airy beam. Nature Methods, 11(5):541–544, may 2014.

[50] Nadine Götte, Thomas Winkler, Tamara Meinl, Thomas Kusserow, Bastian Zielinski, Cristian Sarpe, Arne Senftleben, Hartmut Hillmer, and Thomas Baumert. Temporal airy pulses for controlled high aspect ratio nanomachining of dielectrics. Optica, 3(4):389–395, Apr 2016.

[51] Marti Duocastella and Craig B Arnold. Bessel and annular beams for materials processing. Laser & Photonics Reviews, 6(5):607–621, 2012.

[52] Zhi Wang, Lan Jiang, Xiaowei Li, Andong Wang, Zhulin Yao, Kaihu Zhang, and Yongfeng Lu. High-throughput microchannel fabrication in fused silica by temporally shaped femtosecond laser bessel-beam-assisted chemical etching. Optics letters, 43(1):98–101, 2018.

[53] Evangelos Skoulas, Alexandra Manousaki, Costas Fotakis, and Emmanuel Stratakis. Biomimetic surface structuring using cylindrical vector femtosecond laser beams. Scientific reports, 7(1):1–11, 2017.

[54] Rudolf Weber, Andreas Michalowski, Marwan Abdou-Ahmed, Volkher Onuseit, Volker Rominger, Martin Kraus, and Thomas Graf. Effects of radial and tangential polarization in laser material processing. Physics Procedia, 12:21–30, 2011.

[55] OJ Allegre, W Perrie, SP Edwardson, G Dearden, and KG Watkins. Laser microprocessing of steel with radially and azimuthally polarized femtosecond vortex pulses. Journal of Optics, 14(8):085601, 2012.

[56] Rokas Drevinskas, Jingyu Zhang, Martynas Beresna, Mindaugas Gecevičius, Andrey G Kazanskii, Yuri P Svirko, and Peter G Kazansky. Laser material processing with tightly focused cylindrical vector beams. Applied Physics Letters, 108(22):221107, 2016.

[57] Emil Wolf et al. Introduction to the Theory of Coherence and Polarization of Light. Cambridge University Press, 2007.

[58] Leonard Mandel and Emil Wolf. Optical coherence and quantum optics. Cambridge university press, 1995.

[59] Dalip Singh Mehta, Kanchan Saxena, Satish Kumar Dubey, and Chandra Shakher. Coherence characteristics of light-emitting diodes. Journal of Luminescence, 130(1):96–102, 2010.

[60] Rajiv Dubey and Raj Kumar. A simple setup for measurement of the coherence length of a laser diode using holographic optics. European Journal of Physics, 40(5):055304, 2019.

[61] Bahaa EA Saleh and Malvin Carl Teich. Fundamentals of photonics. john Wiley & sons, 2019.

[62] Heylal Mashaal, Alex Goldstein, Daniel Feuermann, and Jeffrey M Gordon. First direct measurement of the spatial coherence of sunlight. Optics Letters, 37(17):3516–3518, 2012.

[63] François Courvoisier, Jie Zhang, MK Bhuyan, Maxime Jacquot, and John Michael Dudley. Applications of femtosecond bessel beams to laser ablation. Applied Physics A, 112(1):29–34, 2013.

[64] Georgios A Siviloglou and Demetrios N Christodoulides. Accelerating finite energy Airy beams. Optics Letters, 32(8):979, apr 2007.

[65] John Broky, Georgios A Siviloglou, Aristide Dogariu, and Demetrios N Christodoulides. Self-healing properties of optical Airy beams. Phys. Rev. Lett. Contemp. Phys, 58(46):1499–1501, aug 1987.

[66] A. Couairon and A. Mysyrowicz. Femtosecond filamentation in transparent media. Physics Reports, 441(2-4):47–189, mar 2007.

[67] F. Gori, G. Guattari, and C. Padovani. Bessel-Gauss beams. Opt. Commun., 64(6):491–495, dec 1987.

[68] Darioush Abdollahpour, Paris Panagiotopoulos, Margherita Turconi, Ottavia Jedrkiewicz, Daniele Faccio, Paolo Di Trapani, Arnaud Couairon, Dimitris Papazoglou, and Stelios Tzortzakis. Long spatiotemporally stationary filaments in air using short pulse UV laser Bessel beams. Opt. Express, 17(7):5052, mar 2009.

[69] Zhengyi Yang, Martynas Prokopas, Jonathan Nylk, Clara Coll-Lladó, Frank J. Gunn-Moore, David E. K. Ferrier, Tom Vettenburg, and Kishan Dholakia. A compact Airy beam light sheet microscope with a tilted cylindrical lens. Biomed. Opt. Express, 5(10):3434, oct 2014.

[70] Peng Zhang, Jai Prakash, Ze Zhang, Matthew S Mills, Nikolaos K Efremidis, Demetrios N Christodoulides, and Zhigang Chen. Trapping and guiding microparticles with morphing autofocusing Airy beams. Optics Letters, 36(15):2883, aug 2011.

[71] Dimitris G. Papazoglou, Vladimir Yu. Fedorov, and Stelios Tzortzakis. Janus waves. Optics Letters, 41(20):4656, oct 2016.

[72] Miguel A Bandres. Accelerating beams. Optics Letters, 34(24):3791–3793, 2009.

[73] Pavel Polynkin, Miroslav Kolesik, Jerome V. Moloney, Georgios A. Siviloglou, and Demetrios N. Christodoulides. Curved plasma channel

generation using ultraintense airy beams. Science, 324(5924):229–232, apr 2009.

[74] Jörg Baumgartl, Michael Mazilu, and Kishan Dholakia. Optically mediated particle clearing using airy wavepackets. Nature photonics, 2(11):675–678, 2008.

[75] Jonathan Nylk, Kaley McCluskey, Sanya Aggarwal, Javier A Tello, and Kishan Dholakia. Enhancement of image quality and imaging depth with airy light-sheet microscopy in cleared and non-cleared neural tissue. Biomedical optics express, 7(10):4021–4033, 2016.

[76] Daryoush Abdollahpour, Sergiy Suntsov, Dimitrios G. Papazoglou, and Stelios Tzortzakis. Spatiotemporal Airy light bullets in the linear and nonlinear regimes. Physical Review Letters, 105(25):253901, dec 2010.

[77] David K Lynch, William Charles Livingston, and William Livingston. Color and light in nature. Cambridge University Press, 2001.

[78] Elad Greenfield, Mordechai Segev, Wiktor Walasik, and Oren Raz. Accelerating Light Beams along Arbitrary Convex Trajectories. Phys. Rev. Lett., 106(21):213902, may 2011.

[79] Don M Cottrell, Jeffrey A Davis, and Thomas M Hazard. Direct generation of accelerating Airy beams using a 3/2 phase-only pattern. Optics Letters, 34(17):2634–2636, 2009.

[80] Pablo Vaveliuk, Alberto Lencina, Jose A Rodrigo, and Oscar Martinez Matos. Symmetric airy beams. Optics letters, 39(8):2370–2373, 2014.

[81] Pablo Vaveliuk, Alberto Lencina, Jose A Rodrigo, and Ó Martnez-Matos. Intensity-symmetric airy beams. JOSA A, 32(3):443–446, 2015.

[82] Dimitris Mansour. Design Techniques for the Generation of Novel Optical Wavepackets. Master's thesis, University of Crete, Heraklion, Crete, Greece, 2016.

[83] Wanli Lu, Xu Sun, Huajin Chen, Shiyang Liu, and Zhifang Lin. Abruptly autofocusing property and optical manipulation of circular airy beams. Physical Review A, 99(1):013817, 2019.

[84] Chi-Young Hwang, Kyoung-Youm Kim, and Byoungho Lee. Bessel-like beam generation by superposing multiple Airy beams. Optics Express, 19(8):7356, apr 2011.

[85] Ioannis Chremmos, Peng Zhang, Jai Prakash, Nikolaos K Efremidis, Demetrios N Christodoulides, and Zhigang Chen. Fourier-space generation of abruptly autofocusing beams and optical bottle beams. Optics Letters, 36(18):3675, sep 2011.

[86] Ioannis Chremmos, Nikolaos K Efremidis, and Demetrios N Christodoulides. Pre-engineered abruptly autofocusing beams. Optics Letters, 36(10):1890, may 2011.

[87] Hongchang Deng, Yonggui Yuan, and Libo Yuan. Annular arrayed-waveguide fiber for autofocusing Airy-like beams. Optics Letters, 41(4):824, feb 2016.

[88] Yunfeng Jiang, Kaikai Huang, and Xuanhui Lu. Propagation dynamics of abruptly autofocusing Airy beams with optical vortices. Optics express, 20(17):18579–84, aug 2012.

[89] Hwang Chi-Young, Kim Kyoung-Youm, and Lee Byoungho. Dynamic Control of Circular Airy Beams With Linear Optical Potentials. Photonics Journal, IEEE, 4(1):174–180, 2012.

[90] Jinggui Zhang, Yongfan Li, Zuwei Tian, and Dajun Lei. Controllable autofocusing properties of conical circular Airy beams. Optics Communications, 391(January):116–120, 2017.

[91] Maria Manousidaki, Vladimir Yu Fedorov, Dimitrios G Papazoglou, Maria Farsari, and Stelios Tzortzakis. Ring-airy beams at the wavelength limit. Optics letters, 43(5):1063–1066, 2018.

[92] Georgios A Siviloglou, John Broky, Aristide Dogariu, and Demetrios N Christodoulides. Ballistic dynamics of Airy beams. Optics Letters, 33(3):207, feb 2008.

[93] Yiqi Zhang, Milivoj R. Belić, Huaibin Zheng, Haixia Chen, Changbiao Li, Yuanyuan Li, and Yanpeng Zhang. Interactions of Airy beams, nonlinear accelerating beams, and induced solitons in Kerr and saturable nonlinear media. Optics Express, 22(6):7160, mar 2014.

[94] Maria Manousidaki, Dimitrios G. Papazoglou, Maria Farsari, and Stelios Tzortzakis. 3D holographic light shaping for advanced multiphoton polymerization. Opt. Lett., 45(1):85, jan 2020.

[95] Jennifer E Curtis and David G Grier. Structure of optical vortices. Physical review letters, 90(13):133901, 2003.

[96] Jian Wang. Advances in communications using optical vortices. Photonics Research, 4(5):B14–B28, 2016.

[97] Ruslan Vasilyeu, Angela Dudley, Nikolai Khilo, and Andrew Forbes. Generating superpositions of higher–order bessel beams. Optics express, 17(26):23389–23395, 2009.

[98] Ronald Rop, Angela Dudley, Carlos López-Mariscal, and Andrew Forbes. Measuring the rotation rates of superpositions of higher-order bessel beams. Journal of Modern Optics, 59(3):259–267, 2012.

[99] Christian Schulze, Filippus S Roux, Angela Dudley, Ronald Rop, Michael Duparré, and Andrew Forbes. Accelerated rotation with orbital angular momentum modes. Physical Review A, 91(4):043821, 2015.

[100] Jason Webster, Carmelo Rosales-Guzmán, and Andrew Forbes. Radially dependent angular acceleration of twisted light. Optics letters, 42(4):675–678, 2017.

[101] Apostolos Brimis, Konstantinos G Makris, and Dimitris G Papazoglou. Tornado waves. Optics Letters, 45(2):280–283, 2020.

[102] Joseph W Goodman. Introduction to Fourier optics. Roberts and Company Publishers, 2005.

[103] P-Y Madec. Overview of deformable mirror technologies for adaptive optics and astronomy. In Adaptive Optics Systems III, volume 8447, page 844705. International Society for Optics and Photonics, 2012.

[104] Jacques M Beckers. Adaptive optics for astronomy: principles, performance, and applications. Annual review of astronomy and astrophysics, 31(1):13–62, 1993.

[105] Robert K Tyson. Principles of adaptive optics. CRC press, 2015.

[106] Ignacio Moreno, Jeffrey A Davis, Travis M Hernandez, Don M Cottrell, and David Sand. Complete polarization control of light from a liquid crystal spatial light modulator. Optics Express, 20(1):364–376, 2012.

[107] H Kück, W Doleschal, A Gehner, W Grundke, R Melcher, J Paufler, R Seltmann, and G Zimmer. Deformable micromirror devices as phase-modulating high-resolution light valves. Sensors and Actuators A: Physical, 54(1-3):536–541, 1996.

[108] Brian Vohnsen, Alessandra Carmichael Martins, Salihah Qaysi, and Najnin Sharmin. Hartmann–shack wavefront sensing without a lenslet array using a digital micromirror device. Applied optics, 57(22):E199–E204, 2018.

[109] Dimitrios G. Papazoglou. Lecture notes on Foundations of Modern Optics, 2013.

[110] D. C. O'Shea. Elements of Modern Optical Design. John Wiley and Sons, 2nd edition, 1985.

[111] J. C. Wyant and K Creath. Basic Wavefront Aberration Theory for Optical Metrology. In R.˜R. Shannon and J.˜C. Wyant, editors, Applied Optics and Optical Engineering, Volume XI, volume 11, page 2, 1992.

[112] Chris Velzel. A course in lens design, volume 183. Springer Series in Optical Sciences, 2014.

[113] Zhaolou Cao, Chunjie Zhai, Jinhua Li, Fenglin Xian, and Shixin Pei. Light sheet based on one-dimensional Airy beam generated by single cylindrical lens. Optics Communications, 393(February):11–16, jun 2017.

[114] Dimitris Mansour and Dimitris G Papazoglou. Ultra-broadband tunable continuous phase masks using optical aberrations. Optics letters, 43(21):5480–5483, 2018.

[115] Andreas Valdmann, Peeter Piksarv, Heli Valtna-Lukner, and Peeter Saari. Realization of laterally nondispersing ultrabroadband Airy pulses. Optics Letters, 39(7):1877, apr 2014.

[116] Joseph W. Goodman. Introduction to Fourier Optics. McGraw-Hill, New York, 2nd edition, 1996.

[117] Iam-Choon Khoo. Liquid crystals, volume 64. John Wiley & Sons, 2007.

[118] D Gabor. A new microscopic principle., 1948.

[119] Jeffrey A Davis, Don M Cottrell, Juan Campos, María J Yzuel, and Ignacio Moreno. Encoding amplitude information onto phase-only filters. Applied optics, 38(23):5004–5013, 1999.

[120] Noa Voloch-Bloch, Yossi Lereah, Yigal Lilach, Avraham Gover, and Ady Arie. Generation of electron Airy beams. Nature, 494(7437):331–335, feb 2013.

[121] J E Morris, M Mazilu, J Baumgartl, T Cizmár, and K Dholakia. Propagation characteristics of Airy beams: dependence upon spatial coherence and wavelength. Optics express, 17(15):13236–13245, 2009.

[122] Yaakov Lumer, Yi Liang, Ran Schley, Ido Kaminer, Elad Greenfield, Daohong Song, Xinzheng Zhang, Jingjun Xu, Zhigang Chen, and Mordechai Segev. Incoherent self-accelerating beams. Optica, 2(10):886–892, 2015.

[123] Miguel A Bandres, Ido Kaminer, Matthew Mills, BM Rodríguez-Lara, Elad Greenfield, Morderchai Segev, and Demetrios N Christodoulides. Accelerating optical beams. Optics and Photonics News, 24(6):30–37, 2013.

[124] Kimmo Saastamoinen, Jani Tervo, Jari Turunen, Pasi Vahimaa, and Ari T Friberg. Spatial coherence measurement of polychromatic light with modified young's interferometer. Optics express, 21(4):4061–4071, 2013.

[125] Atri Halder, Henri Partanen, Aleksi Leinonen, Matias Koivurova, Tommi K Hakala, Tero Setälä, Jari Turunen, and Ari T Friberg. Mirror-based scanning wavefront-folding interferometer for coherence measurements. Optics Letters, 45(15):4260–4263, 2020.

[126] Abhinandan Bhattacharjee, Shaurya Aarav, and Anand K Jha. Two-shot measurement of spatial coherence. Applied Physics Letters, 113(5):051102, 2018.

[127] K. Y. Kim, A. J. Taylor, J. H. Glownia, and G. Rodriguez. Coherent control of terahertz supercontinuum generation in ultrafast laser–gas interactions. Nature Photonics, 2(10):605–609, 2008.

[128] Anastasios D Koulouklidis, Claudia Gollner, Valentina Shumakova, Vladimir Yu. Fedorov, Audrius Pugžlys, Andrius Baltuška, and Stelios Tzortzakis. Observation of extremely efficient terahertz generation from mid-infrared two-color laser filaments. Nature Communications, 11:292, 2020.

[129] J Durnin, J J Miceli, and J H Eberly. Diffraction-free beams. Physical Review Letters, 58(15):1499, 1987.

[130] L Froehly, F Courvoisier, A Mathis, M Jacquot, L Furfaro, R Giust, P A Lacourt, and J M Dudley. Arbitrary accelerating micron-scale caustic beams in two and three dimensions. Optics Express, 19(17):16455–16465, 2011.

[131] T. Carmon, R. Uzdin, C. Pigier, Z. H. Musslimani, M. Segev, and A. Nepomnyashchy. Rotating propeller solitons. Physical Review Letters, 87(14):12–15, 2001.

[132] Christian Schulze, Filippus S. Roux, Angela Dudley, Ronald Rop, Michael Duparré, and Andrew Forbes. Accelerated rotation with orbital angular momentum modes. Physical Review A, 91(4):043821, apr 2015.

[133] Jason Webster, Carmelo Rosales-Guzmán, and Andrew Forbes. Radially dependent angular acceleration of twisted light. Optics Letters, 42(4):675–678, 2017.

[134] Serguey Odoulov, Alexandr Shumelyuk, Holger Badorreck, Stefan Nolte, Kay-Michael Voit, and Mirco Imlau. Interference and holography with femtosecond laser pulses of different colours. Nature Communications, 6(1):5866, may 2015.

[135] Olivier Vallée and Manuel Soares. Airy functions and applications to physics. World Scientific Publishing Company, 2010.

Acronyms

AR: Aspect Ratio
a.u.: arbitrary units
BBO: Barium Borate
CAB: Circular Airy Beams
CCD: Charge-Coupled Device
CV: Cylindrical Vector
CW: Continuous Wave
DLW: Direct Laser Writing
DMD: Digital Micro-mirror Device
EMCF: Equal-time Mutual Coherence Function
FT: Fourier Transform
FWHM: Full Width Half Maximum
GUI : Graphical User Interface
JW: Janus Wave
LCOS: Liquid Crystal On Silicon
LED: Light Emitting Diode
NA: Numerical Aperture
OAM: Orbital Angular Momentum
OPD: Optical Path Difference
OPL: Optical Path Length
RMS: Root Mean Square
SLM: Spatial Light Modulator
TDM: Time Division Multiplexing
ToW: Tornado Wave

List of Figures

List of Tables

Appendix A

In this section will show that for a polychromatic 1D Airy beam generated from a reflective system that is achromatic in optical path difference, G, its spectral components co-propagate along z axis. We start from the field, at the initial plane, that describes such a beam in normalized coordinates $\phi(s, \xi = 0) = \mathrm{Ai}(s)\exp(\alpha s)$, where $s = x/w$, $\xi = z/kw^2$, α is the truncation factor, w is the width parameter, $k = 2\pi n/\lambda_0$ is the wavenumber, λ_0 is the wavelength and n the refractive index. This in normalized coordinates is $\phi(x, z = 0) = \mathrm{Ai}(x/w)\exp(\alpha x/w)$. Now we take the Fourier transform of this field and we come up with:

$$\begin{aligned}\Phi(u) = w\exp[(-\alpha w^2\frac{k^2}{f^2}u^2) \\ + \frac{i}{3}(w^3\frac{k^3}{f^3}u^3 - 3\alpha^2 w\frac{k}{f}u - i\alpha^3)]\end{aligned} \tag{4.10}$$

where u is the coordinate in frequency space [102], and f is the focal distance of the lens that performs the optical Fourier transform. Eq.4.10 for $a \to 0$ is simplified to:

$$\Phi(u) = w\exp[(-\alpha w^2\frac{k^2}{f^2}u^2) + \frac{i}{3}(w^3\frac{k^3}{f^3}u^3)] \tag{4.11}$$

Comparing Eq. 4.11 with the field distribution of Gaussian with a cubic phase:

$$G(x) = \exp(-\frac{x^2}{w_0^2})\exp(i\delta x^3) \tag{4.12}$$

where w_0 is the waist radius of the Gaussian and δ is a parameter of the cubic phase, we deduce the following:

$$\begin{aligned} w &= \frac{(3\delta)^{1/3}f}{k} \\ a &= \frac{f^2}{w^2k^2w_0^2} = \frac{1}{w_0^2(3\delta)^{2/3}} \\ \delta &= \frac{w^3k^3}{3f^3}\end{aligned} \tag{4.13}$$

Assuming that we have an 1D Airy beam with an extra linear phase, in normalized units, its initial field is $u(s,\xi=0) = \mathrm{Ai}(s)\exp(\alpha s)\exp(ivs)$, $v = \theta k w$, and θ the angle of the linear phase. While the field distribution along propagation is described by:

$$\begin{aligned} u(s,\xi) =& \mathrm{Ai}[s - (\frac{\xi}{2})^2 - v\xi + i\alpha\xi] \\ & \times \exp(\alpha s - \frac{\alpha\xi^2}{2} - \alpha v\xi) \\ & \times \exp[i(-\frac{\xi^3}{12} + (\alpha^2 - v^2 + s)\frac{\xi}{2} + vs - \frac{v\xi}{2})] \end{aligned} \tag{4.14}$$

We can easily deduce that the maximum of the Airy beam propagates along the z axis, in normalized coordinates, according to:

$$s_m - (\frac{\xi}{2})^2 - v\xi \simeq -1 \tag{4.15}$$

where s_m denotes the transverse displacement of the main lobe. Meanwhile in physical coordinates this relation becomes:

$$x_m \simeq \theta z + \frac{z^2}{4k^2w^3} - w \tag{4.16}$$

In the above equations we assumed that $\alpha \to 0$ thus the term $i\alpha\xi$ of Eq. 4.14 can be neglected, also we took the approximation that the Airy function Ai have maximum at $\simeq -1$. If we now set the beginning of the axis at the maximum Eq. 4.16 becomes $x_m \simeq \theta z + z^2/(4k^2w^3)$ and recalling from the first equation of the set of Eq. 4.13 that $w = ((3\delta)^{1/3}f)/k$ and $\delta = nk_0\delta_0$, where δ_0 is a constant, then we have:

$$x_m \simeq \theta z + z^2/(12f^3\delta_0) \tag{4.17}$$

From Eq. 4.17 it is clear that the trajectory of the main lobe of an 1D Airy beam, when is generated by an achromatic system ($\delta_0 = constant$), is independent form the wavelength, thus all the spectral components propagating in the same curve.

Appendix B

Cubic phase play an essential on the generation of an Airy beam, this can be achieved by imposing such a phase into a Gaussian beam and then take its Fourier transform. Moreover, the Fourier transform of a pure Airy function is a pure cubic distribution * [135]. Here we will show, through matrix theory, that the Fourier transform of a cubic wavefront is a phase distribution in the form $x^{3/2}$, which results in a parabolic caustic. Starting with the vector that describes a ray coming from a cubic wavefront, which is perpendicular to its tangent, is:

$$\begin{pmatrix} y_0 \\ \beta_0 \end{pmatrix} = \begin{pmatrix} y_0 \\ a{y_0}^2 \end{pmatrix} \tag{4.18}$$

where y_0 is the position, and $\beta_0 = a{y_0}^2$ the angle of the ray, while a is a constant. The matrix that describes a lens, with focal length f, preforming a Fourier transform is given by:

$$\begin{pmatrix} 0 & f \\ -\frac{1}{f} & 0 \end{pmatrix} = \begin{pmatrix} 1 & f \\ 0 & 1 \end{pmatrix} \begin{pmatrix} 1 & 0 \\ -\frac{1}{f} & 1 \end{pmatrix} \begin{pmatrix} 1 & f \\ 0 & 1 \end{pmatrix} \tag{4.19}$$

Thus for the vector at the exit of such an optical system we have:

$$\begin{pmatrix} y_1 \\ \beta_1 \end{pmatrix} = \begin{pmatrix} 0 & f \\ -\frac{1}{f} & 0 \end{pmatrix} \begin{pmatrix} y_0 \\ \beta_0 \end{pmatrix} \tag{4.20}$$

where

$$\begin{aligned} y_1 &= af{y_0}^2 \\ b_1 &= -\frac{y_0}{f} = -\frac{{y_1}^{1/2}}{a^{1/2}f^{3/2}} \end{aligned} \tag{4.21}$$

Finally we have:

$$\begin{pmatrix} y_1 \\ \beta_1 \end{pmatrix} = \begin{pmatrix} y_1 \\ -\frac{{y_1}^{1/2}}{a^{1/2}f^{3/2}} \end{pmatrix} \tag{4.22}$$

*$\mathfrak{F}(Ai(x)) = \exp(ik^3/3)$

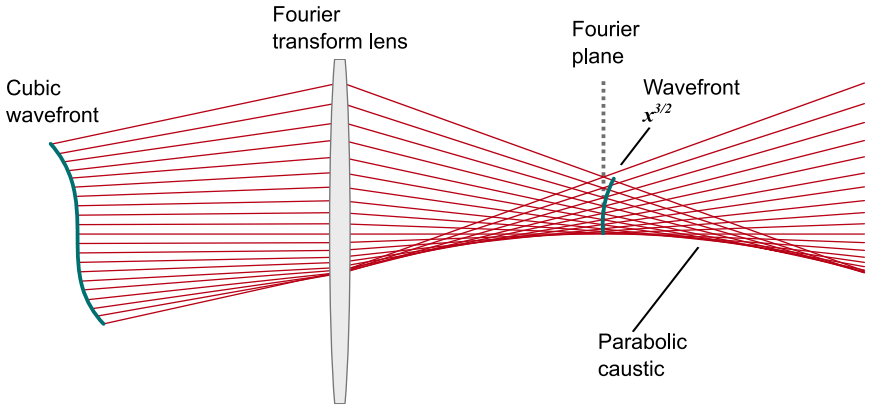

Figure 4.27: Illustration of how an Airy beam can be formed as a result of a caustic of rays. In this case a cubic phase modulated wavefront is Fourier transformed by a lens, resulting to a $x^{3/2}$ phase distribution at the Fourier plane. (Raytracing simulation results)

The rays with such an angle distribution are perpendicular to a wavefront of the form of $\sim y^{3/2} \rightarrow \sim x^{3/2}$. Such rays form a parabolic caustic as shown in Fig. 4.27.